VNIVERSITAT DE VALÈNCIA

Doctorado en Nanociencia y Nanotecnología

Ph.D. Thesis:

Material and interface engineering for vacuum deposited perovskite solar cells

Azin Babaei

February 2020

Directors:

Prof. Hendrik Jan Bolink

Dr. Michele Sessolo

Prof. Hendrik Jan Bolink y **Dr. Michele Sessolo**, Investigadores de la Universidad de Valencia en el Instituto de Ciencia Molecular (ICMol), certifican que la memoria presentada por la estudiante de doctorado Azin Babaei, con el título "Material and interface engineering for vacuum deposited perovskite solar cells" corresponde a su Tesis Doctoral y ha sido realizada bajo su dirección y tutoría, autorizando mediante este escrito la presentación de la misma.

En Valencia, a 07 de Febrero del 2020

Prof. Hendrik Jan Bolink	Dr. Michele Sessolo
(director y tutor)	(director)

"*An experiment is a question which science poses to nature and a measurement is the recording of nature's answer.*"

Max Planck

Chapter 1.

Introduction

1. Introduction

1.1. Perovskite solar cells: A new paradigm in photovoltaics

Renewable energy resources have emerged as an important component of global energy production as a consequence of growing concerns about fossil fuels, mainly the environmental consequences of greenhouse gases leading to global warming. Despite a significant recent increase in renewable energy use and efficiency, most (≈ 80%) of the world energy demand is still met by fossil fuels, as shown in figure 1.[1] All processes associated with fossil fuels extraction, transportation, refinement and particularly their consumption have harmful impact on the environment. One solution to meet the world energy demands while reducing the environmental impact of energy generation is a large deployment of renewable energy sources. The most important features of renewable energy sources are the low environmental impact and their abundancy.

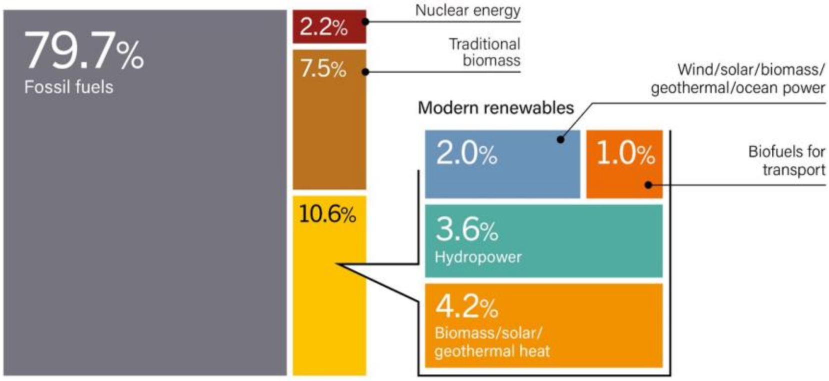

Figure 1. Estimated renewable energy share of global energy consumption in 2017. The image is adapted from reference [1].

Solar irradiation is the most abundant energy source on earth and among the technologies available to harvest it, photovoltaics

(PVs) is one of the most promising. PV system consists of several components, including solar cell panels which can absorb and convert the solar energy into electricity, figure 2. Despite the advantages of PV technology, PV is still considered as an expensive substitute to conventional fossil fuels. In order to make PV more competitive in the current energy market, a substantial cost reduction of module production and solar energy storage is desirable.

Solar cells are generally divided into three main so-called generations. The first generation solar cells employ crystalline Silicon (c-Si) and are considered as the oldest commercially available photovoltaic technology. Silicon is widely abundant on earth; however, challenges still remain regarding processing it into an efficient semiconductor for solar cells. Si solar cells have a relatively high performance, but as high purity Si is required and because of the energy consumption of the purification process, the price is still relatively high compared to the power output. Another widely studied photovoltaic technology includes the second generation solar cells or thin-film solar cells because they are made of very thin layers of semiconductor materials such as cadmium telluride (CdTe), gallium arsenide (GaAs) or copper indium gallium selenide (CIGS). CdTe and CIGS solar cells are potentially cheaper to fabricate, compared to first generation devices, but they have lower efficiency. The opposite is true for GaAs solar cells.[2] The third generation of solar cells is made from organic material, quantum dots and hybrid semiconductors which offer, in principle, lower manufacturing costs and simple fabrication. Recent breakthroughs in this field include the production of solar cells composed of a class of materials called perovskites, which promise to deliver cheaper and efficient solar panels.[3]

Figure 2. The images of roof integrated PV system and solar panels on an electric car. The images are adapted from references [4,5].

1.2. Hybrid perovskites: Structure, properties, and challenges

The term “perovskite” originated from the crystal structure of calcium titanate, which was discovered in 1839 by the German mineralogist Gustav Rose and named in honour of the Russian mineralogist Lev Perovski.[6] Metal halide perovskites can be categorized into two groups, alkali halide and organic (or hybrid) halide perovskites, both of which behave as semiconductors.[7] Three dimensional hybrid perovskites share the general formula ABX_3, where A is a monovalent cation, B is a divalent metal and X is a halide anion. This crystal structure (figure 3) consists of a framework of corner-sharing metal halide (BX_6) octahedra that extend in three dimensions, with interstitial A cations. In the organic-inorganic perovskites, A is an organic (methylammonium, $CH_3NH_3^+$ or MA^+, or formamidinium $NH_2CH{=}NH_2^+$ or FA^+) or inorganic monovalent cation (Cs^+), B is a divalent metal (Pb^{2+} or Sn^{2+}) and X is a halide (Cl^-, Br^-, I^-).[8]

Knowledge of the optical and electrical properties of perovskites such as bandgap energy, charge carrier mobility, diffusion length and lifetime is essential for the fabrication of optoelectronic devices. Herein, we summarize some of the optoelectronic properties of metal halide perovskites.

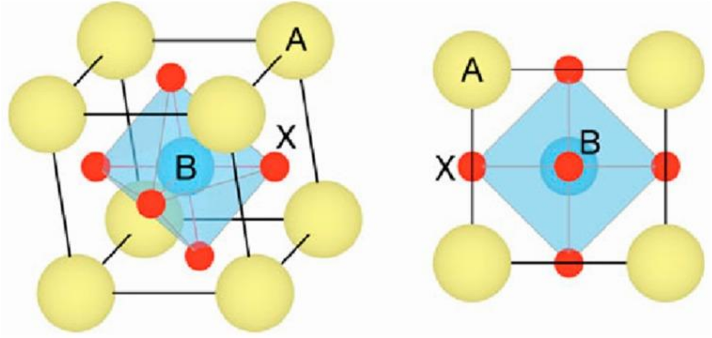

Figure 3. Two views of the cubic perovskite crystal structure. Atoms of type A (in yellow) are positioned at the cube corners, B atoms (in blue) at the cube center, and X atoms (in red) at cube faces. The image is adapted from reference [9].

High optical absorption coefficient: hybrid perovskites, in particular methylammonium lead iodide ($MAPbI_3$), have a high optical absorption coefficient ($\alpha > 10^{15}$ cm^{-1}) comparable to that of inorganic semiconductors such as GaAs.[10] In comparison with Si solar cells, which typically need an absorber layer with thickness of hundreds of microns, perovskite solar cells can be fabricated with submicron thick absorber layers. This originates from the generic nature of direct band gap materials.[11] Furthermore, the exciton binding energy in hybrid perovskites is low, in the order of tens of meV, favouring free charge carrier generation at room temperature.[11,12]

Balanced electron/hole mobility and long diffusion length: the charge carrier mobility, μ, describes the ability of electrons and holes to move within a semiconductor under an applied bias, and is defined as the ratio of the carrier drift velocity υ and the applied field E:

$$\mu = \frac{\upsilon}{E} \tag{1}$$

The mobility is connected to the charge diffusion coefficient D through the Einstein relation:

$$D = \mu \frac{kT}{e} \tag{2}$$

Where k is the Boltzmann constant, T the temperature and e the electron charge. A carrier with a specific lifetime τ will travel at an average distance L (known as diffusion length) from the generation point following the relation:

$$L = \sqrt{D\,\tau} \tag{3}$$

Charge carrier mobility of 8 $cm^2\ V^{-1}\ s^{-2}$ and 11.6 $cm^2\ V^{-1}\ s^{-2}$ have been reported for $MAPbI_3$ and $MAPbI_{3-x}Cl_x$ halide perovskite thin films, respectively.[13,14] Furthermore, polycrystalline perovskite films exhibit a large diffusion length of carriers (in the range of µm) which together with the balanced electron/hole mobility, facilitates charge extraction from the perovskite absorber layer toward the electrodes.[15–19]

Bandgap energy tunability: The generic perovskite structure ABX_3 allows synthesizing a wide range of different materials with altered properties by simple substitution of the building blocks A, B, and X. This is due to the fact that the conduction band of the perovskite is formed mainly by the *p* orbitals of the B atoms while the valence band is composed mainly by the *p* orbitals of the halide.[20] On the other hand, the A cation only influences the electronic structure via changing the geometry of the ABX_3

lattice. $MAPbI_3$, for instance, has a band gap energy of approximately 1.5-1.6 eV.[21] The band gap can be tuned by replacement of the MA^+ for FA^+ which results in a narrower bandgap (1.47 eV for the pure $FAPbI_3$), whereas the substitution of I^- by Br^- or Cl^-, with smaller ionic radii, increases the bandgap to 2.3 eV and 3.1 eV for $MAPbBr_3$ and $MAPbCl_3$, respectively.[22–25]

Although perovskite solar cells have already achieved performance comparable to Si-based PV, still a considerable amount of challenges and questions remain unanswered. One barrier for the further development of perovskite solar cells is the current hysteresis, which is observed when applying different voltage sweeping rates and directions. The mechanism behind the hysteresis is still unknown but several hypotheses have been established.[26–28] Recent findings support that both ion migration and charge trapping are involved in the current hysteresis.[29] Another issue regarding perovskite solar cells is toxicity that comes from the use of lead as B site cation. Large scale fabrication wastes might be an issue of concern for the environment. However, studies already showed that the possible contamination of perovskite would be negligible compared with other sources of lead pollutions.[30] Moreover, attempts to develop lead-free perovskite solar cells are on their way.[31–35]

The stability of perovskite films and solar cells is a central topic in the development of this type of materials and devices. The crystal structure stability, thermal stability and device stability are among the most important challenges that need to be addressed. The Goldschmidt tolerance factor t [36] has been extensively used to predict the stability of the perovskite structure based only on geometrical consideration of the ABX_3 unit cell, taking into account the ionic radii r_i of each ion (A, B, X):

$$t = \frac{r_A + r_X}{\sqrt{2}(r_B + r_X)} \qquad (4)$$

Where r_A, r_B and r_X are the ionic radii for the organic cation A, the metal B and the halide anion X, respectively. The ideal cubic perovskite structure would have a t = 1, and in general stable cubic structures are expected when $0.89 < t < 1$ and.[10] Lower tolerance factors imply a lower symmetry, hence the perovskite structure would shift to orthorhombic or tetragonal, influencing the optoelectronic properties of the semiconductor.[37] The most studied perovskite is $MAPbI_3$, which has a tolerance factor slightly higher than 0.9.[38]

The ionic radius is not the only factor determining the perovskite crystal structure. The crystal structure is also influenced by the temperature. For example, $MAPbI_3$ has three crystal structures depending on the temperature [39], with the tetragonal crystal structure as the most stable at room temperature.[40–44] $MAPbI_3$ undergoes a reversible tetragonal (β) to cubic (α) phase transition which occurs at 56 °C, while stabilized orthorhombic (γ) phase occurs at temperature around 160 K.[43] Recent studies showed that the cubic phase of thermally evaporated $MAPbI_3$ thin films can be obtained and stabilized even at room temperature by simply tuning the material stoichiometry.[45] The thermal stability of $MAPbI_3$ perovskite and its effect on optoelectronic devices is highly dependent on phase transitions and hence on temperature.[37]

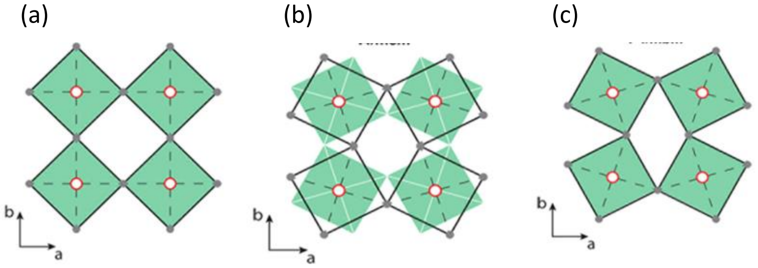

Figure 4. (**a**) Cubic, (**b**) tetragonal and (**c**) orthorhombic perovskite phases obtained from structural optimization of $MAPbI_3$. The images are adapted from reference [41].

Figure 4 displays the common crystal structures for $MAPbI_3$ and for most studied three dimensional hybrid perovskites. The tetragonal-cubic phase transition at 55-60 °C partially influences the thermal stability of perovskite solar cells, as the working temperature of solar panels can be as high as 80 °C.

1.3. Solar cell structure

The first reported perovskite solar cell was designed after the structure of dye-synthesized solar cells (DSSCs), where perovskite materials investigated as a "new" dye in liquid electrolyte in combination with dye-sensitized mesoporous TiO_2 electron transport layers (ETLs).[46] It was observed that the perovskite is a better light absorber compared to the molecular dye, even though the liquid electrolyte could damage the perovskite resulting in device degradation.[47] This triggered researchers to combine features from thin-film PVs and DSSCs, in particular the substitution of the liquid electrolyte with organic hole transport layers (HTLs), resulting in improved device performance and efficiency.[48] Later it was shown that perovskite solar cells can also be fabricated in a planar configuration where the active layer is sandwiched in between two selective charge transport layers.[48,49] Charge transport layers are semiconducting materials with energy levels chosen so that they can selectively transport photogenerated electrons or holes from the perovskite film to the external electrodes. Figure 5 shows the architecture of traditional mesoporous solar cells as well as of planar devices, both in p-i-n and n-i-p configurations. This nomenclature refers to the order of the layers with respect to the transparent electrode and not to the applied potential across the device. If hole are extracted at the front transparent contact the solar cell is named as p-i-n, and vice versa for n-i-p devices. P-i-n perovskite solar cells have attracted a lot of attentions due to their low processing temperature and metal oxide-free structure. These features allow the device fabrication on flexible substrates.[50,51] In addition, p-i-n perovskite solar cells typically show less current-voltage hysteresis.[52,53]

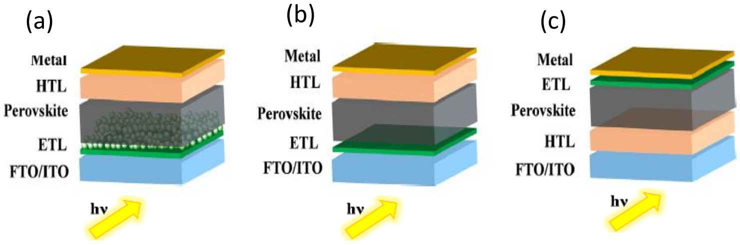

Figure 5. Schematic illustration of the (a) mesoporous n-i-p, (b) planar n-i-p (c) and planar p-i-n device architectures of perovskite solar cells. The images are adapted from reference [54].

Besides planar and mesoporous structures, HTL/ETL free perovskite solar cells and tandem cell configurations have also been reported. In a tandem solar cell, losses due to carrier thermalization are reduced through the use of different and complementary light-absorbing layers.[55]

In this thesis the architecture chosen as a platform to study perovskite solar cells is the planar p-i-n configuration, using small molecular weight organic semiconductors as hole and electron transport layers.

1.4. Solar cell physics

The basic operation of a solar cell involves the following processes.
Absorption of photons and carrier generation: when incident light is absorbed in the semiconductor, free electrons and holes are generated. In principle, all photons with energy larger than the bandgap will lead to the generation of charge carriers. Photons with energy larger than the absorber's bandgap generate so-called hot carriers. The extra energy is rapidly exchanged with the lattice and electrons/holes redistribute towards the lowest energy state available, in a process called thermalization (figure 6). The photogenerated free carriers will lead to a photocurrent when they are collected at the electrodes and connected to a load.

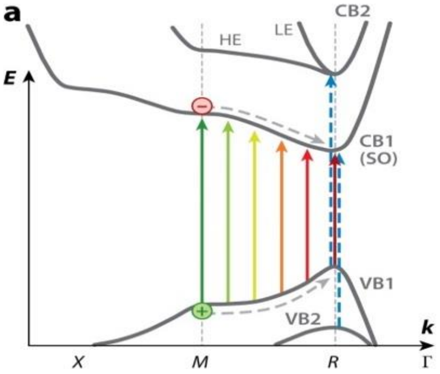

Figure 6. Charge carriers are generated when photons with energies higher than that of bandgap are absorbed. The image is adapted from reference [56].

Recombination: photogenerated carriers can recombine through a process opposite to generation. Understanding and controlling recombination processes is of a great importance as they reduce the charge carrier concentration and hence the power conversion efficiency (PCE). In general, there are three types of recombination, band to band recombination, trap assisted recombination and Auger recombination, as shown in figure 7.

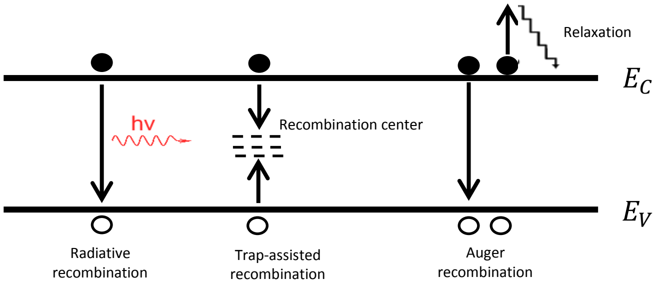

Figure 7. Sources of recombination losses in a perovskite solar cell: (a) radiative recombination, (b) trap-assisted recombination. (c) non-radiative Auger recombination.

When an electron recombines directly from a conduction band state to valence band state, a photon will be generated as a consequence of the relaxation of the electron energy. This process is called radiative recombination. The recombination rate can be expressed with the following equation:

$$R = c_B\,(np - n_i^2) \qquad (5)$$

Where, c_B is the recombination coefficient, n, p and n_i are the electron, hole and intrinsic carrier concentration, respectively. Band to band recombination rate is low under normal solar cell operation.[13]

In trap-assisted recombination, also known as Shockley-Read-Hall (SRH) recombination, electrons/holes are captured by a trap state and they annihilate. It can happen either in the bulk of a semiconductor or on the interface, and the recombination rate is given by:

$$R = \frac{np - n_i^2}{\tau_p(n+n_1)+\tau_n(p+p_1)} \qquad (6)$$

Here, τ_p and τ_n are the minority carrier lifetime of holes and electrons, respectively, which are controlled by the defect density. n_1 and n_2 are constant that depends on the energy levels of the traps. In thin-film photovoltaic devices non-radiative recombination is the most dominant loss process. Non-radiative electron-hole recombination occurs mainly at the interface due to the presence of defect states.[57] It has been already shown that for crystalline Si solar cells, recombination in the bulk can be assumed negligible compared to recombination at the interface.[58]

Interface recombination current, or loss current, can be expressed as follow:

$$J_S = qSne^{\Delta E_F / K_B T} \qquad (7)$$

Where q is the electron charge, S the surface recombination velocity, n the electron density in thermal equilibrium, ΔE_F the quasi-Fermi level splitting, and K_BT the thermal energy. n is mainly related to the built-in potential which means the potential drop at the electrodes determines n, whereas S is mainly determined by the density of defects presents at the surface. Based on the equation (7), to minimize the interfacial recombination current, it is crucial to design defect free interfaces with band alignment that retains the maximum built-in potential. Surface passivation of the perovskite layer can be a key solution which will be discussed in chapter 3.

A large amount of studies has been carried out to better understand the bulk and interfacial recombination in perovskite solar cells. Sarritzu et al. measured the electron-hole free energy as a function of the intensity of the exciting light and compared the values for perovskite films and perovskite/ETL and perovskite/HTL heterojunctions. They measured a lower free energy of electron-hole for the heterojunctions compared to the single perovskite layer, which is due to interfacial non-radiative recombination channels which consequently results in voltage drop and lower device performance.[59] Another study using time-resolved photoluminescence measurements and numerical simulations showed the relation between the accumulation of charge carriers at the perovskite/ETL interface and its effect on interface charge recombination. They showed that charge transport and charge transfer processes are dominant at short delay times after the pulse laser excitations. At longer delay times, charge carrier accumulations at the interface of the perovskite/ETL may occur. These accumulated charge carriers subsequently either recombine at the interface or are reinjected into the perovskite layer.[60] Nonetheless, more studies need to be carried out to obtain a more comprehensive model to describe and clarify the origin of bulk and interface defect states.

Auger recombination is the third type of recombination. In this process, the energy released by a band-to-band transition is transferred to another excited free electron in the conduction band. This high energy electron loses its energy due to collision with the lattice and finally relaxes to the conduction band, as is shown in figure 7.c.

Charge transport and collection: there are two transport mechanisms involved in charge collection, namely diffusion and drift. When a carrier concentration gradient exists in the perovskite semiconductor, carriers will constantly move from areas of high carrier concentration to areas with low concentration in the process of diffusion. Drift-based transport is a consequence of the electric field in the device. A high carrier transfer rate is required to avoid carrier accumulation and loss in the bulk absorber.

1.5. Solar cell characterization

One of the most basic characterizations of semiconductor devices and in particular solar cells involves the measurement of current vs. voltage (IV) characteristics. A solar cell measured in dark conditions shows diode behaviour in the JV curves. An Ideal diode allows the current flow only in forward bias and blocks all current flowing in reverse voltage.

Under illumination, the current shifts to negative values due to the carrier generation inside the cell, namely photocurrent generation. The current in a solar cell is described by the classic Shockley diode equation:

$$I = I_{ph} - I_0 \left\{ e^{\frac{qV}{nkT} - 1} \right\} \tag{8}$$

Where I_{ph} is the photocurrent, V is the applied voltage, I_0 is the reverse saturation current density, q is the elementary charge and n is the ideal factor, k is the Boltzman constant and T the absolute temperature. There are four important parameters which can be extracted from an IV curve obtained from an illuminated solar cell. The first one is the short-circuit current, I_{sc}, which is the current when the voltage across the device is 0. The second one is the open-circuit voltage (V_{OC}), which is the voltage when the current is zero, and is the maximum achievable voltage of a solar cell. By setting the current equal to zero in equation (8), the equation for V_{OC} can be expressed as:

$$V_{oc} = \frac{nkT}{q} \ln\left(\frac{I_{ph}}{I_0} + 1\right) \tag{9}$$

The equation above shows that V_{OC} depends on the saturation current of the solar cell and the photo-generated current. The key effect on V_{OC} is the saturation current, since this may vary by orders of magnitude. The saturation current depends on the charge recombination in the solar cell, thus V_{OC} is a measure of charge recombination in the device: the stronger the charge recombination, the lower the voltage.

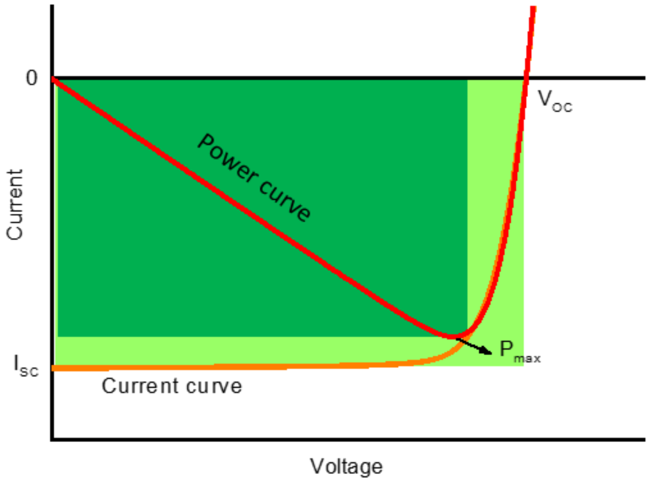

Figure 8. Typical IV-curve, current vs. voltage characteristics of an illuminated solar cell showing the open circuit voltage (V_{OC}) and short circuit current (I_{SC}) as well as the voltage and current at the maximum power point (V_{mp}, I_{mp}). The fill factor is defined as $= \frac{V_{mp}\times I_{mp}}{V_{oc}\times I_{sc}} = \frac{Area\ A}{Area\ B}$.

The output of a solar cell is calculated as $P = I \times V$, which is voltage dependent. The third parameter is the fill factor (FF) that graphically explains how square the IV curve is. The FF is defined as

$$FF = \frac{P_{max}}{V_{oc}\times I_{sc}} = \frac{\max\ (I\times V)}{V_{oc}\times I_{sc}} \tag{10}$$

The FF is equal to the area ratio of A and B in figure 8. The FF is strongly linked to charge transport as well as to series and shunt resistances.

From the three parameters extracted from the IV measurements, one can calculate the efficiency of the solar cell which is the fraction of incident power (solar irradiation) that is converted into electrical power:

$$PCE = \frac{P_{max}}{P_{irradiation}} = \frac{\max(V \times I)}{P_{irradiation}} = \frac{V_{OC} \times I_{SC} \times FF}{P_{irradiation}} \qquad (11)$$

In addition to the IV curve under illumination, the dark IV curve also contains information to further analyse the solar cell. If we consider a diode model of the solar cell in a circuit with series and shunt resistances (figure 9), the current flowing through the device in dark conditions is:

$$I = \ I_0 \ e^{\frac{V-IR_S}{nKT/q}} + \frac{V-IR_S}{R_{SH}} \qquad (12)$$

Where R_s and R_s are the series and shunt resistance respectively. A typical dark IV curve is depicted in figure (10). It can be seen there are three main different regimes of the curve depending on the voltage applied.

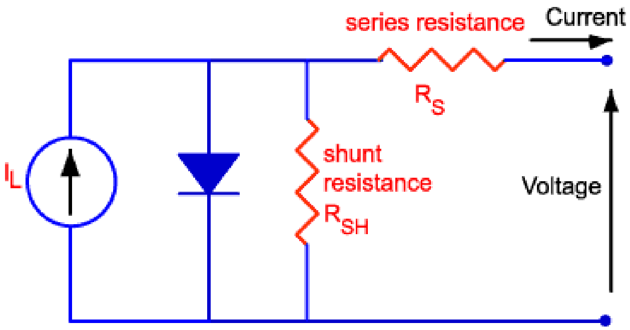

Figure 9. Schematic of a circuit model of a solar cell under illumination with series and shunt resistance.

When the applied bias is low (region A in figure 10), the dark current is dominated by the shunt current which is the second term in the right-hand side of equation (9). Generally, the shunt resistance results from the defects in the perovskite layer or unwanted shunt path in the solar cell. When the applied bias is higher (region B in figure 10), there will be an exponential increase of the current (linear regime in the log scale as in figure 10), described by the exponential term in equation (9). When the current increase deviates from linearity in the log plot, the applied voltage corresponds to the diode built-in potential (V_{bi}), which equals the difference in the work functions of the electrodes. At higher bias (region C in figure 10), the current growth will start to saturate and be limited by the series resistance. Since the low bias region and high bias region are dominated by shunt and series resistance respectively, we can extract the information about them from those two regions.

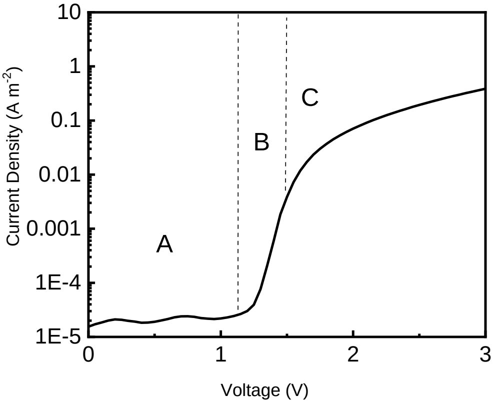

Figure 10. Dark JV curve measurement for a perovskite solar cell. Three different regimes indicated by A, B and C are the consequence of different carrier transport mechanisms.

1.6. The importance of the charge transport layers

In order to fabricate efficient perovskite solar cells, not only the quality of the perovskite film but also the properties of the charge transport layers play an important role. The characteristics of the ETL and the HTL, such as charge carriers mobility, energy levels alignment, morphology and trap states, also influence the performance of the solar cell.

In chapter 1.2, the carrier mobility of the perovskite films and its importance for the solar cell performance was discussed. Similarly, high electron/hole mobility in the charge selective layers (ETL and HTL) is also desired, as photogenerated charge carriers need to be efficiently transported towards the electrodes.

Selectivity of the charge transport layers mainly originates from the energy level alignment at the perovskite/transport layer interface. Figure 11 shows a schematic representation of the energy levels of a perovskite film and the charge transport layers in a solar cell with a planar structure (regardless of p-i-n or n-i-p structure). Free electrons can be selectively extracted from the perovskite conduction band to the lowest unoccupied molecular level (LUMO) of the ETL, if no large energy barrier exists at the perovskite/ETL interface. Simultaneously, holes transfer at this interface should be inhibited by increasing the energy difference between the perovskite valence band and the highest occupied molecular level (HOMO) of the ETL. Similar but energetically opposite characteristics should be fulfilled in order to ensure selective charge extraction at the perovskite/HTL interface.

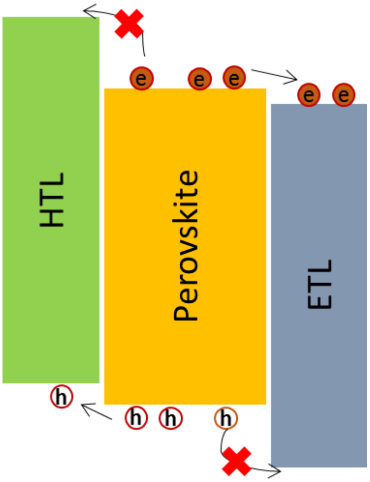

Figure 11. Charge selectivity at the interface of a perovskite film and the transport layers. Electrons are blocked at the perovskite/HTL interface due to the energy barrier between the conduction band of the perovskite and the LUMO of the HTL, and holes are blocked at the perovskite/ETL interface due to the energy barrier between the valence band of the perovskite and the HOMO of the ETL.

Organic electron transport materials (ETMs) are widely used selective electron transport materials in p-i-n perovskite solar cells. Organic molecules have tuneable energy structures to suit the energetics and chemistry of the perovskite layer. Fullerene and its derivatives, such as $PC_{61}BM$, ICBA and $PC_{71}BM$, are good candidates as selective electron extraction materials due to their suitable energy level alignment, good electron mobility and easy deposition process.[61–64] Unsubstituted fullerenes such as C_{60} and C_{70} have higher electron mobility and can be deposited by vacuum sublimation. The energy level and the chemical structure of common ETLs used in p-i-n perovskite solar cells are shown in figure 12.

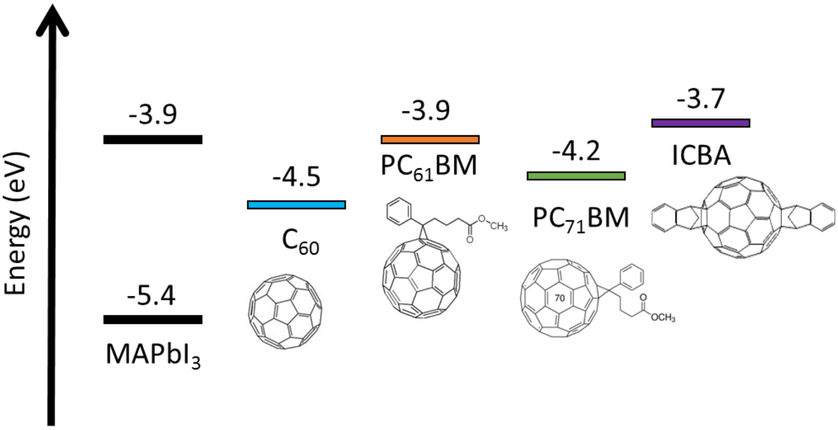

Figure 12. Chemical structure and energy level diagram showing LUMO levels of various ETLs in comparison with the conduction and valence bands of the $MAPbI_3$ perovskite**.**

In p-i-n devices, the HTL acts not only as a selective layer, but also as a window where light enters the device. Therefore, its optical properties are also critical to maximize carrier generation in the perovskite solar cell. This means that to prevent photon loss, the HTL bandgap, its refractive index and the extinction coefficient should be taken into consideration.[65] To date a large number of organic molecules, inorganic materials, and conducting polymers have been tested in perovskite solar cells as HTLs.[23,66,67] The most common HTMs that have been used in p-i-n perovskite solar cells include PEDOT: PSS, spiro-OMeTAD, graphene oxide, NiO and CuSCN.[63,68–71]

In addition, the solar cell performance is influenced by the interface between the charge transport layers and the electrodes. In general, one must ensure ohmic charge extraction by minimizing the energy difference between the electrode work function and the frontier orbitals of the transport material.

Hence, an additional interlayer is usually placed in between the electrode and the transport layer.[72] In p-i-n structure, common materials such as high work function molecules,[73] doped organic semiconductors,[72,74] or metal oxides (MoO_3, V_2O_5 and WO_3)[75] have been proposed as interlayers in between the HTL and the transparent electrode. Likewise, a wide variety of interlayers, such as inorganic metal oxides, organic and polymer materials, metals and metal salts have been tested in between ETLs and the metal electrode. Some of the most important interlayers are depicted in figure 13 and are commented upon below.

Organic materials. Bathocuproine (BCP) is one of the most widely used cathode interface layers in organic light emitting diodes (OLEDs) and organic photovoltaics (OPVs).[76–78] It can be easily thermally sublimed and ensure ohmic electron transfer from metals (Ag, Al) and common ETLs such as fullerenes. Some other organic interfacial materials used to improve the contact between fullerenes and metal electrodes are polyethylenimine ethoxylated (PEIE), poly[3-(6-trimethylammoniumhexyl)thiophene] (P3TMAHT) and poly [(9,9-bis(3'-(N,N-dimethylamino)propyl)-2,7-fluorene)-alt-2,7-(9,9–dioctylfluorene)] (PFN). These materials have been reported to improve charge extraction and supress charge recombination at the interface, which subsequently results in better performances of the solar cell.[79–83]

Inorganic metal oxides. It has been reported that a thin layer of an n-type metal oxide such as TiO_2 , ZnO or SnO_2 on top of fullerene ETLs in p-i-n solar cells can enhance the electrical contact and also increase the stability of the device.[84,85]

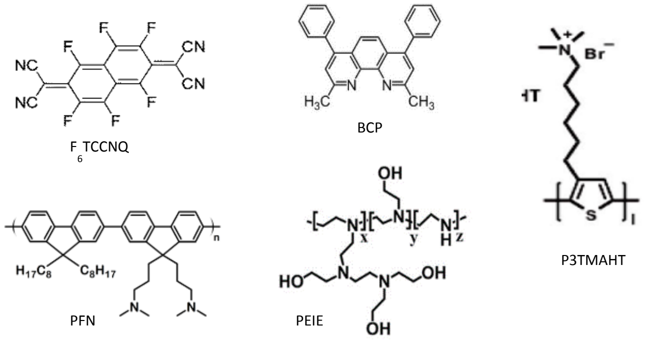

Figure 13. Chemical structure of various organic interfacial materials.

Metals and metal salts. Alkali metal halides are widely used as ETL or cathode buffer layers in OLEDs to enhance electron injection.[86] The widely adopted LiF used as a buffer layer in perovskite solar cells improves the J_{SC} and FF of the device and supresses leakage current under reversed bias.[81]

Aim of the thesis

The aim of this thesis is the development of vacuum deposition methods for the fabrication of perovskite thin films, and their incorporation into solar cells using different charge transport layers. Beyond the development of vacuum deposition of the perovskites themselves, interface engineering is regarded as a valid strategy to advance the perovskite solar cell performance. Hence, the influence of different charge transport layers and interfacial materials on the performance of perovskite solar cells is also studied in this thesis. The thesis has been structured in the following chapters:

- Preparation and characterization of mixed halide $MAPbI_{3-x}Cl_x$ perovskite thin films by three-source vacuum deposition:
  This chapter reports the fabrication of mixed halide perovskite solar cells. Optimizations have been done on three-source co-evaporation to achieve a mixed halide $MAPbI_xCl_{3-x}$.

- High voltage vacuum-processed perovskite solar cells with organic semiconducting interlayers:
  With the aim of reducing the non-radiative recombination, different electron transport layers where investigated. The effect of different ETLs as well as metal cathodes on the solar cell performance has been studied in this chapter.

- Efficient vacuum deposited p-i-n perovskite solar cells by front contact optimization:
  Interface engineering toward ohmic contact at the HTL/perovskite interface is described in this chapter.

Chapter 2.

Experimental method

2. Experimental method

2.1. Materials and pre-cursors

Several solar cell architectures have been prepared in this thesis. All devices were fabricated on top of pre-patterned indium tin oxide (ITO) covered glass substrates purchased from Julius. Molybdenum oxide (MoO_3), $PbCl_2$, PbI_2, MAI, BCP and lithium quinolate (Liq) were purchased from Lumtec. N4,N4,N4",N4"-tetra([1,1'-biphenyl]-4-yl)-[1,1':4',1"-terphenyl]-4,4"-diamine (TaTm) was provided by Novaled. C_{60} was purchased from Sigma-Aldrich.

2.2. Fabrication of perovskite solar cells

Perovskite films and charge transport layers can be deposited by solution processing or vacuum methods. There are several solution processing technologies available, however, the ease of control over the deposition parameters, such as deposition time, deposition rate, surface uniformity and precise layer thickness, make thermal vacuum evaporation a particularly promising technique to fabricate optoelectronic devices. The first thermal vacuum deposited perovskite device was reported by Mitzi et al.[87] Liu et al. used dual-source vacuum deposition of MAI and $PbCl_2$ and fabricated planar perovskite solar cells with efficiency of 15.4%.[88] In vacuum deposition, the organic cation and the metal halide are simultaneously thermally sublimated in a high vacuum chamber, where they solidify and react on a substrate placed above the thermal source (figure 14). The stoichiometry of the layer is controlled by adjusting the evaporation rate of the two (or more) precursors, giving real time control over the film thickness.[89]

In comparison to solution-processed techniques, vacuum deposition technique comes with a variety of benefits.

- **High film purity**: the high vacuum condition, sublimation of the precursors, and the solvent-free process ensure the deposition of highly pure films.
- **Versatile material choice:** Vacuum deposition provides the possibility to process virtually any type of inorganic and organic materials on an equally diverse variety of substrates and surfaces.

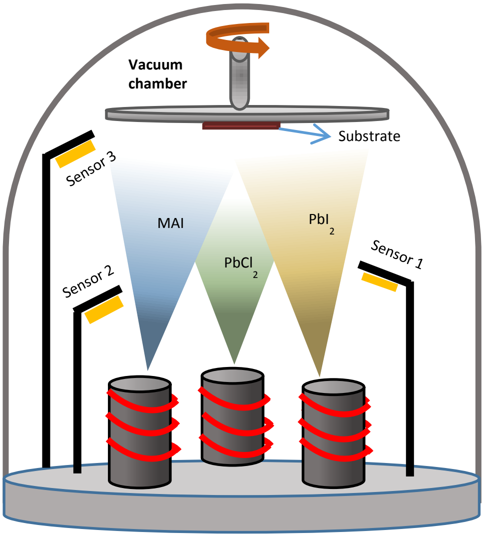

Figure 14. Schematic illustration of a vacuum chamber for the perovskite co-evaporation process. The precursors $PbCl_2$, PbI_2 and MAI are thermally evaporated in a vacuum chamber. Their rates are monitored using quartz microbalances.

- **Fine control of layer thickness:** To fabricate thin-film optoelectronic devices, nanometer precision in the layer thickness is needed. This can be achieved in a well calibrated system by means of monitoring precisely the deposition rate using quartz crystal microbalances (QCMs). QCMs function based on variation of their acoustic impedance as a consequence of the mass of materials deposited on it.

- **Possibility of up scaling and compatibility with different kind of substrate:** Evaporation techniques are widely used in semiconductor industry on various types of substrates.
- **Multilayer deposition possibility:** In comparison with other deposition techniques, such as solution based methods, thermal vacuum evaporation does not require any solvent which means that each layer can be processed on top of the anterior layer without the risk of damaging or removing it.

In this thesis all the layers were deposited by thermal vacuum techniques, and both two and three source co-evaporation methods have been employed to form the perovskite absorber layer (figure 14). As mentioned in chapter 1, a planar solar cell device consists of a perovskite absorber layer sandwiched in between charge transport layers. All the solar cells studied in this thesis have a p-i-n structure with the following stack architecture:

Glass/ITO/MoO_3/TaTm/perovskite/C_{60}/ETL/metal

Substrate preparation and film processing were carried out in a class 10000 cleanroom. The glass/ITO substrates have been cleaned primarily by soap, water and subsequently isopropanol in an ultrasonic bath. Then the substrates are treated by ultraviolet-ozone (UV-ozone). The substrates are subsequently transferred into a nitrogen-filled glovebox for thin-film deposition.

The MoO_3 (6 nm) and the TaTm (10 nm) layers were deposited at rates of 0.1 and 0.4 Å s^{-1}, respectively. For the perovskite deposition, MAI and PbI_2 were co-evaporated with rates of 1.0 and 0.6 Å s^{-1}, respectively, measured by two individual microbalance sensors. The total perovskite thickness was measured by a third sensor. For three source co-evaporation of MAI, PbI_2 and $PbCl_2$, the desired deposition rate of $PbCl_2$ was adjusted by varying the temperature from 265 °C to 285 °C. C_{60} was evaporated at a rate of 0.4 Å s^{-1} with the source temperature at 380 °C, and subsequently a thin layer (8 nm) of BCP was sublimed at a rate of 0.3 Å s^{-1} with a source temperature of 150 °C. Liq (2 nm) at the rate of 0.1 Å s^{-1}, Ba (5 nm) and Ag (100 or 200 nm) were evaporated in another vacuum chamber using molybdenum boats as sources by applying a current of 1 Å and 3-4 Å, respectively.

2.3. Film characterization techniques

Surface profilometry. Contact profilometer (Ambios XP-1) has been used to measure the thickness of the layers. Samples were scratched with a scalpel and cleaned with compressed nitrogen in order to remove residual particles originating from the scratch. Then the tip of the profilometer passed over the sample, crossing over the scratch in the film. This allows us to accurately measure the thickness.

UV-Vis absorption. The thickness that is determined by the profilometer can be confirmed by measuring the UV-Vis absorption, as the absorbance is proportional to the thickness of the layer. UV-Vis absorption measurements can also provide us with the information about the perovskite layer formation by considering the absorption edge vs. wavelength. Optical absorption measurements have been collected with an Avantes Avaspec-2048 spectrometer.

X-ray diffraction. The crystallinity of the vacuum deposited perovskite layers was analysed by X-ray diffraction which at room temperature on an Empyrean Panalytical powder diffractometer using the Cu kα_1 radiation.

Scanning electron microscopy (SEM). The surface morphology of the samples (pre-cut 0.5×0.5 cm^2) were analysed by SEM with a Hitachi S-4800 microscope operating at an accelerating voltage of 2 kV over Platinum-metallized samples. The accelerated electrons from the SEM interact with the sample and produce secondary electrons. The signal from the secondary electrons is collected by detectors to form the image.

X-ray photoemission spectroscopy (XPS). The elemental composition analysis has been done by XPS. In XPS, the material is irradiated with X-ray beams and XPS spectra are obtained by measuring the kinetic energy and the number of the electrons that escape from the surface of the sample. The XPS analyses have been done by means of XPS, K-ALPHA, Thermo Scientific. All spectra were collected using Al-K radiation (1486.6 eV), monochromatized by a twin crystal monochromator, yielding a focused X-ray spot. XPS data were analysed with Avantage software.

Kelvin probe measurement. To measure the surface potential of the layers we used a kelvin probe technique in air by KPTechnology (SKP5050). The configuration of this measurement consists of a conducting tip, air gap and a sample surface. The tip is vibrating and approaches (with a typical distance of 0.2-2.0 nm) the sample without touching the surface. The sample and the vibrating tip form a capacitor. The potential difference between the tip and the surface generates a charge on the probe tip. As the probe tip oscillates, the distance between the tip and the surface alters which (inversely) affects the capacitance. The changes in capacitance vary the charge on the probe tip that subsequently generates a measureable current which is used to calculate the potential difference between the tip and the sample. If the work potential of the metallic tip is constant, the surface potential of the sample can be determined.

Current-voltage measurement. Photovoltaic performance has been measured using an LED-powered light solar simulator (SINUS-70, Wavelabs) producing an AM1.5 spectrum at an intensity of 100 mWcm^{-2}. The active area of the devices is defined using metal mask with different openings of 0.0264, 0.05 and 0.0651 cm^{2}. In all cases average efficiencies reported are from more than 20 devices to ensure meaningful statistics. A Keithley source-measure unit was used to sweep the voltage from -0.2 V to 1.2 V, typically in 0.01 V steps with a scan rate of 0.3 Vs^{-1} whilst the output current is measured. Device parameters such as FF, J_{SC}, V_{OC} and PCE are then determined from the resulting JV curve, as explained in chapter 1. In chapter 5, light intensity dependence measurements were done by placing 0.1, 1, 10, 30, 80% neutral density filters (LOT-Quantum Design GmbH) between the light source and the device.

Maximum power point tracker (MPPT). To measure the lifetime of the solar cells under illumination (chapter 4), a maximum power point tracking system (MPPT), developed by Candlelight, was used. The cells were measured under constant white light from a light emitting diode (LED) source with illumination intensity equal to 1 Sun. Photovoltaic parameters were recorded at fixed time intervals (10 min) to deduce the evolution of the performance of the cells. MPPT provides information about the stability of the devices with the most similar real operation conditions. Furthermore, it helps to detect which parameter causes the decay of the power efficiency so that potential degradation mechanisms can be identified and subsequently prevented.

Time-resolved photoluminescence measurement (TRPL). In chapter 3, the carrier dynamics were examined by photoluminescence (PL) lifetime measurements. This type of measurements can be applied to describe various radiative and non-radiative loss channels for photo-generated carriers. The samples were prepared on glass substrate with the same condition used for the optimized devices (chapter 3). PL lifetime measurements (time-correlated) single photon counting, (TCSPC) were performed using an Edinburgh Instruments FLS1000 spectrometer. A three-component exponential decay was used to fit the TCSPC decays in the Fluoracle software package.

Chapter 3.

Preparation and characterization of mixed halide $MAPbI_{3-x}Cl_x$ perovskite thin films by three-source vacuum deposition

3. Preparation and characterization of mixed halide $MAPbI_{3-x}Cl_x$ Perovskite thin films by three-source vacuum deposition

3.1. Introduction

The latest generation of photovoltaic devices employing hybrid halide perovskites exhibits high PCE, exceeding 25%.[90] $MAPbI_3$ is the most widely studied hybrid perovskite in photovoltaics due to its simplicity and good semiconducting properties. The optoelectronic properties of $MAPbI_3$ can be further improved by introducing chloride ions. Interestingly, both $MAPbI_3$ and $MAPbI_{3-x}Cl_x$ thin films exhibit the same structural and optical properties while, when employed in solar cells, they show significantly different behavior. In spite of a large number of studies, both theoretical and experimental, the effect of chloride in mixed halide $MAPbI_{3-x}Cl_x$ perovskite solar cells remains unclear.[91–94] Some studies have estimated the diffusion length for $MAPbI_3$ and $MAPbI_{3-x}Cl_x$ thin films. It was shown that the diffusion length of $MAPbI_3$ thin films prepared by MAI and PbI_2 precursors is approximately 100 nm, while it was found to be as high as 1 µm when the perovskite was prepared from $PbCl_2$ and MAI.[16,95] The difference in charge diffusion lengths between $MAPbI_3$ and $MAPbI_{3-x}Cl_x$ was ascribed to a different morphology of the perovskite upon incorporation of Cl atoms.[49] However, some studies showed that the chloride does not effectively incorporate into the $MAPbI_3$ structure (below 3 to 4%) and acts only as a dopant. In fact, stable mixed iodide/chloride crystals cannot be formed due to the large difference between the ionic radii of iodine and chloride.[92] XPS measurements in agreement with density functional theory (DFT) calculations showed the segregation of chloride at the ETL/perovskite interface. In particular, DFT calculations reveal a bending of the $MAPbI_3$

conduction band at the interface with the ETL in the presence of Cl, which subsequently results in efficient electron extraction and superior device performance.[94] Other studies measured the charge mobility of $MAPbI_{3-x}Cl_x$ and $MAPbI_3$ showing an enhancement of the charge carrier mobility in the presence of chloride. They attributed these differences to a higher crystallinity of $MAPbI_{3-x}Cl_x$.[96,97]

Most $MAPbI_{3-x}Cl_x$ perovskite solar cells have been fabricated by solution processing.[13,24,48,98] The control of the concentration of MA-X and PbX_2 precursors is very important when preparing the mixed halide $MAPbI_{3-x}Cl_x$ perovskite by solution processing. It has been shown that the final Cl/I ratio in the $MAPbI_{3-x}Cl_x$ film is lower than in the precursor solution, which is likely due to low solubility of chloride into iodide perovskite.[92] In contrast to solution processing techniques, thermal vacuum deposition from multiple sources can be used to prepare mixed halide perovskite thin films with a superior control over the material stoichiometry.[99,100] Liu et al. reported the first thermally evaporated $MAPbI_{3-x}Cl_x$ solar cells using a large excess of MAI compared to the $PbCl_2$ precursor (MAI:$PbCl_2$ = 4:1). Due to the excess of MAI, a long thermal treatment (100 °C, 45 min) was needed to convert the as-deposited film to perovskite, with a substantial loss of chloride.[88]

To better control the $MAPbI_{3-x}Cl_x$ growth using discrete rates of I and Cl salts, we studied three-source vacuum co-deposition of MAI, $PbCl_2$ and PbI_2. In order to investigate the Cl-salt influence on the formation of the material, we varied the deposition rate of $PbCl_2$ while keeping the deposition rates of MAI and PbI_2 constant at 1 Å/s and 0.6 Å/s, respectively. We found that the most stable perovskite was obtained for a $PbCl_2$ deposition rate of 0.05 Å/s.

The SEM images of the mixed halide sample showed very uniform and pinhole-free films. These homogenous layers have been used to fabricate solar cells with the following stack: ITO/MoO_3/TaTm/$MAPbI_{3-x}Cl_x$/C_{60}/BCP/Ag. Remarkably, devices with high V_{OC} (> 1.1 eV) were obtained. As mentioned in chapter 1, defects have an important influence on determining the V_{OC} of the solar cell. Defects normally act as non-radiative recombination centers, which results in short carrier lifetime. To investigate the effect of chloride on the carrier recombination dynamics, we carried out PL lifetime measurements, and found a much longer lifetime for $MAPbI_{3-x}Cl_x$ films as compared to $MAPbI_3$. This suggests a reduction of non-radiative recombination in the mixed halide perovskite films deposited by three-source vacuum deposition.

3.2. Results and discussion

The presence of chloride on the surface of the sample was investigated by XPS. XPS with a penetration depth of a few nanometers is very suitable for surface composition studies. We found that the concentration of the chloride and iodide determined by XPS correlates with the ratio of the deposition rates of the PbI_2 and $PbCl_2$ precursors (PbI_2/$PbCl_2$: 0.6/0.05 Å s^{-1}). Figure 15.a-b shows the XPS spectra of the $MAPbI_{3-x}Cl_x$ thin film, highlighting the presence of chloride on the perovskite surface.

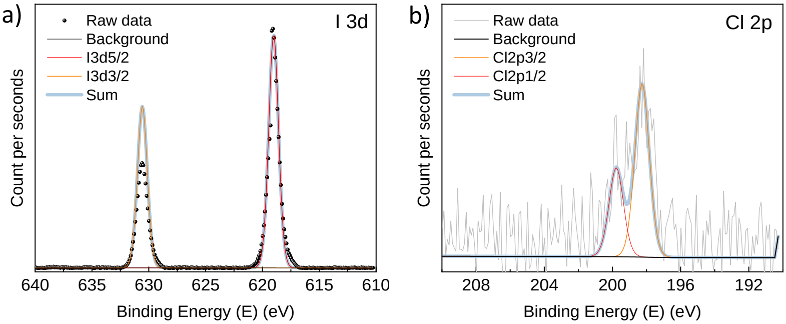

Figure 15. XPS spectra of (a) I 3d and (b) Cl 2p for a mixed halide $MAPbI_{3-x}Cl_x$ thin film.

The X-ray diffraction pattern (figure 16.a) shows highly crystalline $MAPbI_{3-x}Cl_x$ films with a tetragonal perovskite crystal structure, with the main peaks at 14.0° and 28.2°. However, there is an indication of the presence of small amounts of unreacted PbI_2 in the film, as highlighted in figure 16.a. The optical absorption spectrum (figure 16.b) shows an absorption onset at approximately 780 nm, analogous to that of $MAPbI_3$. Figure 16.c shows the SEM image of a $MAPbI_{3-x}Cl_x$ thin film, characterized by a pinhole-free and uniform morphology with grain size in the order of hundreds of nanometers.

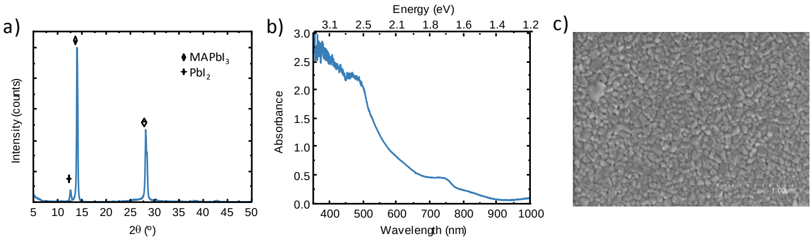

Figure 16. Characterization of perovskite films: a) XRD pattern, b) absorption spectrum of $MAPbI_{3-x}Cl_x$ thin films and c) top view SEM image of a $MAPbI_{3-x}Cl_x$ thin film.

Figure 17 shows the JV characteristics of solar cells under illumination. The solar cell stack has a p-i-n structure with mixed halide film sandwiched in between the MoO_3/TaTm as the HTLs and C_{60}/BCP as ETLs, capped with a silver electrode.

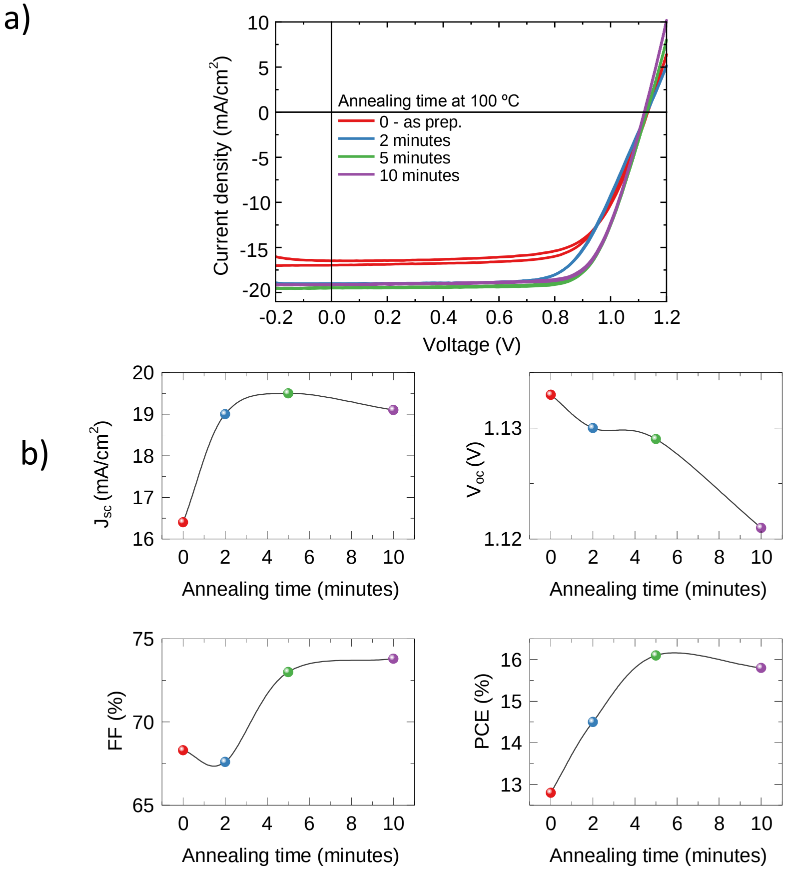

Figure 17. a) Electrical characterization under illumination for different perovskite annealing times. b) Summary of the photovoltaic parameters as a function of the annealing time at 100 °C.

By increasing the annealing time of the perovskite films after deposition, the current density was found to increase. As-prepared solar cells show a low current density (16.4 mA cm^{-2}) with a relatively low FF (68%), while annealing for 2 minutes, results in an increase of the photocurrent (J_{SC} = 19.0 mA cm^{-2}) accompanied with a minor loss in FF and V_{OC}. Longer annealing time (5 minutes) recovers the charge collection efficiency (FF = 73%), leading to an overall PCE of 16.1%. Further annealing mainly reduces the photovoltage, which is however still remarkable (1.12 V) for this type of absorber. It is worth to note that the initial V_{OC} is as high as 1.13 V, about 30 to 50 mV higher compared to state-of-the-art vacuum deposited $MAPbI_3$ solar cells.[74,101]

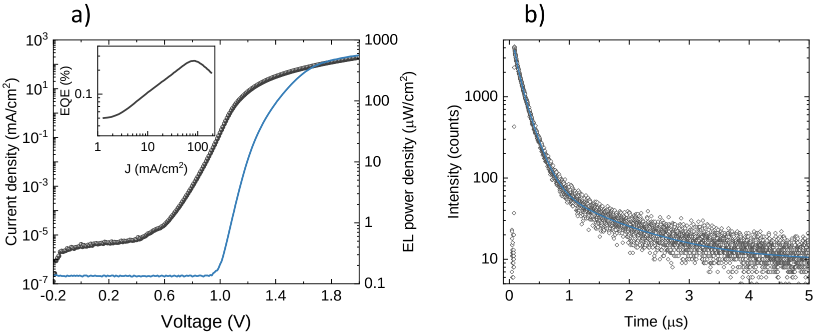

Figure 18. a) Current density (symbols) and electroluminescence power density (line) vs. the applied voltage for a $MAPbI_{3-x}Cl_x$ perovskite diode. Inset shows the EQE for electroluminescence as a function of the injected current density. b) Photoluminescence lifetime for a $MAPbI_{3-x}Cl_x$ film on glass, upon laser excitation at 375 nm. Raw data are symbols; the line is a fit with a tri-exponential function.

To investigate the electroluminescence of the solar cells, the best performing devices were characterized in an integrated sphere and maximum external electroluminescence quantum efficiency (EQE) of 0.3% was obtained (figure 18.a). The relatively high EQE indicates a suppression of non-radiative recombination pathways induced by the incorporation of chloride, most likely due to a reduction in the trap concentration.[102]

Figure 18.b shows the TRPL measurement of $MAPbI_{3-x}Cl_x$ films on quartz. The measured PL decay kinetics were fitted with a tri-exponential function, showing an average PL lifetime exceeding 300 ns, which is one order of magnitude larger than previously reported lifetimes for $MAPbI_3$ films (< 10 ns). These results are in agreement with the enhanced V_{OC} and with a reduction of the density of trap states in the presence of chloride.

3.3. Conclusion

Mixed halide $MAPbI_{3-x}Cl_x$ perovskite films were deposited by means of simultaneous co-evaporation of three precursors, MAI, PbI_2 and $PbCl_2$. Good crystalline and pinhole-free homogenous films have been obtained. Thin-film solar cells have been fabricated by employing mixed halide perovskite $MAPbI_{3-x}Cl_x$. The open-circuit voltage was found to be higher (1.13 V) as compared to pure $MAPbI_3$ vacuum-processed solar cells. The long photoluminescence lifetime (300 ns) and high EQE for electroluminescence (0.3 %) suggest a reduction of the non-radiative recombination rate. Controlled doping with chloride offers a novel opportunity to modify the hybrid perovskite materials improving the device performance, and makes the mixed halide perovskite a good candidate for vacuum deposited solar cells or near-Infrared LEDs.

COMMUNICATION

Energy Technolog
Generation, Conversion, Storage, Distributio
www.entechnol.d

Preparation and Characterization of Mixed Halide $MAPbI_{3-x}Cl_x$ Perovskite Thin Films by Three-Source Vacuum Deposition

Azin Babaei, Wiria Soltanpoor, Maria A. Tesa-Serrate, Selcuk Yerci, Michele Sessolo, and Henk J. Bolink*

Chloride is extensively used in the preparation of metal halide perovskites such as methylammonium lead iodide ($MAPbI_{3-x}Cl_x$), but its persistence and role in solution-processed materials has not yet been rationalized. Multiple-source vacuum deposition of perovskites enables a fine control over thin-film stoichiometry and allows the incorporation of chemical species irrespective of their solubility. Herein, the first example of mixed $MAPbI_{3-x}Cl_x$ thin films prepared by three-source vacuum deposition is presented using methylammonium iodide (MAI), PbI_2, and $PbCl_2$ as precursors. The optoelectronic properties of the material are evaluated through photovoltaic and electro-/photoluminescent characterizations. Besides the very similar structural and optical properties of $MAPbI_3$ and $MAPbI_{3-x}Cl_x$, an increased electroluminescence efficiency, longer photoluminescence lifetimes, as well as larger photovoltage, are observed in the presence of chloride, suggesting a reduction of nonradiative charge recombination.

Organic–inorganic (hybrid) metal halide perovskites are being studied as promising semiconductors for applications in photovoltaics (PVs) and light-emitting diodes (LEDs), due to their desirable properties, such as a high absorption coefficient, long carrier diffusion length, and high tolerance to chemical defects.[1–3] The global research efforts resulted in perovskite solar cells with a power conversion efficiency (PCE) exceeding 24%[4] and LEDs with an external quantum efficiency (EQE) of 20%, approaching its theoretical limit.[5–7] In addition, perovskites can be processed into thin films through a variety of low-temperature techniques, both from solution and from the vapor phase.[8–10] While most studies have been conducted on solution-processed compounds, likely due to the technical simplicity, vapor-phase deposition of perovskites has the advantage of being a solvent-free, intrinsically additive, and scalable process.[9] The archetypal perovskite compound, methylammonium lead iodide ($MAPbI_3$), was initially used as a mixed halide system with the addition of small amounts of chloride.[11] The mixed halide $MAPbI_{3-x}Cl_x$ was found to have a charge diffusion length exceeding 1 μm, about one order of magnitude longer compared with the pure iodide system.[12] Despite many investigations toward the role of chloride, its effect on the optoelectronic properties of $MAPbI_3$ remains poorly understood.[13] Chemical analysis found chloride to be segregated at the interface between $MAPbI_{3-x}Cl_x$ and the electron transport layer (ETL),[14] and in any case its solubility into the triiodide perovskite is extremely small ($x < 0.1$).[15] Interestingly, the first report of vacuum-deposited perovskite solar cells used $PbCl_2$ and methylammonium iodide (MAI) as the precursors, resulting in a mixed halide light absorber.[16] The process used a large excess of MAI ($MAI{:}PbCl_2 = 4{:}1$), and a long postannealing process (100 °C for 45 min in N_2) was needed to achieve full conversion to the perovskite phase. Most of the chloride is indeed lost during conversion of precursors to the perovskite. To circumvent the difficulties of obtaining a stoichiometrically controlled $MAPbI_{3-x}Cl_x$ through vacuum deposition, sequential techniques such as the vapor transfer method to convert the inorganic halide,[17] or single-source deposition of $MAPbCl_3$ followed by spin coating of MAI,[18] have also been explored. While technically more demanding, vacuum deposition from multiple sources offers a superior control over the final material stoichiometry and has been used to prepare mixed halide and mixed cation perovskite thin films.[19,20] Here we explore the vacuum deposition of $MAPbI_{3-x}Cl_x$ by coevaporation of the three precursors—PbI_2, $PbCl_2$, and MAI.

A. Babaei, Dr. M. Sessolo, Prof. H. J. Bolink
Instituto de Ciencia Molecular
Universidad de Valencia
C/Catedratico J. Beltrán 2, 46980 Paterna, Spain
E-mail: michele.sessolo@uv.es

W. Soltanpoor, Prof. S. Yerci
Centre for Solar Energy Research and Applications (GÜNAM)
Middle East Technical University
06800 Ankara, Turkey

W. Soltanpoor, Prof. S. Yerci
Department of Micro and Nanotechnology
Middle East Technical University
06800 Ankara, Turkey

Prof. S. Yerci
Department of Electrical and Electronics Engineering
Middle East Technical University
06800 Ankara, Turkey

Dr. M. A. Tesa-Serrate
Edinburgh Instruments
2 Bain Square, Kirkton Campus, EH54 7DQ Livingston, UK

The ORCID identification number(s) for the author(s) of this article can be found under https://doi.org/10.1002/ente.201900784.

DOI: 10.1002/ente.201900784

Perovskite films with homogenous morphology and high crystallinity are obtained and used in proof-of-concept solar cells with high photovoltage (>1.1 V). The increased open-circuit voltage (V_{oc}) is attributed to a reduced nonradiative recombination, as suggested by electroluminescence (EL) efficiency and photoluminescence (PL) lifetime measurements.

Glass slides with patterned indium tin oxide (ITO) were first coated by vacuum deposition with MoO_3 (5 nm) and a 10 nm-thick layer of *N*4,*N*4,*N*4′′,*N*4′′-tetra([1,1′-biphenyl]-4-yl)-[1,1′:4′,1′′-terphenyl]-4,4′′-diamine (TaTm), used as the hole transport layer (HTL). $MAPbI_{3-x}Cl_x$ films were prepared in a high vacuum chamber, using three different thermal sources, each equipped with a ceramic crucible and a quartz crystal microbalance (QCM) sensor, as schematically shown in **Figure 1**a.

Considering the reported low solubility of chloride in $MAPbI_3$,[15] we aimed at the lowest controllable deposition rate for $PbCl_2$ during the process. Hence, we fixed the $PbCl_2$ deposition rate at 0.05 Å s^{-1}, whereas PbI_2 was deposited at a rate of 0.6 Å s^{-1}. The MAI source was instead maintained at a fixed temperature (85 °C). After deposition, films were annealed in a nitrogen-filled glove box at 100 °C for different times. To assess whether chloride is retained into the film or is eliminated through the annealing process, we analyzed the sample surface by X-ray photoemission spectroscopy (XPS). As shown in Figure S1, Supporting Information, we did identify chloride on the surface of the samples, in a concentration of approximately ten times lower than iodide ($MAPbI_{3-x}Cl_x$ with $x \approx 0.3$), which correlates with the ratios between the deposition rate of $PbCl_2$ and PbI_2. We have to note, however, that the Cl2p electrons (with a binding energy of 200 eV) have an inelastic mean free path of ≈0.8 nm, which translates into a depth of analysis of ≈2–3 nm.[21] Hence we cannot exclude a different composition within the bulk of the perovskite film. The optical absorption spectrum (Figure 1b) shows the expected profile for $MAPbI_3$, with an onset at ≈780 nm (≈1.6 eV). The X-ray diffraction pattern reveals the presence of a small amount of unreacted PbI_2 in the films (12.7°, Figure 1c), as often observed for similar $MAPbI_3$ perovskite materials. However, the diffraction pattern for the tetragonal perovskite structure is clearly visible (main peaks at 14.0°, 28.2°), indicating that indeed highly crystalline $MAPbI_{3-x}Cl_x$ films can be obtained with our technique. The top-view scanning electron microscopy (SEM; Figure 1d) shows highly uniform and pin-hole-free films, with grain size in the order of hundreds of nanometers. These features are very similar to previously reported vacuum-deposited $MAPbI_3$ layers.[22]

The mixed halide films were further tested in a thin-film optoelectronic device, by vacuum processing of the ETLs. They consist of a bilayer of C_{60} fullerene (25 nm) and bathocuproine (BCP, 8 nm), capped with a silver electrode (100 nm).

The perovskite diodes were characterized under AM1.5G simulated illumination. We initially studied the trend of the PV parameters as a function of the $MAPbI_{3-x}Cl_x$ annealing time, as shown in Figure 1. The current density versus voltage (*J*–*V*) curves (**Figure 2**a) show good rectification and a marked trend with increasing annealing time. As-prepared samples show unusually low current density (16.4 mA cm^{-2}), accompanied

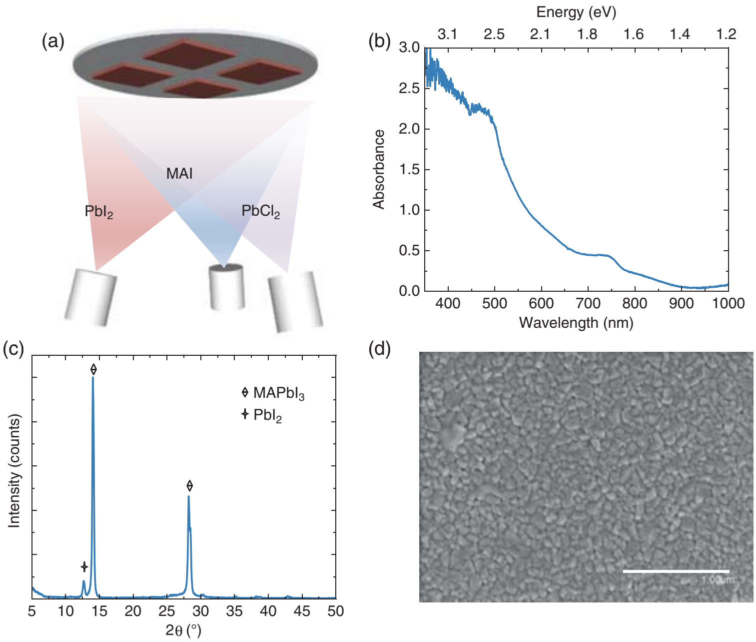

Figure 1. a) Schematics of the three-source vacuum deposition of $MAPbI_{3-x}Cl_x$ thin films. Characterization of perovskite films: b) absorption spectrum, c) XRD pattern, and d) SEM image of the sample surface.

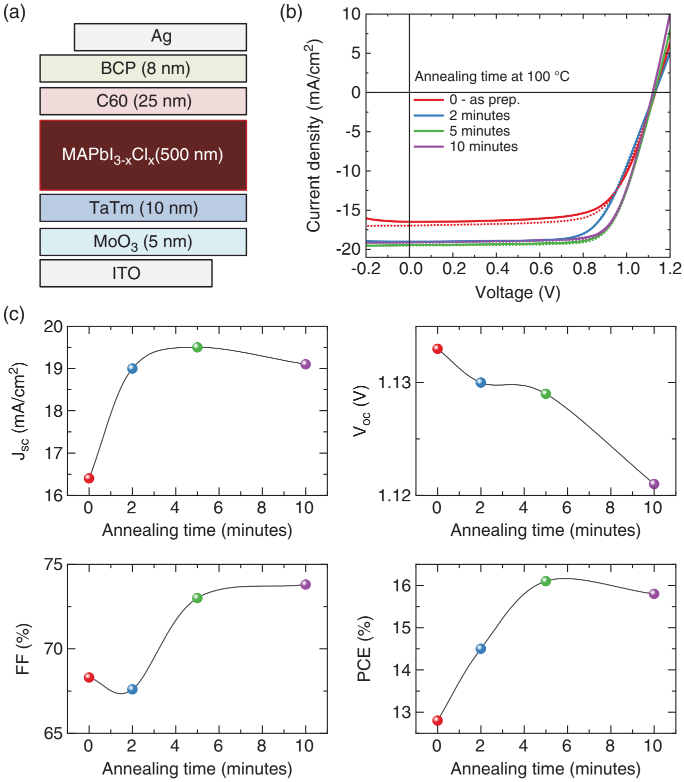

Figure 2. a) Scheme of the vacuum-deposited perovskite diode and b) its electrical characterization for different perovskite annealing temperatures; *J–V* curves under simulated solar illumination are reported in forward (from short to open circuit, solid lines) and reverse (from open to short circuit, dots) scans. c) A summary of the photovoltaic parameters as a function of the annealing time at 100 °C.

by a relatively low fill factor (FF) (68%). It is worth to note that V_{oc} is as high as 1.13 V, ≈30–50 mV higher compared with state-of-the-art vacuum-deposited $MAPbI_3$ solar cells.[22,23] Annealing the perovskite film for 2 min results in an enhancement of the photocurrent ($J_{sc} = 19.0\,mA\,cm^{-2}$), with only minor losses in terms of V_{oc} and FF. Longer annealing (5 min) substantially recovers the charge collection efficiency (FF = 73%), leading to an overall PCE of 16.1%. Furthermore, annealing mainly reduces photovoltage, which is however still remarkable (1.12 V) for this type of absorber.

The best-performing diode was further characterized in forward bias and in an integrating sphere to quantify its electroluminescence efficiency (**Figure 3**). The current density versus voltage profile (Figure 3a) shows a low current leakage at low bias, with steep injection between 0.6 and 1.1 V, indicating a high diode quality. EL is detected at ≈1.0 V, rising fast to reach ≈500 $\mu W\,cm^{-2}$ at 2.0 V applied bias. This corresponds to an EQE for EL of 0.3%, which is on par with the highest-performing vacuum-deposited $MAPbI_3$ diodes to date.[22]

The observation of a high EQE for electroluminescence suggests that the nonradiative recombination pathways are strongly suppressed by incorporation of chloride, in agreement with the literature on similar solution-processed perovskite films.[12] The lower nonradiative recombination might be caused by a reduction in the concentration of trap states, as a result of the incorporation of chloride at grain boundaries.[24] Hence we measured the time-resolved photoluminescence (TRPL) of $MAPbI_{3-x}Cl_x$ films on quartz to investigate the charge recombination dynamics. Figure 3b shows the TRPL trace measured at the maximum of the PL signal upon excitation with a picosecond-fast laser at 375 nm. The measured PL decay kinetics was fitted with a triexponential function of time, obtaining an average PL lifetime of 147 ns (see Supporting Information for details). The measured lifetime is one order of magnitude longer as compared with previously reported, vacuum-deposited, pure $MAPbI_3$ films,[25,26] which are typically characterized by very short PL lifetimes (<10 ns). Interestingly, the first fast component of the PL decay kinetics has a time constant of 63 ns, similar to previously reported dual-source vacuum-deposited $MAPbI_{3-x}Cl_x$ thin films.[27] The fastest decay observed in our materials might be related to different structural/morphological features, and also to the use of UV excitation, which preferentially probes

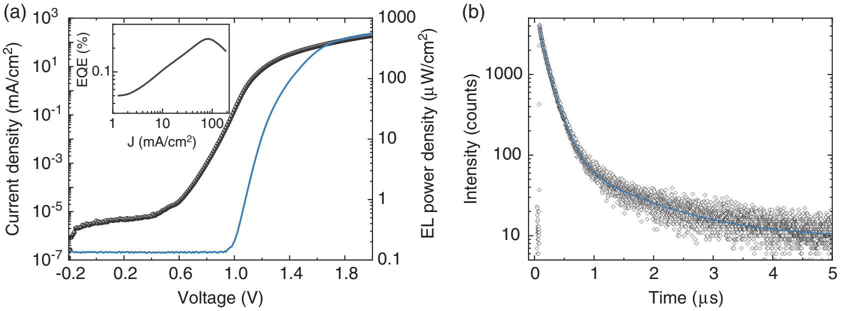

Figure 3. a) Current density (symbols) and electroluminescence power density (line) versus the applied voltage for the $MAPbI_{3-x}Cl_x$ perovskite diode. Inset shows the EQE for electroluminescence as a function of the injected current density. b) Photoluminescence lifetime for a $MAPbI_{3-x}Cl_x$ film on glass, upon laser excitation at 375 nm. Raw data are symbols; the line is a fit with a multiexponential function.

surface recombination. While care should be taken in deducing optoelectronic properties from TRPL, the longer PL lifetime suggests a reduction of the trap density or the presence of shallower trap states compared with pure $MAPbI_3$.[28] These observations are consistent with improvement in device performance, specifically enhanced V_{oc}, using the mixed halide perovskite layers, resulting from a decrease in nonradiative electron–hole recombination channels upon chloride incorporation.

In summary, we showed the formation of the mixed halide $MAPbI_{3-x}Cl_x$ perovskite by means of simultaneous coevaporation of the three precursors. Films showed good crystallinity and homogeneous morphology, a benchmark of vacuum-deposited perovskite films. We investigated the optoelectronic properties of the material by using in thin-film diodes. Under illumination, photovoltage is increased as compared with pure vacuum-processed $MAPbI_3$, reaching 1.13 V and PCE exceeding 16%. In forward bias, we detected intense electroluminescence with a quantum yield of 0.3%, similar to state-of-the-art evaporated perovskite solar cells. These observations, together with the long photoluminescence lifetime, make mixed halide perovskite a good candidate for efficient single-junction solar cells and NIR LEDs. Future studies will focus on the optimization of materials to achieve a higher PCE in both applications.

Experimental Section

Thin Film and Device Preparation: ITO-coated glass substrates were cleaned using soap, water, and isopropanol in an ultrasonic bath, followed by UV–ozone treatment. The substrates were transferred into a vacuum chamber integrated into a nitrogen-filled glove box (H_2O and O_2 <0.1 ppm) and evacuated to a pressure lower than 10^{-6} mbar. Three QCM sensors were used to monitor the deposition rate of the individual sources. For thickness calibration, we individually sublimed precursors, charge transport materials, and their dopants, comparing the thickness inferred from the QCM sensors with that measured using a mechanical profilometer. MoO_3 and TaTm layers were deposited at rates of 0.1 and 0.4 Å s^{-1}, respectively. The evaporation rates of the perovskite precursors were controlled by separate QCM sensors and adjusted to the desired deposition rate, with temperatures ranging from 265 °C to 285 °C for $PbCl_2$ and from ≈290 °C to 310 °C for PbI_2. The crucible-containing MAI was kept at a fixed temperature of 85 °C. After deposition of the perovskite film, C_{60} was evaporated at a rate of 0.4 Å s^{-1} with the source temperature at 380 °C, and subsequently a thin layer (8 nm) of BCP was sublimed at a rate of 0.3 Å s^{-1} with a source temperature of 150 °C. The devices were finished by deposition of silver as the top contact (100 nm thick).

Thin Film and Device Characterization: X-ray diffraction was measured with a Panalytical Empyrean diffractometer equipped with Cu–Kα anode operated at 45 kV and 30 mA and a Pixcel 1D detector in the scanning line mode. Single scans were acquired in the $2\theta = 10°–50°$ range in Bragg–Brentano geometry in air. Antiscatter slits of 1°/16° and step sizes of 0.025° were used for high-resolution diffractograms. Data analysis was performed with HighScore Plus software. The SEM images were performed on a Hitachi S-4800 microscope, operating at an accelerating voltage of 20 kV over platinum-metallized samples. Absorption spectra were collected using a fiber optics-based Avantes AvaSpec-2048 spectrometer. For the solar cell characterization, the *J–V* characteristics were obtained using a solar simulator by Abet Technologies (model 10500 with an AM1.5G xenon lamp as the light source). Before each measurement, the exact light intensity was determined using a calibrated Si reference diode equipped with an infrared cutoff filter (KG-3, Schott). The *J–V* curves were recorded between −0.2 and 1.2 V with 0.01 V steps, integrating the signal for 20 ms after a 10 ms delay. This corresponded to a speed of ≈0.3 V s^{-1}. The electroluminescence characterization was conducted using a Keithley Model 2400 source measurement unit and a sensitive Si photodiode coupled to an integrating sphere. Lifetime measurements (time-correlated single-photon counting, TCSPC) were performed using an Edinburgh Instruments FLS1000 spectrometer. The instrument was equipped with a double-emission monochromator, TCSPC electronics, a visible photomultiplier tube (PMT) detector, and a pulsed diode laser (EPL-375) as the excitation source. TCSPC decays were fitted using the standard Marquardt–Levenberg tail fit algorithm in the Fluoracle software package. A three-component exponential decay model was used for the fit.

Supporting Information

Supporting Information is available from the Wiley Online Library or from the author.

Acknowledgements

This work was supported by the Spanish Ministry of Economy and Competitiveness (MINECO) via the Unidad de Excelencia María de Maeztu MDM-2015-0538, MAT2017-88821-R, PCIN-2015-255, PCIN-2017-014, and the Generalitat Valenciana (Prometeo/2016/135). M.S. thanks the MINECO for his RyC contract. Financial support was also acknowledged from the Scientific and Technological Research Council of Turkey (TUBITAK) under the contract number 315M360.

Conflict of Interest

The authors declare no conflict of interest.

Keywords

halide perovskites, mixed halide perovskites, solar cells, vacuum deposition

Received: July 1, 2019
Revised: September 6, 2019

[1] T. M. Brenner, D. A. Egger, L. Kronik, G. Hodes, D. Cahen, *Nat. Rev. Mater.* **2016**, *1*, 15007.
[2] W. Li, Z. Wang, F. Deschler, S. Gao, R. H. Friend, A. K. Cheetham, *Nat. Rev. Mater.* **2017**, *2*, 16099.
[3] J. Huang, Y. Yuan, Y. Shao, Y. Yan, *Nat. Rev. Mater.* **2017**, *2*, 17042.
[4] M. A. Green, E. D. Dunlop, D. H. Levi, J. Hohl-Ebinger, M. Yoshita, A. W. Y. Ho-Baillie, *Prog. Photovoltaics Res. Appl.* **2019**, *27*, 565.
[5] K. Lin, J. Xing, L. N. Quan, F. P. G. de Arquer, X. Gong, J. Lu, L. Xie, W. Zhao, D. Zhang, C. Yan, W. Li, X. Liu, Y. Lu, J. Kirman, E. H. Sargent, Q. Xiong, Z. Wei, *Nature*, **2018**, *562*, 245.
[6] W. Xu, Q. Hu, S. Bai, C. Bao, Y. Miao, Z. Yuan, T. Borzda, A. J. Barker, E. Tyukalova, Z. Hu, M. Kawecki, H. Wang, Z. Yan, X. Liu, X. Shi, K. Uvdal, M. Fahlman, W. Zhang, M. Duchamp, J.-M. Liu, A. Petrozza, J. Wang, L.-M. Liu, W. Huang, F. Gao, *Nat. Photonics*, **2019**, *13*, 418.
[7] B. Zhao, S. Bai, V. Kim, R. Lamboll, R. Shivanna, F. Auras, J. M. Richter, L. Yang, L. Dai, M. Alsari, X.-J. She, L. Liang, J. Zhang, S. Lilliu, P. Gao, H. J. Snaith, J. Wang, N. C. Greenham, R. H. Friend, D. Di, *Nat. Photonics*, **2018**, *12*, 783.
[8] Z. Li, T. R. Klein, D. H. Kim, M. Yang, J. J. Berry, M. F. A. M. van Hest, K. Zhu, *Nat. Rev. Mater.* **2018**, *3*, 18017.
[9] J. Ávila, C. Momblona, P. P. Boix, M. Sessolo, H. J. Bolink, *Joule*, **2017**, *1*, 431.
[10] P. Luo, S. Zhou, W. Xia, J. Cheng, C. Xu, Y. Lu, *Adv. Mater. Interfaces*, **2017**, *4*, 1600970.
[11] M. M. Lee, J. Teuscher, T. Miyasaka, T. N. Murakami, H. J. Snaith, *Science*, **2012**, *338*, 643.
[12] S. D. Stranks, G. E. Eperon, G. Grancini, C. Menelaou, M. J. P. Alcocer, T. Leijtens, L. M. Herz, A. Petrozza, H. J. Snaith, *Science*, **2013**, *342*, 341.
[13] S. Colella, E. Mosconi, P. Fedeli, A. Listorti, F. Gazza, F. Orlandi, P. Ferro, T. Besagni, A. Rizzo, G. Calestani, G. Gigli, F. De Angelis, R. Mosca, *Chem. Mater.* **2013**, *25*, 4613.
[14] S. Colella, E. Mosconi, G. Pellegrino, A. Alberti, V. L. P. Guerra, S. Masi, A. Listorti, A. Rizzo, G. G. Condorelli, F. De Angelis, G. Gigli, *J. Phys. Chem. Lett.* **2014**, *5*, 3532.
[15] M. Bouchard, J. Hilhorst, S. Pouget, F. Alam, M. Mendez, D. Djurado, D. Aldakov, T. Schülli, P. Reiss, *J. Phys. Chem. C*, **2017**, *121*, 7596.
[16] M. Liu, M. B. Johnston, H. J. Snaith, *Nature*, **2013**, *501*, 395.
[17] Y. Liu, K. Feng, R.-H. Hsieh, X. Mo, *Mater. Lett.* **2019**, *239*, 163.
[18] J. Jang, G. Choe, S. Yim, *ACS Appl. Mater. Interfaces*, **2019**, *11*, 20073.
[19] G. Longo, C. Momblona, M.-G. La-Placa, L. Gil-Escrig, M. Sessolo, H. J. Bolink, *ACS Energy Lett.* **2018**, *3*, 214.
[20] L. Gil-Escrig, C. Momblona, M. G. La-Placa, P. P. Boix, M. Sessolo, H. J. Bolink, *Adv. Energy Mater.* **2018**, *8*, 1.
[21] P. J. Cumpson, *J. Electron Spectrosc. Relat. Phenom.* **1995**, *73*, 25.
[22] C. Momblona, L. Gil-Escrig, E. Bandiello, E. M. Hutter, M. Sessolo, K. Lederer, J. Blochwitz-Nimoth, H. J. Bolink, *Energy Environ. Sci.* **2016**, *9*, 3456.
[23] D. Pérez-del-Rey, L. Gil-Escrig, K. P. S. Zanoni, C. Dreessen, M. Sessolo, P. P. Boix, H. J. Bolink, *Chem. Mater.* **2019**, *31*, 6945.
[24] M. Abdi-Jalebi, Z. Andaji-Garmaroudi, S. Cacovich, C. Stavrakas, B. Philippe, J. M. Richter, M. Alsari, E. P. Booker, E. M. Hutter, A. J. Pearson, S. Lilliu, T. J. Savenije, H. Rensmo, G. Divitini, C. Ducati, R. H. Friend, S. D. Stranks, *Nature*, **2018**, *555*, 497.
[25] J. B. Patel, R. L. Milot, A. D. Wright, L. M. Herz, M. B. Johnston, *J. Phys. Chem. Lett.* **2016**, *7*, 96.
[26] I. Levine, S. Gupta, A. Bera, D. Ceratti, G. Hodes, D. Cahen, D. Guo, T. J. Savenije, J. Ávila, H. J. Bolink, O. Millo, D. Azulay, I. Balberg, *J. Appl. Phys.* **2018**, *124*, 103103.
[27] C. Wehrenfennig, M. Liu, H. J. Snaith, M. B. Johnston, L. M. Herz, *J. Phys. Chem. Lett.* **2014**, *5*, 1300.
[28] V. S. Chirvony, S. González-Carrero, I. Suárez, R. E. Galian, M. Sessolo, H. J. Bolink, J. P. Martínez-Pastor, J. Pérez-Prieto, *J. Phys. Chem. C*, **2017**, *121*, 13381.

Supplementary Information

Preparation and characterization of mixed halide $MAPbI_{3-x}Cl_x$ perovskite thin films by three-source vacuum deposition.

Azin Babaei[a], Wiria Soltanpoor[b,c], Maria A. Tesa-Serrate[d], Selcuk Yerci[b,c,e], Michele Sessolo[a],* and Henk J. Bolink[a]

[a] *A. Babaei, M. Sessolo, H. J. Bolink*
Instituto de Ciencia Molecular, Universidad de Valencia, C/Catedratico J. Beltrán
2, 46980 Paterna, Spain

[b] *W. Soltanpoor, S. Yerci*
Centre for Solar Energy Research and Applications (GÜNAM), Middle East Technical University, 06800 Ankara, Turkey

[c]*Department of Micro and Nanotechnology, Middle East Technical University, 06800 Ankara, Turkey*

[d] *Edinburgh Instruments, 2 Bain Square, Kirkton Campus, EH54 7DQ Livingston, United Kingdom*

[e] *Department of Electrical and Electronics Engineering, Middle East Technical University, 06800 Ankara, Turkey*

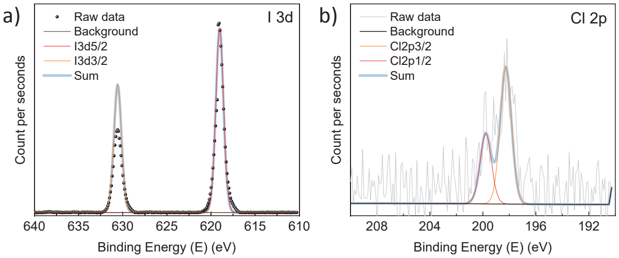

Figure 1s. XPS spectra of (a) I 3d and (b) Cl 2p for a mixed halide $MAPbI_{3-x}Cl_x$ thin film.

TRPL

The measured PL decay kinetics were fitted with a tri-exponential function of time (t):

$$I_{PL}(t) = a_1 \exp\left(-\frac{t}{\tau_1}\right) + a_2 \exp\left(-\frac{t}{\tau_2}\right) + a_3 \exp\left(-\frac{t}{\tau_3}\right)$$

We found:

$\tau_1 = 63$ ns with amplitude $a_1 = 1365$

$\tau_2 = 172$ ns with amplitude $a_2 = 2346$

$\tau_3 = 1078$ ns with amplitude $a_3 = 93$

The average lifetime (τ_{avg}) was calculated as:

$$\tau_{avg} = \frac{\sum a_i \tau_i^2}{\sum a_i \tau_i} = 311\ ns$$

Chapter 4.

High voltage vacuum-processed perovskite solar cells with organic semiconducting interlayers

4. High voltage vacuum-processed perovskite solar cells with organic semiconducting interlayers

4.1. Introduction

Hybrid lead halide perovskites are being widely used as absorber layers in solar cells due to their desirable properties, such as high absorption coefficient, long carrier diffusion length and high tolerance to chemical defects.[8,103,104] $MAPbI_3$-based solar cells have the benefit of being easy to process with different methods while exhibiting high power conversion efficiency.[74,88,105–107] In general, when designing the device structure, appropriate charge transport layers need to be selected to ensure a high V_{OC} and high FF of the solar cells. As detailed in chapter 1, ETLs and HTLs are responsible for the transport and extraction of electrons and holes within the device. The choice of a suitable ETM is of a particular importance for the V_{OC} and FF of the solar cell, as it influences the charge recombination and rectification of the device.

To date, several ETLs have been used and studied in perovskite solar cells.[62,63,75,84,108] Among them, fullerene and its derivatives have been mostly used due to their favourable characteristics. Fullerenes efficiently transport electrons and can also passivate trap states on the surface of perovskites.[109,110]

In order to achieve high performance perovskite solar cells, ETM should fulfil several criteria. The ETM needs to have LUMO and HOMO matched with the conduction and valence bands of the perovskite to efficiently and selectively transport electrons. Moreover, the LUMO of the ETM requires matching with the work function of the metal electrode to facilitate electron collection. For this purpose, one approach is the use of low work function electrodes such as barium or calcium in p-i-n structure.[79,111] Another way is to use an interlayer between the ETL and the metal electrode. BCP, an organic semiconductor with a band gap of about 3.5 eV, is a widely used interlayer in combination with fullerenes and Ag or Al, and can be easily deposited in thin films by thermal evaporation.[76,78,112,113] While the working mechanism of electron transfer through BCP is still a matter of debate, it has been reported that BCP and Ag/Al can form organometallic complexes leading to a new density of electronic states below the LUMO of pristine BCP, mediating the charge transport. Another interlayer which was used in this chapter is Liq, which has HOMO and LUMO energies at -5.6 eV and -3.2 eV, respectively.[114] Liq can be thermally evaporated and is commonly used in OLEDs as an electrode interlayer. It has been shown that Liq can form radical anions upon reacting with metal contact, favouring electron injection in OLEDs.[115]

In this chapter we investigated the effect of these interlayers, specifically BCP and Liq or the combination of them, on the performance of perovskite solar cells. The top electrode used in this chapter is either Ba or Ag and the overall effect of each top contact on the V_{OC} and the stability of the perovskite solar cells are discussed. The following device stack was used in this chapter: ITO/MoO_3/TaTm/$MAPbI_3$/C_{60}/EIL/metal (figure 19). All the layers were prepared by thermal evaporation in high-vacuum chambers.

4.2. Result and discussion

Five different combinations of interlayers and metals have been studied. Figure 19 shows the schematics of the devices as well as the flat band energy diagram of the materials used. The JV curves under AM 1.5G simulated illumination at the intensity of 100 mW cm^{-2} of the finished devices are depicted in figure 20.a. All solar cells showed a similar J_{SC} of approximately 20.5 mA cm^{-2} and hysteresis-free JV curves which is an indication of well-matched energy levels among different materials. A high V_{OC} (1.13 V) with good rectification (FF of 77.6%) was obtained for the internal reference device with BCP/Ag top contact. It is worth mentioning that the V_{OC} achieved for the internal reference device with BCP/Ag top contact in this chapter is larger compared to that reported in chapter 3 for the same perovskite solar cell structure. This difference originates from the optimization of the $MAPbI_3$ vacuum-deposition process.

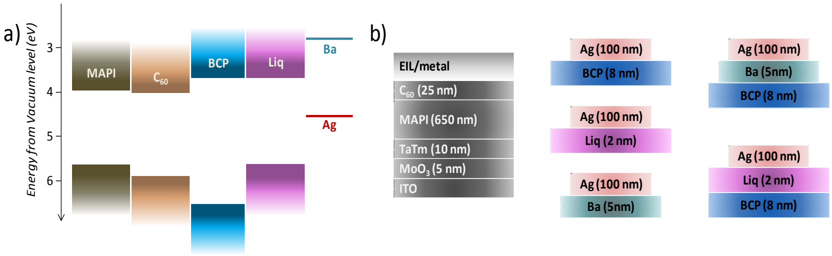

Figure 19. (a) Flat band energy diagram of the materials used as electron transport/injection layers and electrodes. (b) Device schematics with thickness of all layers and highlight of the five different device structures studied in the paper.

The photovoltaic parameters remain unchanged when replacing BCP by Liq, resulting in devices with V_{OC} of 1.13 V and a PCE of 18.1% on average. The lower V_{OC} (1.11 V) and FF of 67.1% were obtained for the devices employing BCP in combination with the low work function Ba top electrode. The Low FF is related to limited charge extraction, most likely due to an unfavourable interaction between BCP and Ba. The overall efficiency of the device incorporating BCP and Ba is 15.7%, as a result of the low

FF and V_{OC}. The diodes with a BCP/Liq/Ag top contact exhibited a V_{OC} of 1.12 V, slightly higher compared to those with BCP/Ba/Ag, but with FF's as high as 80%, indicating a better rectification. As the thickness of Liq is small (2 nm) in this device configuration, it might be possible that the chemical interaction between BCP and Ag still takes place, resulting in better charge extraction and higher FF.

The highest V_{OC} (1.15 V) was detected for the devices with Ba electrode directly deposited on the C_{60} ETL, with only a small drop in FF. Table 1 summarizes the average photovoltaic parameters of all devices with different top contacts which were extracted from the JV curves.

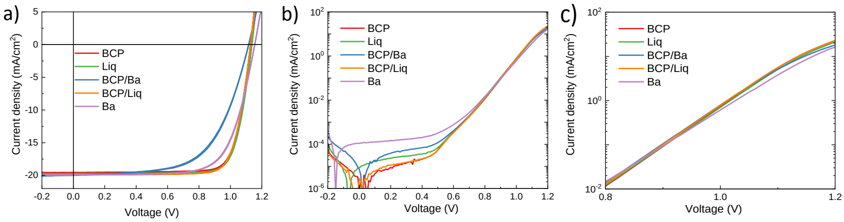

Figure 20. (a) Representative JV curves measured under simulated solar illumination in forward (short to open circuit) and reverse (open to short circuit) scan direction for each studied device. Due to the lack of hysteresis the two scans are indistinguishable. (b) JV characteristics collected in the dark with (c) highlight of the transition between the diffusion and drift current regimes. No substantial differences in built-in potential can be observed.

Figure 20.b shows the dark JV characteristics of the solar cells with different top contacts. The observed trends in photovoltage are not related with the diode dark JV curves, where all the solar cells show rather low and comparable leakage current in low voltage regime. There are several hypotheses to explain the differences between the values of V_{OC} in the different devices.

One reason could be a variation in diode built-in potential, which might help to extract the majority of electrons from the $MAPbI_3/C_{60}$ interface. However, in the dark JV curves (figure 20.c) there is no appreciable difference in the built-in potential as a function of the interlayer used.

Top contact	FF (%)	V_{OC} (V ± mV)	J_{SC} (mA cm^{-2})	PCE (%)
BCP	77.8 ± 2.8	1.13 ± 3	20.5 ± 0.1	18.1 ± 0.2
Liq	77.6 ± 1.9	1.13 ± 4	20.4 ± 0.3	18.1 ± 0.3
BCP/Ba	67.1 ± 1.9	1.11 ± 2	20.7 ± 0.5	15.7 ± 0.1
BCP/Liq	78.3 ± 0.2	1.12 ± 6	20.6 ± 0.7	18.4 ± 0.2
Ba	71.8 ± 1.8	1.15 ± 7	20.7 ± 0.7	17.1 ±0.6

Table 1. Average photovoltaic parameters with standard deviation σ extracted from JV curves for solar cells with different top contact.

In optoelectronic devices, non-radiative recombination reduces the quasi-Fermi-level splitting (QFLS), and hence limits the attainable V_{OC}. As in perovskites recombination takes place from free charge carriers, the QFLS can be directly related to the perovskite photoluminescence quantum yield.[116] With this in mind, we performed PL measurements on full solar cells in an integrated sphere, illuminating the device with a 515 nm laser. To ensure having the same carrier concentration for all devices, we adjusted the laser power so that the J_{SC} of the cells matched the one obtained under simulated solar illumination. Figure 21.a shows the PL spectra of all the devices with different top contacts, exhibiting a maximum centred at 1.58 eV, regardless of the top contact. The maximum intensity of the PL peak belongs to the device with Ba top contact coated directly on C_{60}, which indicates that the work function of Ba has a positive influence on the charge carrier recombination in the solar cell.

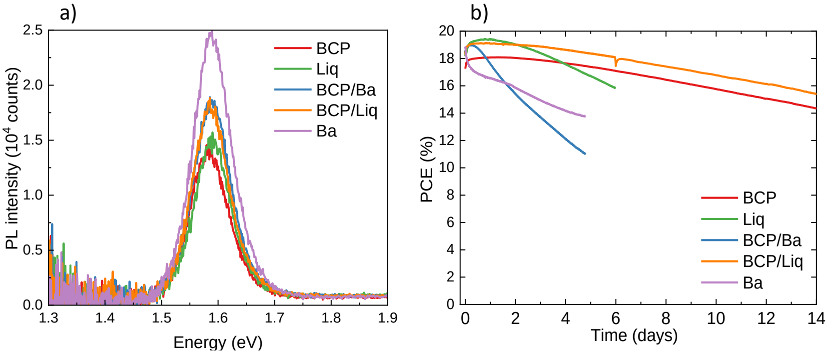

Figure 21. (a) Steady-state PL spectra of devices with different top contacts, excited with a 522 nm laser at the intensity equivalent to 1 sun illumination. (b) Evolution of the PCE of devices with different top contacts under continuous simulated solar illumination.

Devices with Liq and BCP showed the lowest PL intensity, although they were characterized by a high V_{OC}, while devices employing BCP/Liq and BCP/Ba resulted in brighter PL. These observations suggest that the final photovoltage is determined by different competitive mechanisms. Interestingly, both the work function of the electrode and type of interlayer can influence the PL of the $MAPbI_3$. One hypothesis to explain this is the alteration of the $MAPbI_3$ film work function directly by the top surface. However, the direct measurement of the work function of these materials is difficult as the interface is buried within the device. It has been already reported that the perovskite Fermi level can be modulated by changing the substrate. For instance, p-type substrates induce a p-type character on the perovskite itself.[57,117,118] Hence we can assume that the Fermi level of $MAPbI_3$ is influenced also by the top contact.

The stability of the perovskite solar cells was also evaluated by measuring their power output under illumination and over time. To measure the lifetime, the devices were encapsulated with UV-curable resin and a glass slide, and were analysed under a constant nitrogen flow at 25°C. The current-voltage curves were recorded automatically every 10 min. The evolution of the PCE over time for the device series is depicted in figure 21.b. Devices employing Ba as the electrode (either alone or in combination with BCP) show an initial fast rise in efficiency (to about 19%) followed by a relative fast decay. This is expected as Ba is extremely reactive, and hence a more rigorous encapsulation is needed to avoid the presence of oxygen and/or moisture. Similar decay profiles but with much longer stability was observed for devices employing BCP and BCP/Liq in combination with the Ag electrode. The device employing the thin Liq interlayer in between C_{60} and Ag showed an initial increase of efficiency (up to 19.5% after 1 day) again followed by a slow decay, reaching about 16% after 6 days of operation. Several mechanisms responsible for the degradation of perovskite solar cells have been proposed, such as compositional degradation, halide and metal ion migration.[119–121] Among them, the main processes driving the degradation of perovskite solar cell is the diffusion of halides to the electrode, as well as the opposite migration of metal atoms from the electrode the perovskite film.[122,123] Considering this, the short lifetime for the solar cells with a thin (2 nm) layer of Liq in between the C_{60} and the Ag might be related with a faster interdiffusion of species between the electrode and the $MAPbI_3$ film. The additional barrier provided by BCP can alleviate this effect, resulting in the longer lifetimes observed here.

4.3. Conclusion

We studied the effect of different interlayers, electrodes, and their combinations on the performance of vacuum processed $MAPbI_3$ solar cells. Two organic semiconductors, BCP and Liq as electron transport materials were used in this chapter. Organic semiconductors traditionally used in solar cells (BCP) and OLEDs (Liq) can lead to devices with high rectification, fill factor, and photovoltage. We also observed how the non-radiative recombination reduces when exchanging Ag top contact with a low work function metal, such as Ba. However, the device stability drops in this case as a consequence of the higher reactivity of the metal. Long-term device stability was observed only in the presence of BCP, with or without the Liq buffer layer. More studies should be carried out to understand the interplay of metals and interlayers and their effect on the performance and lifetime of perovskite solar cells.

RSC Advances

ROYAL SOCIETY OF CHEMISTRY

PAPER

View Article Online
View Journal | View Issue

Check for updates

Cite this: *RSC Adv.*, 2020, **10**, 6640

High voltage vacuum-processed perovskite solar cells with organic semiconducting interlayers†

Azin Babaei, Chris Dreessen, Michele Sessolo* and Henk J. Bolink

Received 8th January 2020
Accepted 4th February 2020

DOI: 10.1039/d0ra00214c

rsc.li/rsc-advances

In perovskite solar cells, the choice of appropriate transport layers and electrodes is of great importance to guarantee efficient charge transport and collection, minimizing recombination losses. The possibility to sequentially process multiple layers by vacuum methods offers a tool to explore the effects of different materials and their combinations on the performance of optoelectronic devices. In this work, the effect of introducing interlayers and altering the electrode work function has been evaluated in fully vacuum-deposited perovskite solar cells. We compared the performance of solar cells employing common electron buffer layers such as bathocuproine (BCP), with other injection materials used in organic light-emitting diodes, such as lithium quinolate (Liq), as well as their combination. Additionally, high voltage solar cells were obtained using low work function metal electrodes, although with compromised stability. Solar cells with enhanced photovoltage and stability under continuous operation were obtained using BCP and BCP/Liq interlayers, resulting in an efficiency of approximately 19%, which is remarkable for simple methylammonium lead iodide absorbers.

1 Introduction

Organic–inorganic lead halide perovskites are being widely studied in thin-film optoelectronics and especially photovoltaics,[1] in view of their good semiconducting properties.[2] They typically exhibit a high absorption coefficient, long carrier diffusion length, high tolerance to chemical defects, and they can be prepared as high quality thin-films through a variety of deposition techniques.[3] In particular, perovskite thin-films can be readily prepared by solution processing or vacuum methods at low temperature, which is desirable when scaling up the device fabrication.[4,5] In perovskite solar cells, the photogenerated charge carriers need to be efficiently and selectively transported to the electrodes, minimizing non-radiative charge recombination. For this reason, the perovskite film is typically sandwiched in between organic or inorganic semiconductors, acting as electron and hole transport layers (ETL and HTL, respectively).[6] Several studies have been focused on the understanding of charge transfer and interfacial processes between the perovskite, the ETLs, and the electrode, with the ultimate goal of maintaining a high charge collection efficiency and to abate non-radiative charge recombination.[7] Among ETLs, notable examples are n-type metal oxides,[8] in particular TiO_2 and SnO_2, while the most widely adopted organic semiconductors are fullerene derivatives.[9] Fullerenes cannot only selectively transport electrons between the perovskite and the electrode, but are also capable to effectively passivate trap states and mitigate ionic migration at the perovskite surface and at the grain boundaries.[10] Efficient electron extraction, ensuring high open-circuit voltage (V_{oc}) and fill factor (FF), requires matching of the lowest unoccupied molecular orbital (LUMO) of the fullerene with the electrode work function. In a first approximation, this can be simply attained by using low work function electrodes such as calcium or barium,[11,12] although stable metals (Ag, Au) can also lead to ohmic contacts with fullerenes due to the formation of interfacial dipoles.[13,14] Another approach to reduce the energy mismatch between a semiconductor and an electrode is to increase the charge-carrier density in the organic semiconductor through doping.[15–17] In p–i–n perovskite solar cells employing fullerene ETLs, typically C_{60} or 1-[3-(methoxycarbonyl)propyl]-1-phenyl-[6.6]C_{61} (PCBM), ohmic injection is ensured by depositing a thin interlayer between the ETL and the electrode. This includes different molecules such as 1,3,5-tri(*m*-pyrid-3-yl-phenyl)benzene (TmPyPB)[18] or (2-(1,10-phenanthrolin-3-yl)naphth-6-yl) diphenylphosphine oxide (DPO),[19] inorganic salts such as LiF,[20] or n-type metal oxides.[21,22] The most widely adopted interlayer is a thin (5–10 nm) film of 2,9-dimethyl-4,7-diphenyl-1,10-phenanthrolin (bathocuproine, BCP), which is sublimed onto C_{60} and covered with a silver or aluminium electrode. BCP is a wide band gap material with a deep highest occupied molecular orbital (HOMO, >6.5 eV) and shallow LUMO (3–3.5 eV, Fig. 1a), which makes it suitable as exciton-blocking layer in organic electronics.[23–27] By simply considering the flat band energy diagram in Fig. 1a, BCP would not appear as

---

Instituto de Ciencia Molecular, Universidad de Valencia, C/Beltrán 2, Paterna, 46980, Spain. E-mail: michele.sessolo@uv.es

† Electronic supplementary information (ESI) available. See DOI: 10.1039/d0ra00214c

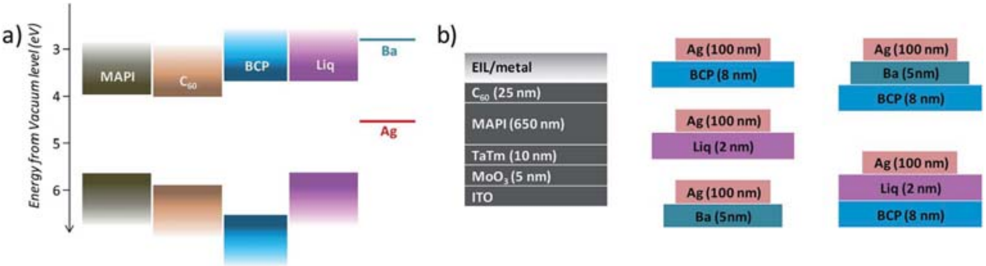

Fig. 1 (a) Flat band energy diagram of the materials used as electron transport/injection layers and electrodes. (b) Device schematics with thickness of all layers and highlight of the five different device structures studied in the paper.

a rational choice to match the energy levels of C_{60} and Ag, as its small electron affinity would hinder both the electron injection and extraction at the C_{60}/Ag interfaces. However, several reports have shown a strong chemical reaction occurring upon thermal vacuum deposition of Ag onto the BCP, and leading to the formation of Ag-BCP organometallic complexes.[24,28] These compounds would mediate charge transport due to the formation of new states well below the LUMO of pristine BCP, which justifies the efficient electron injection/extraction properties of BCP in optoelectronic devices.[25] This widely accepted view is challenged by recent reports where BCP was found to efficiently mediate electron transfer when placed in between an indium tin oxide (ITO) electrode and C_{60}, where the formation of organometallic species is unlikely.[29] In perovskite solar cells, non-radiative recombination is dominant at dislocations, grain boundaries, impurities as well as at the contact interface, and in all cases it unavoidably diminishes the attainable open-circuit voltage.[30] Non-radiative recombination in the perovskite layer can be regulated through controlled film crystallization/processing, while interface recombination should be minimized through the choice of suitable transport materials and optimized device architectures.[31] The influence of interlayer chemical and electronic properties on transport and recombination in vacuum-deposited perovskite solar cells has not been fully investigated, although it is critical to modulate and maximize FF, V_{oc} and stability. Here we studied the influence of interlayers and cathode work function at the C_{60} interface in vacuum-deposited p–i–n perovskite solar cells. In particular, we compared BCP with 8-hydroxyquinolinolato-lithium (Liq, Fig. 1a), a common electrode interlayer used in high efficiency organic light-emitting diodes (OLEDs).[32] Liq has HOMO and LUMO energies of −5.6 eV and −3.2 eV from the vacuum level, respectively,[33] and has the advantage of being easily processed by thermal evaporation or solution.[34,35] As for the case of BCP, the electron injection mechanism of Liq is not completely understood, but the most accepted hypothesis is that it is able to release metallic lithium upon reaction with the metallic cathode, leading to interfacial reduction of the underlying ETL.[36,37] In this work, we compared fully vacuum-deposited MAPI solar cells employing organic semiconductors as the transport and injection materials. We examined the influence of different thin electron injection layers and of the metal work function on the performance of p–i–n solar cells, where the electron transport layer is deposited on top of the perovskite and before the metal electrode. We compared the performance of the devices using BCP, Liq or combinations of them, using either Ag or Ba as the top electrode. We identified that while low work function metals can enhance the open-circuit voltage, they do it at the expense of the fill factor and especially of the stability. Using bare BCP or a combination of BCP and Liq led to solar cells with improved rectification, high photovoltage, and long-term stability.

2 Results and discussions

Details of preparation and characterization of materials and devices are reported in the experimental section. Briefly, we processed a 650 nm thick MAPI film and employed it in the fabrication of p–i–n perovskite solar cells. All layers were prepared by vacuum sublimation of the corresponding inorganic or organic materials in high-vacuum chambers. A scheme of the device structure is reported in Fig. 1a. A thin layer of molybdenum oxide (MoO_3, 5 nm) was deposited onto pre-patterned ITO-coated glass slides, acting as hole injection layer (HIL). As the HTL we used a 10 nm thick N^4,N^4,$N^{4''}$,$N^{4''}$-tetra([1,1′-biphenyl]-4-yl)-[1,1′:4′,1″-terphenyl]-4,4″-diamine (TaTm) film, while C_{60} was used in all cases as the ETL on top of the perovskite. We then finished the devices using 5 different variations of interlayers and metals (Fig. 1b), namely BCP (8 nm)/Ag, Liq (2 nm)/Ag, Ba (5 nm)/Ag, and the combinations BCP (8 nm)/Ba (5 nm)/Ag and BCP (8 nm)/Liq (2 nm)/Ag, where Ag is 100 nm thick in all cases. The latter two combinations were chosen to assess whether BCP can be used in combination with a low work function metal (Ba), or when not in contact with Ag (using a Liq interlayer). To ensure sufficient statistics, for each device configuration, at least 2 different substrates each containing 4 cells were evaluated, while for top performing configurations at least 5 different substrates with a total of 20 cells were characterized. The overlap area between the metal and ITO electrode was 6.51 mm^2 (2.1 × 3.1 mm^2) and the solar cell characteristics were measured under illumination with a 4 mm^2 mask to accurately determine the short circuit current (J_{sc}), and without a mask to avoid erroneous determination of both open-circuit voltage and fill factor.[38]

We initially tested the optoelectronic properties of the devices by measuring the current density–voltage (*J*–*V*) curves under AM 1.5G simulated sun illumination at the intensity of 100 mW cm^{-2} (Fig. 2a and Table 1). Very small and negligible differences were observed between forward (from short to open circuit) and reverse (from open to short circuit) scans. The lack of hysteresis in the *J*–*V* curves suggests that no charge accumulation takes places at the perovskite/transport layers' interface, indicating good energy level matching among the different materials. All solar cells were characterized by a similar J_{sc} of approximately 20.5 mA cm^{-2}, which is reasonable as all devices share the exact same stack of materials at the front contact, and the internal field is sufficient to overcome eventual energy barriers induced by the use of different ETLs. The internal reference device with BCP/Ag top contact delivered a high V_{oc} of 1.13 V with good rectification (FF of 77.6%), resulting in a PCE of 18.1% on average. When exchanging BCP for Liq, we observed that the photovoltaic parameters are essentially unvaried, leading to a V_{oc} of 1.13 V and a PCE of 18.1% on average. Devices employing BCP in combination with the low work function Ba electrode exhibited a low FF (67.1%) suggesting hindered charge extraction, despite of the ohmic BCP/Ba electron transport interface. Most likely, with this device structure the electron extraction is limited by the large potential difference between the LUMOs of C_{60} and BCP, and there is no beneficial interaction between BCP and Ba, as often reported for BCP in combination with Ag and Al. This is an additional indirect evidence that indeed metals such as Ag and Al do interact with BCP leading to the formation of new species and of an additional density of states below the BCP LUMO, as described above. The V_{oc} was also found to be slightly lower (1.11 V), and the overall efficiency was 15.7%. More interesting is the other device variation where we included Liq as interlayer between BCP and Ag. The diodes with BCP/Liq/Ag top contact exhibited a $V_{oc} = 1.12$ V, slightly higher compared to those with BCP/Ba, but with a much better rectification, as the FF approached 80% with small pixel-to-pixel variation. The latter observation might suggest that the chemical interaction between BCP and Ag takes place even in the presence of the Liq interlayer, due to its very low thickness (2 nm).

Finally, the solar cells employing the top Ba electrode deposited directly on the C_{60} ETL delivered the highest V_{oc} of 1.15 eV, even though at the price of a small decrease in FF. The observed trends in photovoltage were not related with the diode dark *J*–*V* characteristics (Fig. 2b), where all solar cells showed rather low and comparable leakage current in the low voltage regime. In this regime, the minimum of the current density for devices with Ba and Liq appeared at low negative voltage, indicating a small carrier accumulation within the device. Only devices finished with Ba were found to have a slightly higher

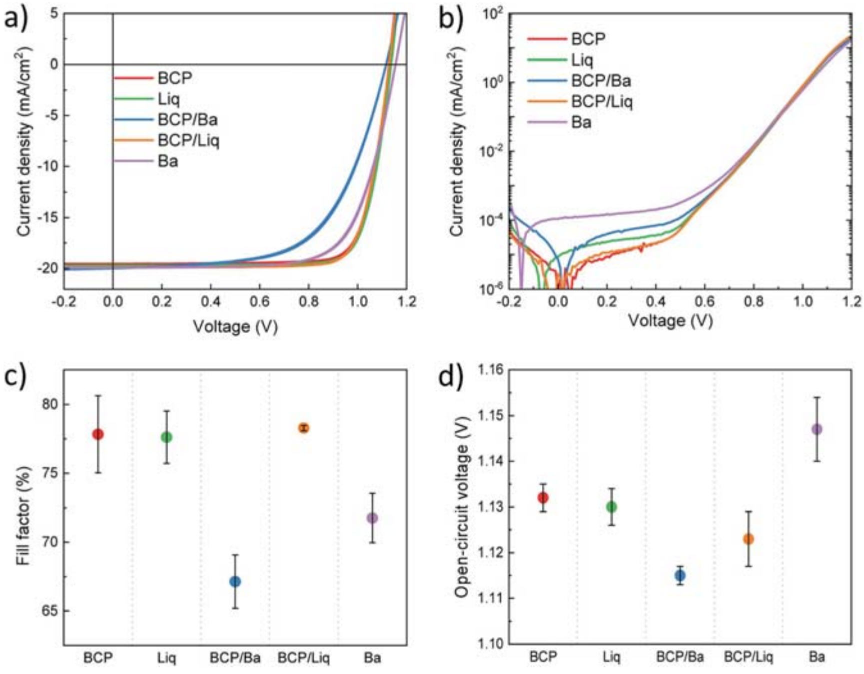

Fig. 2 (a) Representative *J*–*V* curves measured under simulated solar illumination in forward (short to open circuit) and reverse (open to short circuit) scan direction for each studied device. Due to the lack of hysteresis the two scans are indistinguishable. (b) *J*–*V* characteristics collected in the dark. Statistics on the (c) FF and (d) V_{oc} as a function of the top contact used.

leakage, but that is also not reflected in the measured V_{oc}, which was the highest across the entire device series.

While still a topic of debate, it is commonly accepted that a good energy level alignment is favourable for the carrier extraction (FF) and to limit recombination (increase V_{oc}) at the transport layer/perovskite interface.[7] In our case, however, the MAPI/ETL interface is unvaried, as in all device variations we have employed C_{60} in contact with the perovskite. One effect responsible for the difference in V_{oc} could be a variation of the diode built-in potential, which might help remove the majority carrier (electrons) from the MAPI/C_{60} interface. However, we did not observe appreciable differences in the built-in potential across the series of devices (Fig. S1†).

At open-circuit all photogenerated charge carriers recombine, and non-radiative recombination will reduce the quasi-Fermi-level splitting (QFLS), and hence limit the attainable photovoltage. As in perovskites recombination takes place from free charge carriers, the QFLS can be directly related to the perovskite photoluminescence quantum yield.[39] Hence, we performed photoluminescence (PL) measurements on full devices with the different top contacts. In order to compare the PL, we characterized the solar cells in an integrated sphere, illuminating the pixel with a 522 nm laser. We adjusted the laser power so that the J_{sc} of the cells matched the one obtained under simulated solar illumination, ensuring to have the same carrier concentration for all devices. All the PL spectra were taken with an integration time of 1 s.

The series of devices exhibited PL spectra with maxima centred at 1.58 eV (Fig. 3), independently on the top contact composition, but with different intensity. In general, V_{oc} fluctuations can be ascribed to a variation of the non-radiative recombination rates (change of the PL quantum yield) in the device. In particular, the more intense PL (and V_{oc}) observed for solar cells capped with Ba indicates that the electrode work function has indeed an important role on the charge carrier recombination dynamics of the perovskite film, even across the C_{60} film. On the other hand, devices with BCP and Liq showed the lowest PL intensity, while the combined BCP/Liq and BCP/Ba top contacts were found to lead to brighter PL. The solar cells with BCP and Liq interlayers were characterized by a high V_{oc}, although not accompanied by a proportionally intense PL signal, suggesting other competitive mechanisms determining the final photovoltage. It is important to note that the trends observed in the PL might be affected, at least partially, to transient phenomena which will be discussed below. The fact that both the electrode work function and type of interlayers can influence the MAPI PL, even when the adjacent C_{60} ETL is unvaried, reflects some of the unique properties of perovskites. It has been widely reported that the perovskite Fermi level can be drastically modulated by choosing the appropriate substrate.[31] In particular, p-type substrates (NiO_x, or MoO_3) impose a p-type character on the perovskite itself, and the same but opposite mechanism is true for n-type materials, such as metal oxides or low work function surfaces in general.[40,41] Within this perspective, we can reasonably envision that the Fermi level of the MAPI films is directly influenced also by the top surface (the top contacts studied here). The work function of these materials is, however, very difficult to probe as the interface is buried within the device.

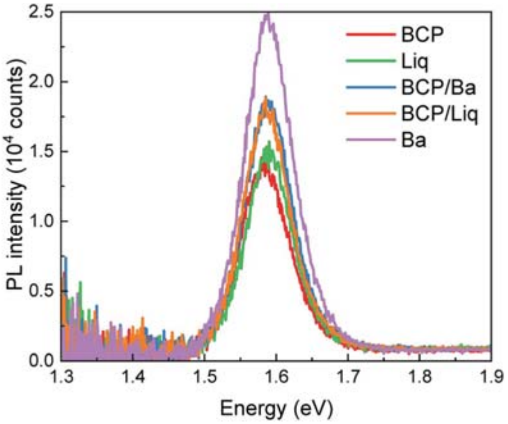

Fig. 3 Steady-state PL spectra of devices with different top contacts, excited with a 522 nm laser at the intensity equivalent to 1 sun illumination.

Table 1 Average photovoltaic parameters with standard deviation σ extracted from J–V curves for solar cells with different top contact

Top contact	FF (%)	V_{oc} (V) ± σ (mV)	J_{sc} (mA cm^{-2})	PCE (%)
BCP	77.8 ± 2.8	1.132 ± 3	20.5 ± 0.1	18.1 ± 0.2
Liq	77.6 ± 1.9	1.130 ± 4	20.4 ± 0.3	18.1 ± 0.3
BCP/Ba	67.1 ± 1.9	1.115 ± 2	20.7 ± 0.5	15.7 ± 0.1
BCP/Liq	78.3 ± 0.2	1.123 ± 6	20.6 ± 0.7	18.4 ± 0.2
Ba	71.8 ± 1.8	1.147 ± 7	20.7 ± 0.7	17.1 ± 0.6

We further investigated the characteristics of the series of solar cells by measuring their behaviour as a function of time, under continuous simulated solar illumination. The devices were encapsulated with UV-curable resin and a glass slide, and kept at 25 °C under a nitrogen flow (max relative humidity 10%), to minimize the effect of the environmental degradation. The maximum power point was continuously tracked and we also measured the device V_{oc} every 10 minutes. The evolution of the PCE over time for the series of devices are depicted in Fig. 4a. We can distinguish three types of behaviour for the device series. The solar cells employing Ba as the electrode (either alone or in combination with BCP) showed an initial fast rise in efficiency (to about 19%) followed by a relative fast decay of the device performance. After 2 days of continuous operation, the PCE for both devices was found to be already below 16%. This is expected as Ba is extremely reactive, and its implementation requires very rigorous encapsulation to ensure the absence of oxygen and/or moisture. On the contrary, the devices employing BCP and BCP/Liq in combination with the Ag electrode were found to be much more stable, and with rather similar decay profile. After 2 weeks of continuous operation, the device with BCP/Liq top contact still delivered a PCE of 15.5%, while the

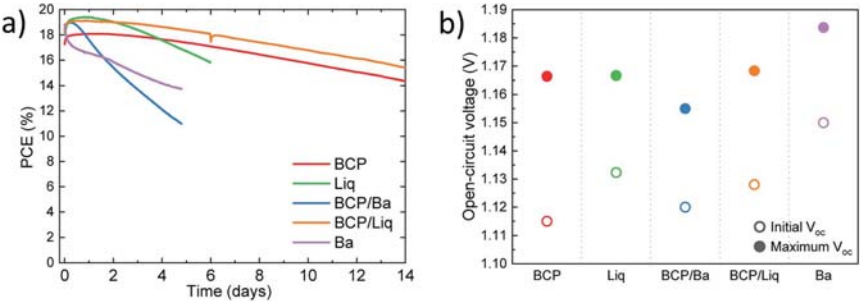

Fig. 4 (a) Evolution of the PCE of devices with different top contacts under continuous simulated solar illumination. (b) Open-circuit voltage for the same devices measured as-fabricated (empty symbols) and maximum V_{oc} recorded during maximum power point tracking (full symbols).

reference cell with only BCP showed an efficiency of 14.5%. Also in this set of devices we noted an initial rise of PCE to about 18% and 19% for cells with BCP and BCP/Liq top contacts, respectively.

The solar cell employing the thin Liq interlayer in between C_{60} and Ag showed a different behaviour, with an initial notable increase of the efficiency (up to 19.5% after 1 day) followed by a monotonic decay of the PCE, reaching about 16% after 6 days of operation. Apart from the perovskite intrinsic instability, the main processes driving the degradation of perovskite solar cells are the diffusion of halides to the electrode,[42] as well as the opposite migration of metal atoms from the electrode to the perovskite film.[43] With this in mind, we can reasonably ascribe the short lifetime observed for the cells with only 2 nm thick layers of Liq in between the C_{60} and Ag, to the faster interdiffusion of species between the MAPI film and the electrode. When BCP is used, it can alleviate this effect just because of the additional barrier it introduces, but likely also thanks to the ability of BCP to coordinate Ag atoms, as discussed above, which might slow down the metal diffusion. An interesting feature of the measurements under continuous illumination is the initial performance increase observed for the solar cells, independently on the top-contact used (although Ba was found to speed up the device degradation, as compared to the other interlayers). In particular, the open-circuit voltage was found to increase in all cases of about 40 to 50 mV, as illustrated in Fig. 4b. Considering that the variations are similar and virtually independent on the type of top-contact, their origin is most likely a consequence of a reduction of the non-radiative recombination within the MAPI film. A similar behaviour was previously observed in efficient vacuum-deposited n–i–p perovskite solar cells.[15] It has been widely reported that, under continuous illumination, the density of shallow traps can be reduced, leading to a decrease of the non-radiative recombination rate.[44,45] Interestingly, here we observed maximum V_{oc} close to 1.16 V for solar cells with BCP, Liq or their combinations, and up to 1.185 V for devices employing Ba as the electrode. Although in the latter case the stability was found to be very limited, these voltage values are among the highest reported for vacuum-processed MAPI solar cells.[15,46–48]

3 Conclusion

In summary, we have studied the influence of different interlayers, electrodes, and their combinations on the performance and especially the photovoltage of vacuum-processed perovskite solar cells. Organic semiconductors traditionally used in solar cells (BCP) and OLEDs (Liq) can lead to devices with high rectification, fill factor, and photovoltage. Furthermore, we have observed that the use of low work function metals, such as Ba, can be beneficial for the reduction of non-radiative recombination, although at the expenses of the device stability. Long-term device stability was observed only in the presence of BCP, with or without the Liq buffer layer. Future studies will address this aspect, trying to introduce low work function surfaces without undermining the device operation under continuous illumination.

4 Experimental section

4.1 Thin film and device preparation

To prepare the devices, the layers were deposited on ITO-coated glass substrates. The substrates were cleaned using soap, water, and subsequently isopropanol in an ultrasonic bath, followed by a UV-ozone treatment. The substrates were transferred into a nitrogen-filled glovebox (H_2O and $O_2 < 0.1$ ppm) equipped with a vacuum chamber with pressure lower than 10^{-6} mbar. MoO_3 and TaTm layers were deposited at rates of 0.1 and 0.4 Å s^{-1}, respectively. The MAPI films were deposited by co-evaporation of MAI and PbI_2 precursors simultaneously at the rates of 1.0 and 0.6 Å s^{-1}, respectively. The rates of the co-evaporation and the thickness of each layer were controlled by using three quartz crystal microbalance sensors. After deposition of the perovskite film, C_{60} was evaporated at a rate of 0.4 Å s^{-1} with the source temperature at 380 °C, and subsequently a thin layer (8 nm) of BCP was sublimed at a rate of 0.3 Å s^{-1} with a source temperature of 150 °C. Liq (2 nm) was deposited at a rate of 0.1 Å s^{-1}. Ba (5 nm) and Ag (100 nm) were evaporated in another vacuum chamber using molybdenum boats as sources by applying a current of 1 A and 3–4 A, respectively.

4.2 Device characterization

The *J–V* curves for the solar cells were recorded using a Keithley 2612A SourceMeter in a −0.2 and 1.2 V voltage range, with 0.01 V steps and integrating the signal for 20 ms after a 10 ms delay, corresponding to a speed of about 0.3 V s^{-1}. The devices were illuminated under a Wavelabs Sinus 70 LED solar simulator. The light intensity was calibrated before every measurement using a calibrated Si reference diode. Solar cell stability measurements (photovoltaic parameters *versus* time) were recorded using a maximum power point tracker system, with a white LED light source under 1 sun equivalent, developed by candlelight. During the stability measurements, the encapsulated devices were exposed to a flow of N_2 gas; temperature was stabilized at 300 K during the entire measurement using a water-circulating cooling system controlled by a Peltier element; *J–V* curve measurements were performed every 10 min.

4.3 Photoluminescence measurements

The photoluminescence of the full devices was measured with an Avantes AvaSphere-50-REFL integrating sphere connected to a 600 nm long-pass filter and an Avantes Avaspec2048 spectrometer. The devices were illuminated with a diode laser of integrated optics, emitting at 522 nm. The laser power was adjusted so that the short-circuit current *via* laser illumination matched the short-circuit current obtained from the measurement with the solar simulator. All the spectra were taken with an integration time of 1 s.

Conflicts of interest

There are no conflicts to declare.

Acknowledgements

The research leading to these results has received funding from the European Union Programme for Research and Innovation Horizon 2020 (2014–2020) under grant agreement No. 763977 of the PerTPV project, grant agreement No. 83441 of the ERC grant HELD, and from the Spanish Ministry of Economy and Competitiveness (MINECO) *via* the Unidad de Excelencia María de Maeztu MDM-2015-0538, MAT2017-88821-R, RTI2018-095362-A-I00, PCIN-2015-255, PCIN-2017-014, and the Generalitat Valenciana (Prometeo/2016/135). The project that gave rise to these results received the support of a fellowship from "la Caixa" Foundation (ID 100010434). The fellowship code is LCF/BQ/DI19/11730020. M. S. acknowledges the MINECO for his RyC contract.

References

1 A. K. Jena, A. Kulkarni and T. Miyasaka, *Chem. Rev.*, 2019, **119**, 3036–3103.
2 T. M. Brenner, D. A. Egger, L. Kronik, G. Hodes and D. Cahen, *Nat. Rev. Mater.*, 2016, **1**, 15007.
3 W. A. Dunlap-Shohl, Y. Zhou, N. P. Padture and D. B. Mitzi, *Chem. Rev.*, 2019, **119**, 3193–3295.
4 Z. Li, T. R. Klein, D. H. Kim, M. Yang, J. J. Berry, M. F. A. M. van Hest and K. Zhu, *Nat. Rev. Mater.*, 2018, **3**, 18017.
5 J. Ávila, C. Momblona, P. P. Boix, M. Sessolo and H. J. Bolink, *Joule*, 2017, **1**, 431–442.
6 H. D. Pham, L. Xianqiang, W. Li, S. Manzhos, A. K. K. Kyaw and P. Sonar, *Energy Environ. Sci.*, 2019, **12**, 1177–1209.
7 C. M. Wolff, P. Caprioglio, M. Stolterfoht and D. Neher, *Adv. Mater.*, 2019, 1902762.
8 S. S. Shin, S. J. Lee and S. Il Seok, *Adv. Funct. Mater.*, 2019, 1900455.
9 E. Castro, J. Murillo, O. Fernandez-Delgado and L. Echegoyen, *J. Mater. Chem. C*, 2018, **6**, 2635–2651.
10 Y. Shao, Z. Xiao, C. Bi, Y. Yuan and J. Huang, *Nat. Commun.*, 2014, **5**, 5784.
11 S.-Y. Hsiao, H.-L. Lin, W.-H. Lee, W.-L. Tsai, K.-M. Chiang, W.-Y. Liao, C.-Z. Ren-Wu, C.-Y. Chen and H.-W. Lin, *Adv. Mater.*, 2016, **28**, 7013–7019.
12 L. Gil-Escrig, C. Momblona, M. Sessolo and H. J. Bolink, *J. Mater. Chem. A*, 2016, **4**, 3667–3672.
13 S. C. Veenstra, A. Heeres, G. Hadziioannou, G. A. Sawatzky and H. T. Jonkman, *Appl. Phys. A: Mater. Sci. Process.*, 2002, **75**, 661–666.
14 O. Malinkiewicz, A. Yella, Y. H. Lee, G. M. Espallargas, M. Graetzel, M. K. Nazeeruddin and H. J. Bolink, *Nat. Photonics*, 2014, **8**, 128–132.
15 C. Momblona, L. Gil-Escrig, E. Bandiello, E. M. Hutter, M. Sessolo, K. Lederer, J. Blochwitz-Nimoth and H. J. Bolink, *Energy Environ. Sci.*, 2016, **9**, 3456–3463.
16 L. E. Polander, P. Pahner, M. Schwarze, M. Saalfrank, C. Koerner and K. Leo, *APL Mater.*, 2014, **2**, 081503.
17 T. H. Schloemer, J. A. Christians, J. M. Luther and A. Sellinger, *Chem. Sci.*, 2019, **10**, 1904–1935.
18 W.-H. Lee, C.-Y. Chen, C.-S. Li, S.-Y. Hsiao, W.-L. Tsai, M.-J. Huang, C.-H. Cheng, C.-I. Wu and H.-W. Lin, *Nano Energy*, 2017, **38**, 66–71.
19 K. Wang, M. Neophytou, E. Aydin, M. Wang, T. Laurent, G. T. Harrison, J. Liu, W. Liu, M. De Bastiani, J. I. Khan, T. D. Anthopoulos, F. Laquai and S. De Wolf, *Adv. Mater. Interfaces*, 2019, **6**, 1900434.
20 X. Liu, H. Yu, L. Yan, Q. Dong, Q. Wan, Y. Zhou, B. Song and Y. Li, *ACS Appl. Mater. Interfaces*, 2015, **7**, 6230–6237.
21 F. Fu, T. Feurer, T. P. Weiss, S. Pisoni, E. Avancini, C. Andres, S. Buecheler and A. N. Tiwari, *Nat. Energy*, 2017, **2**, 16190.
22 K. A. Bush, A. F. Palmstrom, Z. J. Yu, M. Boccard, R. Cheacharoen, J. P. Mailoa, D. P. McMeekin, R. L. Z. Hoye, C. D. Bailie, T. Leijtens, I. M. Peters, M. C. Minichetti, N. Rolston, R. Prasanna, S. Sofia, D. Harwood, W. Ma, F. Moghadam, H. J. Snaith, T. Buonassisi, Z. C. Holman, S. F. Bent and M. D. McGehee, *Nat. Energy*, 2017, **2**, 17009.
23 D. F. O'Brien, M. A. Baldo, M. E. Thompson and S. R. Forrest, *Appl. Phys. Lett.*, 1999, **74**, 442–444.
24 H. Gommans, B. Verreet, B. P. Rand, R. Muller, J. Poortmans, P. Heremans and J. Genoe, *Adv. Funct. Mater.*, 2008, **18**, 3686–3691.
25 H. Yoshida, *J. Phys. Chem. C*, 2015, **119**, 24459–24464.

26 J. Avila, L. Gil-Escrig, P. P. Boix, M. Sessolo, S. Albrecht and H. J. Bolink, *Sustainable Energy Fuels*, 2018, **2**, 2429–2434.
27 C. Chen, S. Zhang, S. Wu, W. Zhang, H. Zhu, Z. Xiong, Y. Zhang and W. Chen, *RSC Adv.*, 2017, **7**, 35819–35826.
28 M. Vogel, S. Doka, C. Breyer, M. C. Lux-Steiner and K. Fostiropoulos, *Appl. Phys. Lett.*, 2006, **89**, 163501.
29 F. Jafari, B. R. Patil, F. Mohtaram, A. L. F. Cauduro, H.-G. Rubahn, A. Behjat and M. Madsen, *Sci. Rep.*, 2019, **9**, 10422.
30 J. M. Ball and A. Petrozza, *Nat. Energy*, 2016, **1**, 16149.
31 P. Schulz, D. Cahen and A. Kahn, *Chem. Rev.*, 2019, **119**, 3349–3417.
32 J. Lee, H.-F. Chen, T. Batagoda, C. Coburn, P. I. Djurovich, M. E. Thompson and S. R. Forrest, *Nat. Mater.*, 2016, **15**, 92–98.
33 C. Schmitz, H.-W. Schmidt and M. Thelakkat, *Chem. Mater.*, 2000, **12**, 3012–3019.
34 T. Chiba, Y.-J. Pu, M. Hirasawa, A. Masuhara, H. Sasabe and J. Kido, *ACS Appl. Mater. Interfaces*, 2012, **4**, 6104–6108.
35 H. Kaji, H. Suzuki, T. Fukushima, K. Shizu, K. Suzuki, S. Kubo, T. Komino, H. Oiwa, F. Suzuki, A. Wakamiya, Y. Murata and C. Adachi, *Nat. Commun.*, 2015, **6**, 1–8.
36 J. Kido and T. Matsumoto, *Appl. Phys. Lett.*, 1998, **73**, 2866–2868.
37 F. A. Angel, R. Gao, J. U. Wallace and C. W. Tang, *Org. Electron.*, 2018, **59**, 220–223.
38 D. Kiermasch, L. Gil-Escrig, H. J. Bolink and K. Tvingstedt, *Joule*, 2019, **3**, 16–26.
39 R. T. Ross, *J. Chem. Phys.*, 1967, **46**, 4590–4593.
40 P. Schulz, L. L. Whittaker-Brooks, B. A. MacLeod, D. C. Olson, Y.-L. Loo and A. Kahn, *Adv. Mater. Interfaces*, 2015, **2**, 1400532.
41 S. Olthof and K. Meerholz, *Sci. Rep.*, 2017, **7**, 40267.
42 C. C. Boyd, R. Cheacharoen, T. Leijtens and M. D. McGehee, *Chem. Rev.*, 2019, **119**, 3418–3451.
43 C. C. Boyd, R. Cheacharoen, K. A. Bush, R. Prasanna, T. Leijtens and M. D. McGehee, *ACS Energy Lett.*, 2018, **3**, 1772–1778.
44 S. Chen, X. Wen, S. Huang, F. Huang, Y.-B. Cheng, M. Green and A. Ho-Baillie, *Sol. RRL*, 2017, **1**, 1600001.
45 R. Brenes, D. Guo, A. Osherov, N. K. Noel, C. Eames, E. M. Hutter, S. K. Pathak, F. Niroui, R. H. Friend, M. S. Islam, H. J. Snaith, V. Bulović, T. J. Savenije and S. D. Stranks, *Joule*, 2017, **1**, 155–167.
46 D. Pérez-del-Rey, P. P. Boix, M. Sessolo, A. Hadipour and H. J. Bolink, *J. Phys. Chem. Lett.*, 2018, **9**, 1041–1046.
47 V. S. Chirvony, K. S. Sekerbayev, D. Pérez-del-Rey, J. P. Martínez-Pastor, F. Palazon, P. P. Boix, T. I. Taurbayev, M. Sessolo and H. J. Bolink, *J. Phys. Chem. Lett.*, 2019, **10**, 5167–5172.
48 A. Al-Ashouri, A. Magomedov, M. Roß, M. Jošt, M. Talaikis, G. Chistiakova, T. Bertram, J. A. Márquez, E. Köhnen, E. Kasparavičius, S. Levcenco, L. Gil-Escrig, C. J. Hages, R. Schlatmann, B. Rech, T. Malinauskas, T. Unold, C. A. Kaufmann, L. Korte, G. Niaura, V. Getautis and S. Albrecht, *Energy Environ. Sci.*, 2019, **12**, 3356–3369.

SUPPLEMENTARY INFORMATION

High voltage vacuum-processed perovskite solar cells with organic semiconducting interlayers

Azin Babaei, Chris Dreessen, Michele Sessolo* and Henk J. Bolink

Instituto de Ciencia Molecular, Universidad de Valencia, C/ Beltrán 2, Paterna, 46980, Spain. E-mail: michele.sessolo@uv.es

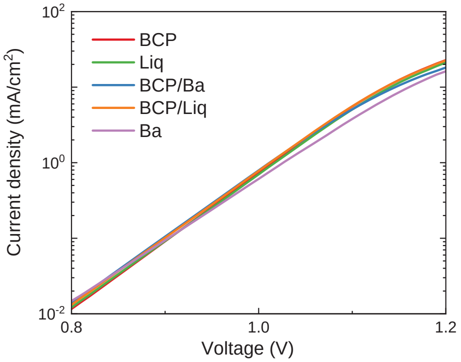

Figure S1. IV curves in the dark for solar cells with different top contacts. The region highlights the transition between the diffusion and drift regimes. No substantial differences in built-in potential can be found.

Top contact	FF (%)	V_{oc} (V)	J_{sc} (mA cm^{-2})	PCE (%)
BCP	79.7	1.135	21.8	18.9
Liq	79.2	1.136	21.8	19.1
BCP/Ba	75.3	1.116	21.3	17.8
BCP/Liq	80.1	1.130	21.7	18.8
Ba	79.7	1.155	21.8	18.9

Table S1 Maximum photovoltaic parameters extracted from J-V curves for different top contacts.

Chapter 5.

Efficient vacuum deposited p-i-n perovskite solar cells by front contact optimization

5. Efficient vacuum deposited p-i-n perovskite solar cells by front contact optimization

5.1. Introduction

As described in chapter 1, there are two main solar cell structures, termed n-i-p and p-i-n. In both structures, the perovskite absorber layer is sandwiched in between the charge selective layers, HTL and ETL. Each transport layer is responsible for transporting only a specific type of carrier by blocking the opposite one. To develop highly efficient solar cells, it is crucial to understand and optimize the properties of these charge selective layers. In p-i-n solar cells, the HTL plays a significant role in the overall device functioning, as the carrier concentration at the front HTL/perovskite contact is higher. As mentioned before, a suitable HTL should confine electrons and efficiently extract holes, avoiding non-recombination losses at the HTL/perovskite interface. To ensure such selectivity, the HOMO of the HTM should be aligned with the valence band maximum of the perovskite (-5.4 eV for $MAPbI_3$), while its electron affinity should be low enough to efficiently block electrons within the perovskite. For this reason, wide bandgap semiconductors are often used as HTLs. Furthermore, the choice of the HTL has a substantial effect on the device stability and lifetime.[124] Apart from the energy level alignment with the perovskite, an ohmic contact between the HTL and the charge collecting electrode is essential to ensure efficient charge collection. A transparent electrode which is widely adopted in p-i-n solar cells is ITO, with a work function of approximately 4.7 eV. As the requirement for a HTL is to match the perovskite valence band maximum, the energy difference between ITO and the perovskite leads to a barrier for the hole injection/extraction of up to 0.7 eV. One common approach to reduce this barrier is to use a high work function interlayer between the electrode and the HTL, most commonly a metal oxide such as NiO_x, V_2O_5 or MoO_3.[101,108,125,126] MoO_3 is a promising and versatile material due to the ease of processing, non-toxicity, ambient stability, and very high work function.[127] MoO_3 was initially used in OLEDs as a hole injection layer and later in organic solar cells as an anode buffer layer.[66,101,128,129] MoO_3 have been also used in perovskite solar cells as an interfacial layer between the anode and the hole transport layer to improve the hole transportation.[130,131] In p-i-n solar cells, the use of a hole injection/extraction interlayer results in a reduction of the series resistance, leading to high FF, J_{SC} and enhanced PCE. The thin-film processing procedure has an important effect on the electronic properties of MoO_3. MoO_3 can be easily processed both from solution and vacuum deposition techniques.[125,132,133] Thermal vacuum deposition provides a precise control over the film thickness and is suitable for fabrication of multilayer devices without complications related with the use of solvents (redissolution or intermixing of underlying films). The quality and properties of vacuum-deposited films varies with the chamber pressure, the source temperature and the deposition rate. Post-deposition treatments, such as annealing temperatures can also affect the deposited films and subsequently the solar cell performance.[134,135]

In this chapter we study the effect of post-deposition treatments of MoO_3 films at the interface with HTLs in perovskite solar cells. The HTL which was used is TaTm and the whole stack has the following configuration: ITO/MoO_3/TaTm/$MAPbI_3$/C_{60}/BCP/Ag.

We investigated and compared the effect of annealing MoO_3 prior to the deposition of TaTm and annealing the MoO_3/TaTm together. We examined a broad range of temperatures from 60 to 200 °C.

5.2. Results and discussion

Figure 22 represents the JV curves under simulated solar illumination for the two series of solar cells with the p-contact annealed at temperatures varied from 60 °C to 200 °C. In almost all the temperatures tested, the solar cells in which the annealing of the p-contact was performed after the deposition of TaTm (blue curves) showed higher FF compared to devices with annealing performed before the deposition of TaTm (orange curves). This means that charge carrier extraction/injection are enhanced when the annealing is carried out on the MoO_3/TaTm bilayer.

To get a more complete picture of the device characteristics, the PV performance parameters extracted from the JV curves are shown in figure 23 as a function of the annealing temperature. All devices exhibited a similar J_{SC} of about 19–20 mA cm^{-2}. Slight fluctuations in the values recorded for the J_{SC} originated from batch to batch variations in the $MAPbI_3$ deposition process.

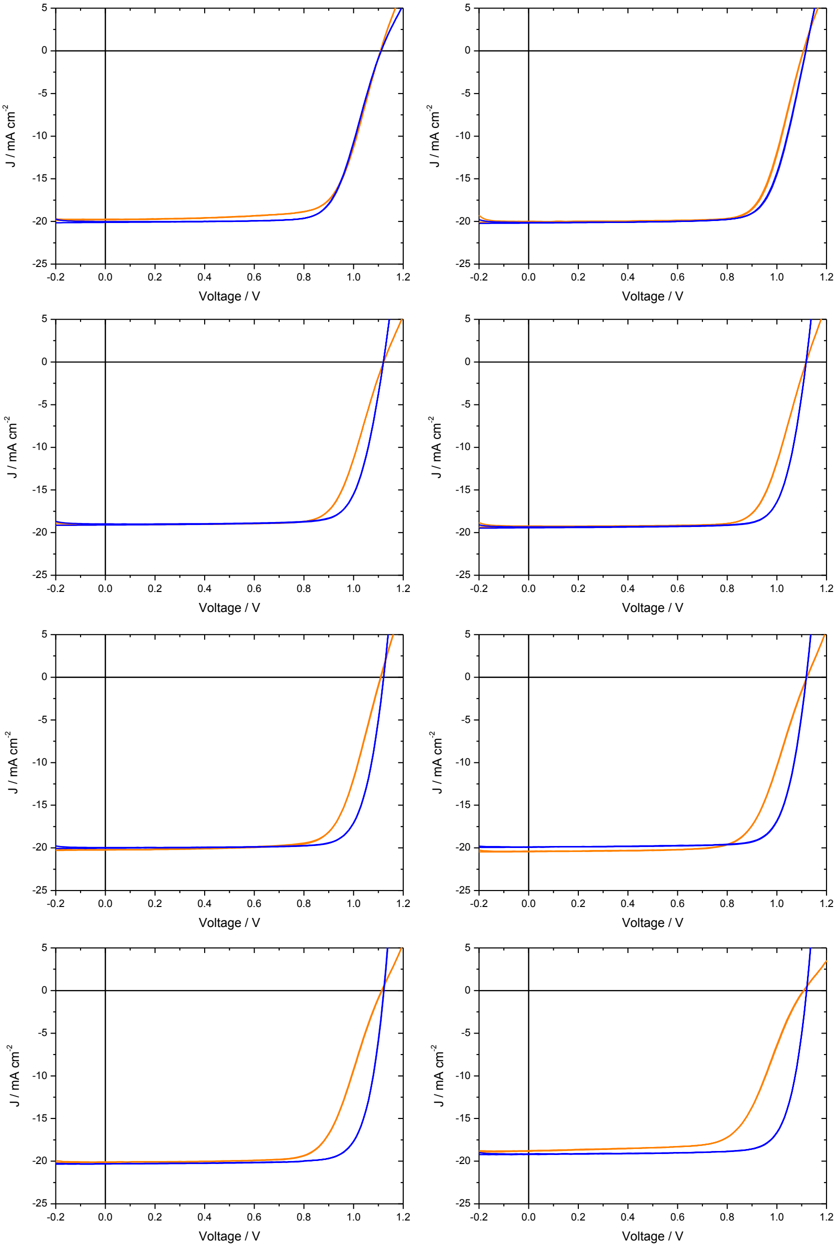

Figure 22. JV curves under simulated solar illumination for two series of solar cells, with annealing of the p-contacts performed before (orange line) or after (blue line) the deposition of TaTm.

Figure 23.B shows an increase in the V_{OC} when increasing the temperature from 60 °C to 100 °C for both series of devices. Interestingly, for the cells with annealed MoO_3/TaTm bilayers, the V_{OC} was found to be high and stable (>1.12 V) even for annealing temperatures above 100 °C.

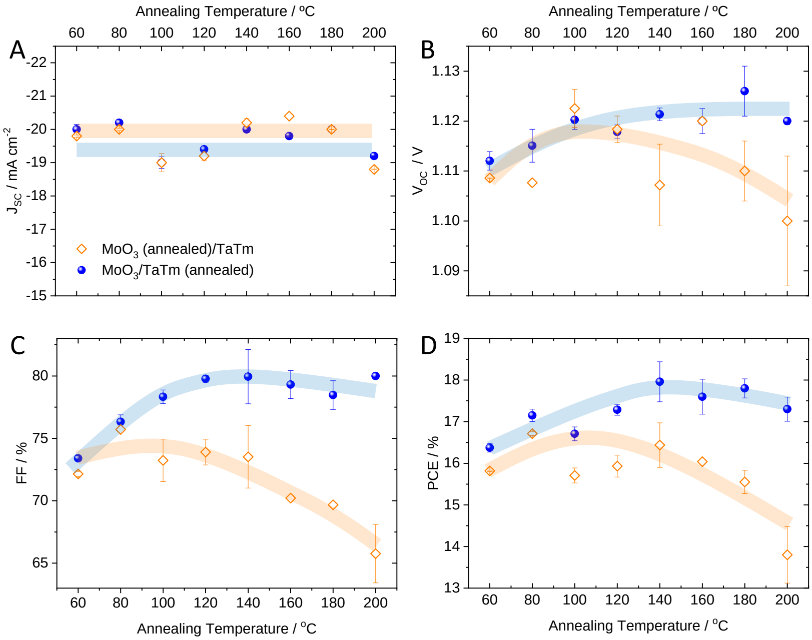

Figure 23. Photovoltaic parameters extracted form JV curves under simulated solar illumination, for solar cells with the MoO_3/TaTm contacts annealed at different temperatures. The blue symbols indicate that the annealing was carried out on the MoO_3/TaTm bilayer, while orange symbols correspond to devices where the annealing was carried out on the MoO_3 prior to depositing TaTm. Lines are a guide to the eye for the reader.

On the contrary, the voltage was lower and progressively decreasing for the cells with only annealed the MoO_3 layer (<1.11 V). For the cells with the annealed MoO_3/TaTm bilayer, the FF increases from 73% (at 60 °C) to about 80% (in the 120 – 200 °C range), while for the devices with annealed MoO_3 prior to the deposition of TaTm, the FF shows a constant value of about 73% up to 140 °C, and afterwards a continuous decrease down to 65% (figure 23.C). The evolution of the PCE vs. annealing temperature (figure 23.D) follows rather similar trends as the FF for both device series.

Illuminated and dark JV curves of the devices annealed at optimal temperature (140 °C) are shown in figure 24. A high V_{OC} (1.105 V) and J_{SC} (20 mA cm^{-2}), but reduced FF (73%) were observed for the device with the p-contact annealed before the deposition of TaTm layer. The low FF is caused by the reduced slope of the JV curve after the maximum power point (> 0.8 V), which is an indication of the presence of high series resistance in these cells, which results in hindered charge extraction/injection. Hindered charge extraction may lead to charge accumulation at the interface and subsequently increases the probability of non-radiative recombination. On the contrary, solar cells with the p-contact annealed after the deposition of TaTm led to devices with high FF (80%), indicating that the charge carrier extraction is improved. This can be clearly seen form the dark JV curves, where the slope of the diffusion region (0.5 - 1 V) as well as the current density recorded at 1.2 V outperform those of the other type of devices.

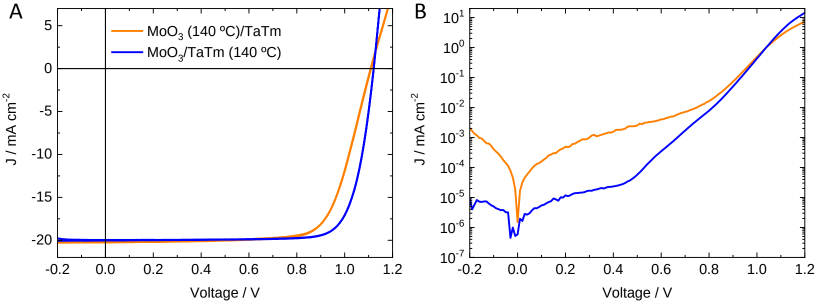

Figure 24. (A) Illuminated and (B) dark JV curves (forward and backward) of ITO/MoO_3/TaTm/$MAPbI_3$/C_{60}/BCP/Ag solar cells for which the annealing of the MoO_3 layer was performed at 140 °C before (orange line) or after (blue line) the deposition of the TaTm layer.

The performance of the solar cells with the optimum annealing temperature (140 °C) were also investigated as a function of the incident light intensity, as summarized in figure 25. Diode ideality factors (IF) of 1.9 and 1.4 have been calculated for the low (0.1 – 10 mW cm^{-2}) and high (10 – 100 mW cm^{-2}) intensity regimes, respectively, with no significant difference for the two sets of devices (figure 25.A-B). However, the V_{OC} was found to be systematically larger when annealing the TaTm layer on top of the MoO_3 buffer layer, indicating that non-radiative recombination is reduced with this p-contact.

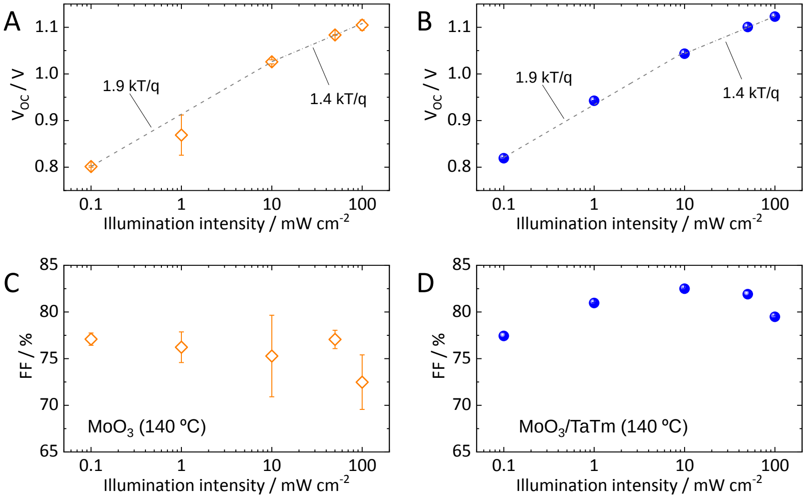

Figure 25. Light intensity dependent characterization of perovskite solar cells with p-contacts annealed at 140 °C. The intensity dependent open-circuit voltage for cells with annealing on (A) bare MoO_3 and on (B) the MoO_3/TaTm bilayer has been fitted to extract the ideality factor, reported in the graphs. The dependence of the FF for cells employing annealed (C) MoO_3 or (D) MoO_3/TaTm bilayers is also reported.

The calculated IF = 1.9 at low carrier concentration suggests a dominant trap-assisted recombination in the bulk of perovskite, while at higher light intensities the IF ≈ 1.4 is likely reduced due to surface recombination at the front contact.[136]

Figure 25. C-D shows the trend of the FF with increasing light intensity. For devices with MoO_3 annealed before coating the TaTm layer, no clear trend can be seen (figure 25.C), which can be an indication of the presence of an extraction barrier at the Moo_3/TaTm interface, which does not lead to recombination (as the intensity dependent V_{OC} is similar to the other devices). The existence of the potential barrier at the MoO_3/TaTm interface

hinders efficient charge collection at the p-contact, reducing the FF (< 77%) of the solar cells. This barrier would also justify the series resistance observed for these diodes (figure 24. B). For the higher efficiency devices with the annealed MoO_3/TaTm bilayer (figure 3.D), the decreased FF at low light intensity (low carrier concentration) indicates that traps dominate this regime, in agreement with the trend observed for the photovoltage (figure 23.B).

Figure 26 shows Kelvin probe measurements performed (in air) on the surface of MoO_3 as a function of the annealing temperature. It shows a WF of 5.05 eV for the sample annealed at 60 °C, while for higher temperatures, the MoO_3 WF was found to decrease by approximately 0.2 eV. The WF reduction is in agreement with the trend of FF observed in figure 23.C for cells in which annealing was carried out on the MoO_3 film before deposition of TaTm. This suggests that the WF of the electrode might be responsible for the extraction barrier and recombination at the front contact. Greiner et al. reported that increasing oxygen vacancies results in lowering the work function (WF) of MoO_3.[137,138]

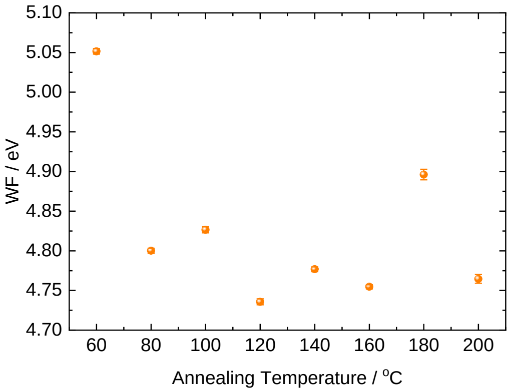

Figure 26. Effect of annealing temperature on the WF of the surface of MoO_3 thin films deposited on ITO-coated glass slides.

As mentioned in chapter 2, Kelvin probe measurement is a surface sensitive technique; hence we could not extract meaningful information for the MoO_3 films coated with TaTm. In this case, the loss of oxygen upon annealing might be hindered by the presence of a physical barrier of TaTm on top of MoO_3 which results in better ohmic contact within the MoO_3/TaTm interface.[101]

5.3. Conclusion

We observed that the PCE of p-i-n PCSs can be substantially improved by post-deposition annealing at the interface of MoO_3/TaTm HTL. Large improvements in FF (>80%) and PCE (18%) were achieved when the TaTm layer was deposited and annealed together with the MoO_3 layer, with optimal results obtained for an annealing temperature of 140 ^{o}C. The improved performance for solar cells with annealed ITO/MoO_3 bilayers is likely related with an intimate interaction between the two materials, which minimizes the energy barrier for hole transfer at their interface.

frontiers
in Chemistry

ORIGINAL RESEARCH
published: 17 January 2020
doi: 10.3389/fchem.2019.00936

Efficient Vacuum Deposited P-I-N Perovskite Solar Cells by Front Contact Optimization

Azin Babaei[1], Kassio P. S. Zanoni[1], Lidón Gil-Escrig[2], Daniel Pérez-del-Rey[1], Pablo P. Boix[1], Michele Sessolo[1]* and Henk J. Bolink[1]*

[1] Instituto de Ciencia Molecular, Universidad de Valencia, Paterna, Spain, [2] Helmholtz-Zentrum Berlin für Materialien und Energie GmbH, Berlin, Germany

Hole transport layers (HTLs) are of fundamental importance in perovskite solar cells (PSCs), as they must ensure an efficient and selective hole extraction, and ohmic charge transfer to the corresponding electrodes. In p-i-n solar cells, the ITO/HTL is usually not ohmic, and an additional interlayer such as MoO_3 is usually placed in between the two materials by vacuum sublimation. In this work, we evaluated the properties of the MoO_3/TaTm (TaTm is the HTL N4,N4,N4″,N4″-tetra([1,1′-biphenyl]-4-yl)-[1,1′:4′,1″-terphenyl]-4,4″-diamine) hole extraction interface by selectively annealing either MoO_3 (prior to the deposition of TaTm) or the bilayer MoO_3/TaTm (without pre-treatment on the MoO_3), at temperature ranging from 60 to 200°C. We then used these p-contacts for the fabrication of a large batch of fully vacuum deposited PSCs, using methylammonium lead iodide as the active layer. We show that annealing the MoO_3/TaTm bilayers at high temperature is crucial to obtain high rectification with low non-radiative recombination, due to an increase of the electrode work function and the formation of an ohmic interface with TaTm.

Keywords: perovskite solar cell, molybdenum oxide, vacuum-deposition, processing, hole transport layer

Edited by:
Silvia Colella,
University of Salento, Italy

Reviewed by:
Iván Mora-Seró,
University of Jaume I, Spain
Vincenzo Pecunia,
Soochow University, China

***Correspondence:**
Kassio P. S. Zanoni
kassio.zanoni@uv.es
Michele Sessolo
michele.sessolo@uv.es

Specialty section:
This article was submitted to Physical Chemistry and Chemical Physics, a section of the journal Frontiers in Chemistry

Received: *11 November 2019*
Accepted: *23 December 2019*
Published: *17 January 2020*

Citation:
Babaei A, Zanoni KPS, Gil-Escrig L, Pérez-del-Rey D, Boix PP, Sessolo M and Bolink HJ (2020) Efficient Vacuum Deposited P-I-N Perovskite Solar Cells by Front Contact Optimization. Front. Chem. 7:936. doi: 10.3389/fchem.2019.00936

Perovskite solar cells (PSCs) are at the forefront of emerging photovoltaics materials, as demonstrated by the continuously rising power conversion efficiency (PCE) (Green et al., 2019). Achieving high conversion efficiencies requires placing the perovskite absorber in between selective charge transport layers that direct charge carriers to the appropriate electrodes for extraction (Pham et al., 2019; Shin et al., 2019). The choice of suitable charge selective materials depends on the type of device architecture used, the particular perovskite absorber, and on the thin-film processing technique. PSCs can be prepared in different architectures, depending on the polarity of the transparent electrode, normally a transparent conductive oxide (TCO) coated on a glass substrate. If the TCO front electrode is used as the p-contact, the structure is referred to as p-i-n, while if electrons are collected at the front contact, the solar cell is termed n-i-p. In p-i-n solar cells, the most common TCO is indium tin oxide (ITO), which is coated with a suitable hole transport layer (HTL) to selectively shuttle holes from the perovskite to the electrode. The hole transport material (HTM) should have a highest occupied molecular orbital (HOMO) or valence band close in energy to the perovskite valence band, as any mismatch would introduce losses in charge extraction or recombination (Schulz et al., 2015). Common molecular HTMs are arylamine derivatives (either polymers or isolated "small" molecules) and polythiophenes, due to their favorable hole mobility and suitable energy level alignment with most perovskite absorbers (Pham et al., 2019). While in some circumstances the direct ITO/HTL p-contact can lead to very efficient charge collection (Al-Ashouri et al., 2019; Liu et al., 2019), the interface is not ohmic, and an additional interlayer is usually placed in between the ITO and the HTL (Schloemer et al., 2019). Common interface materials are high work function molecules (Avila et al., 2018), doped organic semiconductors (Momblona et al., 2016; Schloemer et al., 2019), or metal oxides such as MoO_3, V_2O_5, and W_2O_3 (Shin et al., 2019). MoO_3 is widely adopted as it can be deposited in thin-films by simple thermal vacuum sublimation, resulting in quasi-ohmic interfaces (Schulz et al., 2016). The use of vacuum deposition for transport layers and in particular for the perovskite gives several advantages over solution techniques. The thickness of each layer can be finely controlled, the materials purity is enhanced, and, more importantly, vacuum deposition methods are intrinsically additive, meaning that multilayer devices can be prepared without issues such as intermixing or partial redissolution of materials which are common to solution processing (Ávila et al., 2017). Recently, we have demonstrated the first vacuum-deposited PSCs with metal oxides at both the electron and the hole transporting layers (ETL and HTL) (Pérez-del-Rey et al., 2019). Both the p-i-n or n-i-p structures used MoO_3 at the p-contact, in combination with N4,N4,N4″,N4″-tetra([1,1′-biphenyl]-4-yl)-[1,1′:4′,1″-terphenyl]-4,4″-diamine (TaTm, **Figure 1**) as the HTM. In this work, we study the MoO_3/TaTm interface and use post-deposition treatments in order to ensure an ohmic contact at the interface, demonstrating that a high work function MoO_3 is required to obtain high efficiency, vacuum deposited p-i-n PSCs.

For this study we used the following device configuration (**Figure 1**): ITO/MoO_3 (5 nm)/TaTm (10 nm)/MAPI (600 nm)/C_{60} (25 nm)/BCP (8 nm)/Ag (in which C_{60} is fullerene; BCP is bathocuproine and MAPI is methylammonium lead iodide). TaTm and C_{60} are intrinsic organic materials for charge selection, and MoO_3 and BCP are p- and n-contacts for efficient extraction of the photogenerated holes and electrons, respectively (Pérez-del-Rey et al., 2019; Zanoni et al., 2019). All the layers in the device, including the MAPI perovskite film, were deposited by vacuum-assisted thermal evaporation, as described in the experimental section in the **Supporting Information**. To ensure sufficient statistics, for each device configuration, at least two different substrates each containing four cells were evaluated, while for top performing configurations at least five different substrates with a total of 20 cells were characterized. Due to the limited number of substrates (5) that can be processed in the setup used for these experiments, samples were fabricated through several perovskite deposition runs. Hence, small batch-to-batch variations might also contribute to the deviations observed in the photovoltaic parameters. We evaluated the properties of the MoO_3/TaTm hole extraction interface by selectively annealing either MoO_3 (prior to the deposition of TaTm) or the bilayer MoO_3/TaTm (without pre-treatment on the MoO_3), at temperature ranging from 60 to 200°C in a nitrogen atmosphere for 10 min. We then used these p-contacts for the fabrication of solar cells as described above. The series of devices was initially characterized under simulated solar illumination by measuring the current density vs. voltage (J-V) curves and extracting the relevant PV performance parameters (**Figure 2**).

As depicted in **Figure 2A**, all devices exhibited similar short-circuit current densities (J_{SC}) in the 19–20 mA cm^{-2} range, with small fluctuations originated from common batch-to-batch variability in the MAPI perovskite film properties. A difference in the temperature dependence can be observed for the open-circuit voltage (V_{oc}, **Figure 2B**), but especially for the fill factor (FF, **Figure 2C**). For both device series, we noted an increase in the photovoltage from 60 to ∼100°C, after which the V_{oc} was found to be high and stable (>1.12 V) for the cells with annealed MoO_3/TaTm bilayer, or lower and progressively decreasing for the cells with annealed MoO_3 (until <1.11 V). The FF (**Figure 2C**) was found to steadily increase from 73% (at 60°C) to about 80% (in the 120–200°C range) for devices employing the annealed MoO_3/TaTm bilayer. An opposite behavior was

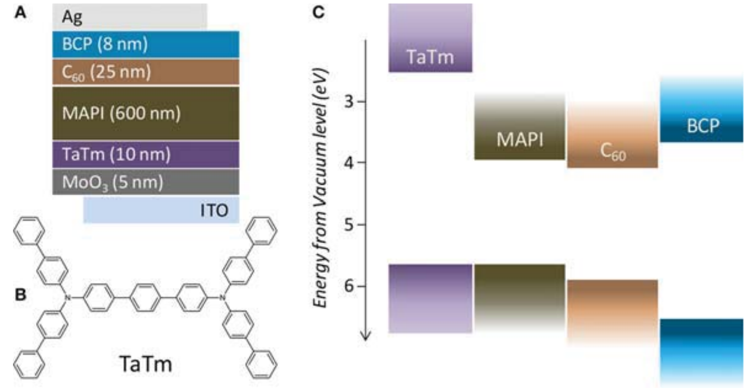

FIGURE 1 | (A) Schematics of the device architecture, **(B)** chemical structure of the hole transport layer TaTm and **(C)** flat band energy diagram with the semiconducting materials used in the solar cells.

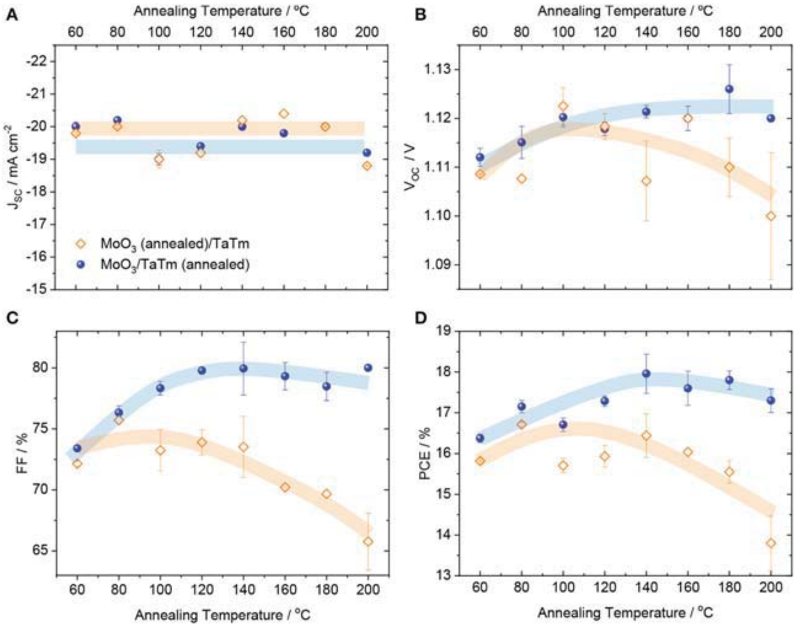

FIGURE 2 | Photovoltaic parameters—**(A)** J_{SC}, **(B)** V_{OC}, **(C)** FF and **(D)** PCE—extracted form J-V curves under simulated solar illumination, for MoO$_3$/TaTm contacts annealed at different temperatures. The blue symbols indicate that the annealing was carried out after deposition of the MoO$_3$/TaTm bilayer, while orange symbols correspond to devices where the annealing was carried out on the MoO$_3$ prior to depositing TaTm. Lines are a guide to the eye for the reader.

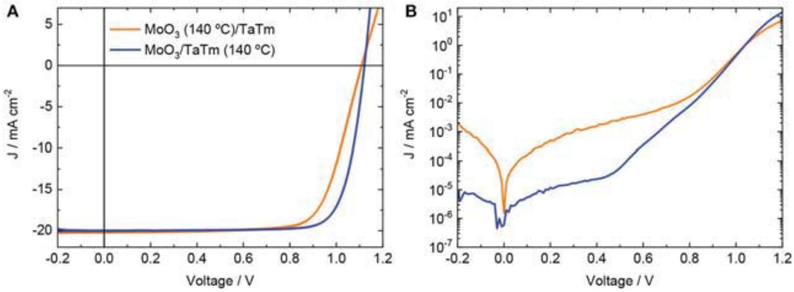

FIGURE 3 | J-V curves **(A)** under simulated solar illumination and **(B)** in the dark for solar cells with structure ITO/MoO$_3$/TaTm/MAPbI$_3$/C$_{60}$/BCP/Ag, with annealing of the p-contacts performed at 140°C before (orange line) or after (blue line) the deposition of TaTm.

observed when annealing the MoO$_3$ prior to the deposition of TaTm. In this case the FF is rather constant at 72–73% until 140°C, when it starts to progressively decrease reaching values of ∼65% at 200°C. The evolution of the V_{oc} and especially of the FF with the temperature determine the overall PCE. For solar cells with annealed MoO$_3$/TaTm bilayers, the PCE steadily increases from 60°C (16.5%), reaching a maximum of 18% at 140°C, and only slightly diminishing to still above 17% for higher temperatures. On the other hand, the PCE of devices where annealing is carried out on the bare MoO$_3$ peaks at 140°C (at 16.5%), but it is strongly limited at higher temperatures, with values below 14% for p-contact annealed at 200°C.

The representative J-V curves under simulated solar illumination for the two types of device with p-contact annealed at 140°C are reported in **Figure 3** (J-V curves for all the other investigated annealing temperatures are reported in **Figure S1**).

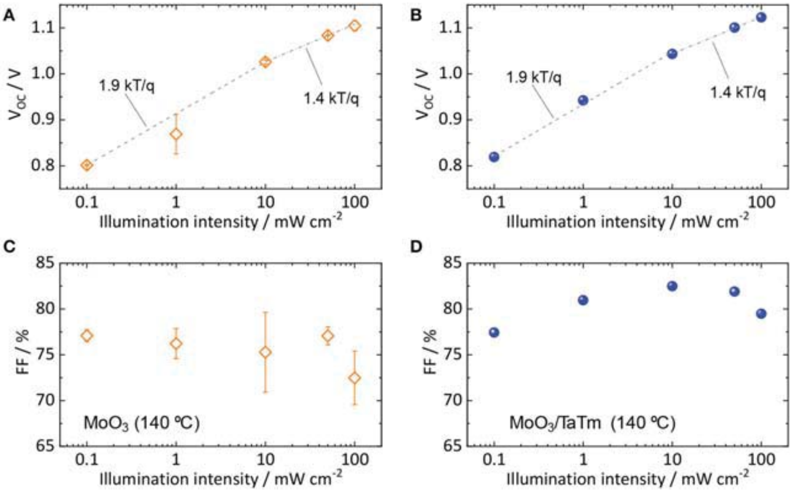

FIGURE 4 | Light intensity dependent characterization of the perovskite solar cells with p-contacts annealed at 140°C. The intensity dependent open-circuit voltage for cells with annealing on **(A)** the bare MoO_3 and on **(B)** the MoO_3/TaTm bilayer has been fitted to extract the ideality factor, reported in the graphs. The dependence of the FF for cells employing annealed **(C)** MoO_3 or **(D)** MoO_3/TaTm bilayers is also reported.

The device with a MoO_3 layer annealed before TaTm deposition exhibited fairly high V_{oc} of 1.105 V and J_{sc} of 20 mA cm^{-2}, but with a rather poor FF of 73%. This is caused by the reduced slope of the J-V curve after the maximum power point (>0.8 V), which reveals the presence of a high series resistance in these cells (hindered charge extraction/injection). The lower V_{oc} is likely related to the extraction issue, as charge accumulation at the interface can increase the probability of non-radiative recombination, as well as to the higher leakage current (J-V curves in dark, **Figure 3B**). On the contrary, having the TaTm top-layer deposited and annealed together with MoO_3 led to solar cells with high rectification (FF = 80%), meaning that charge carrier extraction and injection are enhanced. This can be clearly seen form the dark J-V curves, where the slope of the diffusion region (0.5–1 V) as well as the current density at 1.2 V outperform those of the other type of devices.

The same set of solar cells with the optimum annealing temperature (140°C) were also studied as function of the incident light intensity, as summarized in **Figure 4**. The V_{oc} dependence for both devices (**Figures 4A,B**) showed a higher slope at low light intensity, reduced when approaching 1 sun equivalent illumination (10–100 mW cm^{-2}). Fitting the logarithmical dependence of the V_{oc} with the light intensity resulted in diode ideality factors (IF) of 1.9 and 1.4 for the low and high intensity regime, respectively. This behavior can be rationalized on the basis of a dominant trap-assisted recombination (IF = 2) in the bulk of the perovskite at low carrier concentration, and the appearance of surface recombination at the front contact (lowering the IF) which saturates the V_{oc} at higher light intensity (Tress et al., 2018). The trend of intensity-dependent current density for the same devices (**Figure S2**) also suggest hindered charge extraction (increased recombination) at high light intensity, as the power factor α becomes < 1.

While no substantial differences could be discerned for the two set of devices, the V_{oc} was found to be systematically larger when annealing the TaTm on top of the MoO_3 buffer layer, indicating that non-radiative recombination is reduced with this p-contact.

The recombination processes and presence of traps can also be deduced from the trend of the FF with decreasing light-intensity. In a pure trap-assisted recombination regime, the FF decreases with decreasing light intensity as the trap density is constant while the carrier concentration diminishes. For free-carrier recombination, the FF would increase monotonically when decreasing the light intensity, as the recombination rate depends only on the charge densities (Sherkar et al., 2017). As can be seen from **Figure 4D** for the high efficiency device with annealed MoO_3/TaTm bilayer, free carrier recombination is present for light intensity above 10 mW cm^{-2}, while trap-assisted recombination dominates for low light intensities, in agreement with the trend of photovoltage (**Figure 4B**). On the other hand, the solar cells with the annealed MoO_3 did not show a clear trend in the intensity dependence of the FF, remaining rather low (<77%) at all charge carrier concentration. This might indicate the presence of an extraction barrier at the MoO_3/TaTm interface, which however does not lead to substantial recombination (as the intensity dependent V_{oc} is similar to the other devices). When the majority carriers (holes) are transferred from the perovskite into the TaTm, they can

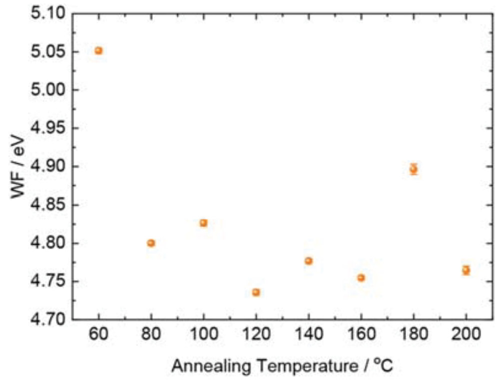

FIGURE 5 | Effect of annealing temperature on the WF of the surface of MoO_3 thin films deposited on ITO-coated glass slides.

recombine only with the minority carriers (electrons), leading to only small photovoltage losses. However, a potential barrier at the MoO_3/TaTm interface can still hinder their efficient collection at the front contact, reducing the FF of the solar cells. This barrier would also justify the series resistance observed for these diodes (**Figure 3**).

In order to shed light on the origin of this phenomena, we performed Kelvin probe measurements on the surface of MoO_3 as a function of the annealing temperature. We have to note that the experiments were performed in air, and hence the extracted work function (WF) values are affected by spontaneous adsorptions of atmospheric contaminants on the surface of MoO_3. We observed a WF = 5.05 eV for the sample annealed at 60°C, while for higher temperatures, the MoO_3 WF was found to decrease of ∼0.2 eV (**Figure 5**). This WF reduction qualitatively agrees with the trend of the FF observed for cells with annealed solely on MoO_3, presented in **Figure 2C**. Hence the electrode WF might be held responsible for the extraction barrier and recombination at the front contact. The variation of the WF of MoO_3 with annealing is likely a consequence of increasing oxygen vacancies (Greiner et al., 2012), as in general reducing the oxidation state of any cationic center (such as by removal of oxygen) tends to decrease the metal oxide WF (Dasgupta et al., 2013). As Kelvin Probe is a surface sensitive technique, we could not extract meaningful information for the MoO_3 films coated with TaTm. In that case, the loss of oxygen upon annealing might be attenuated by the physical barrier of TaTm itself, leading to a better ohmic contact within the MoO_3/TaTm interface (Pérez-del-Rey et al., 2019). Additionally, considering the high work function of MoO_3, hole transfer from the TaTm to MoO_3 is likely to occur (Xu et al., 2016), resulting in interfacial doping of TaTm and hence beneficial charge extraction.

In summary, the power conversion efficiencies of p-i-n PSCs can be modulated through the optimal processing of the MoO_3/TaTm HTLs. We observed that having the TaTm deposited and annealed together with the MoO_3 leads to large improvements in fill factor (>80%) and PCE (>18%) at any annealing temperature or light intensity, with the best results obtained for annealing at 140°C. These enhancements are accounted to an improved hole extraction rate and adjusted ohmic contact at the anode, which are likely due to an increased ITO/MoO_3 electrode work function.

DATA AVAILABILITY STATEMENT

The datasets generated for this study are available on request to the corresponding author.

AUTHOR CONTRIBUTIONS

AB, KZ, and LG-E fabricated and characterized the solar cells. DP-d-R and PB performed part of the characterization. MS and HB conceived the idea and directed the overall project. AB, KZ, and MS wrote the manuscript. All authors read and commented on the manuscript.

ACKNOWLEDGMENTS

Financial support is acknowledged from the Spanish Ministry of Economy and Competitiveness (MINECO) via the Unidad de Excelencia María de Maeztu MDM-2015-0538, MAT2017-88821-R, RTI2018-095362-A-I00, PCIN-2015-255, PCIN-2017-014, and the Generalitat Valenciana (Prome-teo/2016/135). KZ acknowledge the financial support from Fundação de Amparo à Pesquisa do Estado de São Paulo for financing a postdoctoral scholarship (2018/05152-7). MS thanks the MINECO for their RyC contracts.

SUPPLEMENTARY MATERIAL

The Supplementary Material for this article can be found online at: https://www.frontiersin.org/articles/10.3389/fchem.2019.00936/full#Supplementary-Material

REFERENCES

Al-Ashouri, A., Magomedov, A., Roß, M., Jošt, M., Talaikis, M., Chistiakova, G., et al. (2019). Conformal monolayer contacts with lossless interfaces for perovskite single junction and monolithic tandem solar cells. *Energy Environ. Sci.* 12, 3356–3369. doi: 10.1039/C9EE02268F

Avila, J., Gil-Escrig, L., Boix, P. P., Sessolo, M., Albrecht, S., and Bolink, H. J. (2018). Influence of doped charge transport layers on efficient perovskite solar cells. *Sustain. Energy Fuels* 2, 2429–2434. doi: 10.1039/C8SE00218E

Ávila, J., Momblona, C., Boix, P. P., Sessolo, M., and Bolink, H. J. (2017). Vapor-deposited perovskites: the route to high-performance solar cell production? *Joule* 1, 431–442. doi: 10.1016/j.joule.2017.07.014

Dasgupta, B., Goh, W. P., Ooi, Z. E., Wong, L. M., Jiang, C. Y., Ren, Y., et al. (2013). Enhanced extraction rates through gap states of molybdenum oxide anode buffer. *J. Phys. Chem. C* 117, 9206–9211. doi: 10.1021/jp3114013

Green, M. A., Dunlop, E. D., Levi, D. H., Hohl-Ebinger, J., Yoshita, M., and Ho-Baillie, A. W. Y. (2019). Solar cell efficiency tables (version 54). *Prog. Photovoltaics Res. Appl.* 27, 565–575. doi: 10.1002/pip.3171

Greiner, M. T., Chai, L., Helander, M. G., Tang, W., and Lu, Z. (2012). Transition metal oxide work functions : the influence of cation oxidation state and oxygen vacancies. *Adv. Funct. Mater*. 22, 4557–4568. doi: 10.1002/adfm.201200615

Liu, Z., Krückemeier, L., Krogmeier, B., Klingebiel, B., Márquez, J. A., Levcenko, S., et al. (2019). Open-circuit voltages exceeding 1.26 V in planar methylammonium lead iodide perovskite solar cells. *ACS Energy Lett.* 4, 110–117. doi: 10.1021/acsenergylett.8b01906

Momblona, C., Gil-Escrig, L., Bandiello, E., Hutter, E. M., Sessolo, M., Lederer, K., et al. (2016). Efficient vacuum deposited p-i-n and n-i-p perovskite solar cells employing doped charge transport layers. *Energy Environ. Sci.* 9, 3456–3463. doi: 10.1039/C6EE02100J

Pérez-del-Rey, D., Gil-Escrig, L., Zanoni, K. P. S., Dreessen, C., Sessolo, M., Boix, P. P., et al. (2019). Molecular passivation of MoO3: band alignment and protection of charge transport layers in vacuum-deposited perovskite solar cells. *Chem. Mater.* 31, 6945–6949. doi: 10.1021/acs.chemmater.9b01396

Pham, H. D., Xianqiang, L., Li, W., Manzhos, S., Kyaw, A. K. K., and Sonar, P. (2019). Organic interfacial materials for perovskite-based optoelectronic devices. *Energy Environ. Sci.* 12, 1177–1209. doi: 10.1039/C8EE02744G

Schloemer, T. H., Christians, J. A., Luther, J. M., and Sellinger, A. (2019). Doping strategies for small molecule organic hole-transport materials: impacts on perovskite solar cell performance and stability. *Chem. Sci.* 10, 1904–1935. doi: 10.1039/C8SC05284K

Schulz, P., Tiepelt, J. O., Christians, J. A., Levine, I., Edri, E., Sanehira, E. M., et al. (2016). High-work-function molybdenum oxide hole extraction contacts in hybrid organic–inorganic perovskite solar cells. *ACS Appl. Mater. Interfaces* 8, 31491–31499. doi: 10.1021/acsami.6b10898

Schulz, P., Whittaker-Brooks, L. L., MacLeod, B. A., Olson, D. C., Loo, Y.-L., and Kahn, A. (2015). Electronic level alignment in inverted organometal perovskite solar cells. *Adv. Mater. Interfaces* 2:1400532. doi: 10.1002/admi.201400532

Sherkar, T. S., Momblona, C., Gil-Escrig, L., Ávila, J., Sessolo, M., Bolink, H. J., et al. (2017). Recombination in perovskite solar cells: significance of grain boundaries, interface traps, and defect ions. *ACS Energy Lett.* 2, 1214–1222. doi: 10.1021/acsenergylett.7b00236

Shin, S. S., Lee, S. J., and Seok, S. I. (2019). Metal oxide charge transport layers for efficient and stable perovskite solar cells. *Adv. Funct. Mater.* 29:1900455. doi: 10.1002/adfm.201900455

Tress, W., Yavari, M., Domanski, K., Yadav, P., Niesen, B., Correa Baena, J. P., et al. (2018). Interpretation and evolution of open-circuit voltage, recombination, ideality factor and subgap defect states during reversible light-soaking and irreversible degradation of perovskite solar cells. *Energy Environ. Sci.* 11, 151–165. doi: 10.1039/C7EE02415K

Xu, J., Voznyy, O., Comin, R., Gong, X., Walters, G., Liu, M., et al. (2016). Crosslinked remote-doped hole-extracting contacts enhance stability under accelerated lifetime testing in perovskite solar cells. *Adv. Mater.* 28, 2807–2815. doi: 10.1002/adma.201505630

Zanoni, K. P. S., Pérez-del-Rey, D., Dreessen, C., Angeles Hernández-Fenollosa, M., de Camargo, A. S. S., Sessolo, M., et al. (2019). Use of hydrogen molybdenum bronze in vacuum-deposited perovskite solar cells. *Energy Technol.* 1900734. doi: 10.1002/ente.201900734. [Epub ahead of print].

Conflict of Interest: The authors declare that the research was conducted in the absence of any commercial or financial relationships that could be construed as a potential conflict of interest.

SUPPORTING INFORMATION

Efficient vacuum deposited p-i-n perovskite solar cells by front contact optimization

Azin Babaei [1]*, Kassio P. S. Zanoni* [1*]*, Lidón Gil-Escrig* [2]*, Daniel Pérez-del-Rey* [1]*, Pablo P. Boix, Michele Sessolo* [1]** and Henk J. Bolink* [1]

[1] *Instituto de Ciencia Molecular, Universidad de Valencia, C/ Catedrático J. Beltrán 2, 46980 Paterna, Spain*
[2] *Helmholtz-Zentrum Berlin für Materialien und Energie GmbH, Kekulestraße 5, 12489 Berlin, Germany*
Corresponding authors: zanoni@ifsc.usp.br; michele.sessolo@uv.es

Experimental Section

Photolithographically patterned ITO coated glass substrates were purchased from Naranjo Substrates. N4,N4,N4′,N4′-tetra([1,1′- biphenyl]-4-yl)-[1,1′:4′,1′-terphenyl]-4,4′-diamine (TaTm) was provided by Novaled GmbH and Fullerene (C_{60}) was purchased from Sigma Aldrich. PbI_2, CH_3NH_3I (MAI), MoO_3, and bathocuproine (BCP) were purchased from Lumtec.

Device Fabrication. ITO prepatterned substrates were cleaned following a standard procedure in which they are sequentially cleaned with soap, water, deionized water, and isopropanol in a sonication bath, followed by UV treatment for 20 min. All the solar cell layers were prepared by thermal vacuum deposition performed in vacuum chambers evacuated to a pressure of 10^{-6} mbar, which were integrated into a nitrogen-filled glovebox (H_2O and $O_2 < 0.1$ ppm). In general, the vacuum chambers were equipped with temperature controlled evaporation sources (Creaphys) fitted with ceramic crucibles. The sources were directed upward with an angle of approximately 90° with respect to the bottom of the evaporator. The distance between the substrate holder and the evaporation source was approximately 20 cm. Individual quartz crystal microbalance (QCM) sensors monitored the deposition rate of each evaporation source and another one close to the substrate holder monitored the total deposition rate. TaTm, $MAPbI_3$, C_{60} and BCP were sublimed in the same vacuum chamber at temperatures ranging from 60 to >300 °C, depending on the material, and the precise evaporation rate and deposited film thickness were controlled by the QCM sensors. In general, the deposition rate for TaTm and C_{60} was 0.5 Å s^{-1} while the thinner BCP layer was evaporated at 0.2−0.3 Å s^{-1}. For the perovskite deposition, MAI and PbI_2 were co-evaporated at the same time by measuring the deposition rate of each material in two different sensors (with rates of 1.0 and 0.6 Å s^{-1}, respectively) and obtaining the total perovskite thickness in the third one, leading to a 600 nm-thick perovskite. MoO_3 and Ag were evaporated in another vacuum chamber using aluminum boats as sources by applying currents ranging from 2.0 to 4.5 A.

General characterizations. For the solar cell characterization, the J−V curves were recorded using a Keithley 2612A SourceMeter in a −0.2 and 1.2 V voltage range, with 0.01 V steps and integrating the signal for 20 ms after a 10 ms delay, corresponding to a speed of about 0.3 V s^{-1}. The devices were illuminated under a Wavelabs Sinus 70 LED solar simulator. The light intensity was calibrated before every measurement using a calibrated Si reference diode equipped with an infrared cut-off filter (KG-3, Schott). Intensity dependent measurements where carried out by collecting J-V curves with different neutral density filters of decreasing optical density. The layout used to test the solar cells has four equal areas (0.083 cm^2, defined as the overlap between the ITO and the top metal contact) and measured through a shadow mask with 0.050 cm^2 aperture. The work functions were determined by Kelvin probe measurements using an Ambient Pressure Photoemission Spectroscopy system from KP Technology.

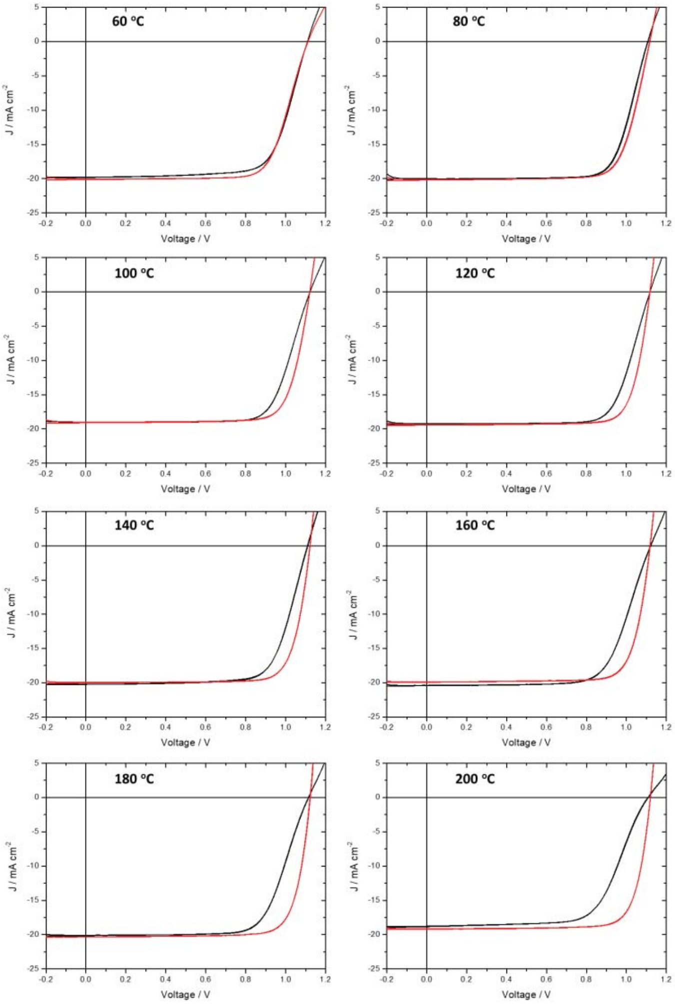

Figure S1. Illuminated JV curves of ITO/MoO_3/TaTm/$MAPbI_3$/C_{60}/BCP/Ag solar cells, with annealing of MoO_3 at different temperatures performed before (black line) or after (red line) the deposition of TaTm.

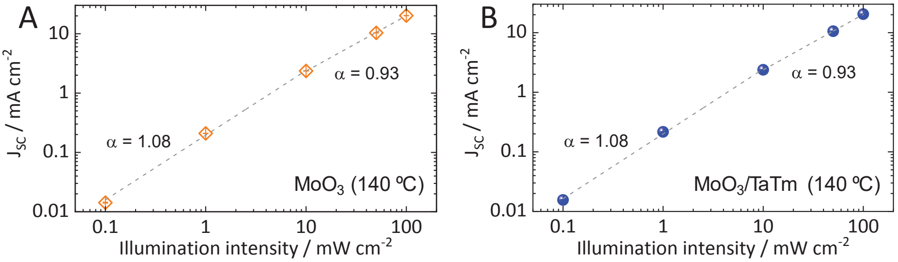

Figure S2. Intensity dependent photocurrent of the perovskite solar cells with p-contacts annealed at 140 ºC. The intensity dependent short-circuit current densities for cells with annealing on (A) the bare MoO_3 and on (B) the MoO_3/TaTm bilayer has been fitted with a power law $J \propto I^{\alpha}$, where I is the incident light intensity.

Chapter 6.

General conclusions

6. General conclusions

The aim of this thesis was the development of materials and device architectures for the preparation of efficient vacuum deposited perovskite solar cells. The effect of different charge transport layers, interfacial materials and electrodes on the performance of perovskite solar cells was studied. Emphasis was placed on the importance of reducing non-radiative recombination within the perovskite and at the interfaces, which is the key to maintain high photovoltage in a solar cell.

In chapter 3, a novel approach to prepare mixed iodide-chloride perovskites, using three-source vacuum deposition technique, was presented. $MAPbI_{3-x}Cl_x$ perovskite films showed a homogenous morphology and good crystallinity, and were hence used to fabricate thin-film diodes to examine the optoelectronic properties. Under illumination, the photovoltage was found to be larger as compared to pure iodide perovskite, reaching 1.13 V and a power conversion efficiency exceeding 16%. In forward bias, we detected intense electroluminescence with a quantum yield of 0.3%, similar to that of state-of-the-art evaporated MAPbI3 solar cells. The high quantum yield for electroluminescence together with the long photoluminescence lifetime suggests a reduction of the non-radiative recombination rate.

The importance of the choice of suitable interfacial charge transport layers, electrodes, and their combinations, was highlighted in chapter 4. The $MAPbI_3$ perovskite layer was deposited by dual source vacuum deposition. BCP, Liq and their combination were used as interlayers between the electron transport layer and the top electrode. We observed that BCP and Liq can lead to devices with high rectification, fill factor, and photovoltage. We also observed that the use of low work function metals, such as Ba, can be beneficial for the reduction of non-radiative recombination, although at the price of the device stability.

In chapter 5, the optimization of the front contact in perovskite solar cells was investigated. As in chapter 4, the $MAPbI_3$ perovskite film was deposited by dual source vacuum deposition. The hole transport layer which was used to fabricate the perovskite solar cells is TaTm. To ensure an ohmic contact between the TaTm layer and the ITO, an additional MoO_3 layer was placed in between the two materials. The hole extraction properties of the MoO_3/TaTm was evaluated by selectively annealing either MoO_3 (prior to the deposition of TaTm) or the bilayer MoO_3/TaTm (without pre-treatment on the MoO_3), at temperature ranging from 60 °C to 200 °C. We observed that having TaTm deposited and annealed together with the MoO_3 layer led to large improvement in fill factor (80%) and power conversion efficiency (> 18%) at any annealing temperature, with the best results obtained at 140 °C.

Chapter 7.

Resumen en Castellano

Resumen en Castellano

1.1. Introducción

Las fuentes de energía renovables se están convirtiendo en un componente importante de la producción mundial de energía como consecuencia de los problemas ambientales relacionados con el uso de combustibles fósiles, en particular la liberación de gases de efecto invernadero, que contribuyen al calentamiento global. A pesar del reciente y significativo aumento en el uso y la eficiencia de las energías renovables, la mayor parte de la demanda mundial de energía aún se satisface con combustibles fósiles (≈ 80%).[1] Todos los procesos asociados con la extracción, transporte, refinamiento, y consumo de combustibles fósiles tienen un impacto nocivo en el medio ambiente. Una solución para satisfacer la demanda mundial de energía reduciendo el impacto ambiental es la implementación de fuentes de energía renovables. Las características más importantes de los recursos de energía renovable son el bajo impacto ambiental y su abundancia.

La irradiación solar es la fuente de energía más abundante en la tierra, y entre las tecnologías disponibles para cosecharla, la fotovoltaica (FV) es una de las más prometedoras. Un sistema fotovoltaico consta de varios componentes, entre los que destacan las células solares que pueden absorber y convertir la energía solar en electricidad. A pesar de las ventajas de la tecnología FV, aún se considera un sustituto costoso de los combustibles fósiles convencionales. Para hacer que la energía fotovoltaica sea más competitiva en el mercado energético, se requiere una reducción sustancial de los costes de los módulos fotovoltaicos y nuevas formas de almacenamiento de energía.

Las células solares se dividen generalmente en tres principales categorías o generaciones. Las células solares de primera generación utilizan silicio cristalino (c-Si) y representan la tecnología fotovoltaica más antigua disponible comercialmente. Las células solares de Si tienen un rendimiento relativamente alto, pero como se requiere Si de alta pureza, y debido al consumo de energía del proceso de purificación, el precio sigue siendo relativamente alto en comparación con el coste asociado a las fuentes tradicionales. Otra tecnología fotovoltaica ampliamente estudiada comprende las células solares de segunda generación o células solares de capa fina porque están hechas de capas delgadas de materiales semiconductores como telururo de cadmio (CdTe), arseniuro de galio (GaAs) o seleniuro de cobre, indio y galio (CIGS). Las células solares de CdTe y CIGS son potencialmente más baratas de fabricar en comparación con los dispositivos de primera generación, pero tienen menor eficiencia. Lo contrario vale para las células solares de GaAs, que son más eficientes pero más costosas.[2] La tercera generación de células solares está hecha de materiales orgánicos, puntos cuánticos y semiconductores híbridos que ofrecen, en principio, menores costes de producción y una fabricación más simple. Los más recientes avances en este campo se centran en las células solares basadas en una clase de materiales llamados perovskitas, que podrían emplearse en paneles solares más baratos y eficientes.[3]

1.2. Perovskitas híbridas: estructura, propiedades y desafíos

El término "perovskita" se utilizó para designar la estructura cristalina del titanato de calcio, que fue descubierto en 1839 por el mineralogista alemán Gustav Rose, y nombrado en honor del mineralogista ruso Lev Perovski.[6] Las perovskitas de haluro metálico se pueden clasificar en dos grupos, las inorgánicas, que contienen cationes alcalinos, y las perovskitas híbridas basadas en cationes orgánicos,, siendo ambas materiales semiconductores.[7] Las perovskitas híbridas tridimensionales comparten la fórmula general ABX_3, donde A es un catión orgánico, B es un metal divalente y X es un anión haluro.

El conocimiento de las propiedades ópticas y eléctricas de las perovskitas, como la energía de banda prohibida, la movilidad de electrones y huecos, la longitud de difusión y el tiempo de vida de los portadores de carga, es esencial para la fabricación de dispositivos optoelectrónicos. Aquí resumimos algunas de las propiedades optoelectrónicas de las perovskitas:

- Alto coeficiente de absorción.
- Fácil control del ancho de banda prohibida.
- Alta movilidad de electrones y huecos.
- Baja energía de enlace de los excitones.

Aunque las células solares de perovskita ya han logrado un rendimiento comparable a los dispositivos basados en Si, todavía quedan obstáculos para su aplicación a gran escala . Algunos de ellos son:

- Histéresis en la característica corriente-tensión: Su origen podría ser la migración de iones, la acumulación de carga, o ambos.
- Toxicidad: Proviene del uso de plomo como catión divalente en la estructura cristalina de la perovskita.
- Estabilidad, tanto de la estructura cristalina, como estabilidad térmica y del dispositivo.

1.3. Arquitectura de las células solares

La primera célula solar de perovskita se diseñó tomando como base la estructura de las células solares sensibilizadas con colorantes, donde las perovskitas se investigaron como un "nuevo" colorante en combinación con un electrolito líquido y con capas de transporte de electrones de TiO_2 mesoporoso.[46] Se observó que, en comparación con colorantes moleculares, la perovskita es un mejor absorbente de luz, a pesar de que el electrolito líquido dañaba la perovskita provocando la degradación del dispositivo.[47] Esto impulsó a que los investigadores combinaran características de célula solar de película fina y célula solar sensibilizada por colorante, en particular la sustitución del electrolito líquido con capas orgánicas de transporte de huecos, resultando en una mejora del rendimiento y de la estabilidad del dispositivo.[48]

Se ha demostrado que las células solares de perovskita también se pueden fabricar en una configuración plana donde la capa activa se intercala entre dos capas de transporte de carga.[48,49] Las capas de transporte de carga son materiales semiconductores con niveles de energía elegidos para que puedan transportar selectivamente los electrones y huecos fotogenerados desde la perovskita a los electrodos externos. La arquitectura del dispositivo juega un papel importante a la hora de determinar la eficiencia de la extracción de carga. Las células solares de perovskita pueden dividirse en dos clases: planares y mesoporosas, y dentro de estas estructuras existen a su vez dos tipos de configuración, p-i-n y n-i-p. Si se extraen huecos en el contacto transparente frontal (mediante un semiconductor de tipo p), la célula solar se denomina p-i-n, y viceversa para los dispositivos n-i-p.

En esta tesis, se ha utilizado la configuración p-i-n para la fabricación de las células solares de perovskita.

1.4. Física de células solares

El funcionamiento básico de una célula solar y su eficiencia correspondiente implica, de forma resumida, los procesos siguientes.

- *Absorción de fotones y generación de carga*: cuando la luz incidente es absorbida por la perovskita, se generan electrones y huecos libres. Los electrones y huecos se generarán siempre que el fotón incidente tenga una energía mayor que la de la banda prohibida del semiconductor.
- *Recombinación:* Los electrones y huecos fotogenerados pueden recombinarse a través de un proceso opuesto a la generación. Comprender y controlar los procesos de recombinación es de gran importancia ya que al reducir la concentración de portadores de carga se reduce la eficiencia de conversión de energía. Los electrones excitados pueden volver a la banda de valencia y su energía se liberará en forma de fotones (recombinación radiativa) o calor (recombinación no radiativa).
- *Transporte de carga y recolección:* hay dos mecanismos de transporte involucrados en la recolección de cargas, la corriente de difusión y de deriva. Cuando existe un gradiente de concentración de carga en el semiconductor, las cargas se moverán, en el proceso de difusión, de áreas de alta concentración a áreas con baja concentración. La corriente de deriva es consecuencia de la presencia del campo eléctrico en el material, y es importante a voltajes

cercanos o por encima del punto de máxima potencia de la célula solar.

1.5. Caracterización de células solares

Una de las medidas más básicas de los dispositivos de semiconductores y, en particular, de las células solares, es la medición de la corriente al variar el voltaje, llamada característica IV. Simplemente se mide la corriente generada en función de la tensión aplicada bajo iluminación utilizando un simulador solar calibrado. De las características IV pueden extraerse varios parámetros fundamentales:

- Corriente de cortocircuito (I_{sc}, mA cm^{-2}, es la corriente a voltaje igual a 0 V)
- Voltaje en circuito abierto (V_{OC}, V, es el voltaje cuando la corriente es cero y es el máximo voltaje generado por una célula solar.)
- Factor de forma o “fill factor” (FF, %, se define como la relación entre el punto de máxima potencia y el producto $V_{OC}{\cdot}J_{SC}$)
- Eficiencia de conversión de potencia (PCE, %, la fracción de potencia incidente, irradiación solar, que se convierte en potencia eléctrica)

1.6. Importancia de las capas de transporte de cargas

Para fabricar células solares de perovskita eficientes, no solo la calidad de la película de perovskita, sino también las propiedades de las capas de transporte de carga, juegan un papel importante. Las características de transportadores de electrones y huecos, como la movilidad de carga, la alineación de los niveles de energía, la morfología y la densidad de defectos, también determinan en última instancia el rendimiento de la célula solar.

En el capítulo 1.2, se discutió la movilidad de electrones y huecos en las películas de perovskita y su importancia en el rendimiento de las células solares. De manera similar, también se desea una alta movilidad de electrones/huecos en las capas selectivas de transporte, ya que los portadores de carga deben moverse eficientemente hacia los electrodos.

La selectividad de las capas de transporte de carga viene dada principalmente por la alineación del nivel de energía en la interfaz de la capa de transporte/perovskita. Si no existe una gran barrera de energía en la interfaz de la capa de perovskita y la capa de transporte de electrones (ETL), los electrones libres se pueden extraer eficientemente de la banda de conducción de la perovskita al nivel molecular desocupado más bajo (LUMO) de la capa de transporte de electrones. Simultáneamente, la transferencia de huecos en esta interfaz debe inhibirse maximizando la diferencia de energía entre la banda de valencia de la perovskita y el nivel molecular ocupado más elevado (HOMO) de la capa de transporte de electrones. Deben cumplirse características similares pero energéticamente opuestas para garantizar una extracción de carga selectiva en la interfaz entre la perovskita y la capa de transporte de huecos (HTL).

Los materiales orgánicos de transporte de electrones tienen estructuras y niveles energéticos ajustables para adaptarse a la capa de perovskita. El fullereno y sus derivados, como $PC_{61}BM$, ICBA y $PC_{71}BM$, son buenos candidatos para ser usados como materiales selectivos de extracción de electrones debido a su alineación adecuada del LUMO, buena movilidad de electrones y a la facilidad de deposición en capa delgada.[61–64] Los fullerenos como C_{60} y C_{70} tienen mayor movilidad de electrones y pueden además depositarse por sublimación en vacío. En los dispositivos p-i-n, la capa de transporte de huecos actúa no solo como una capa selectiva, sino también como una ventana donde la luz accede al dispositivo. Por lo tanto, sus propiedades ópticas también son críticas para maximizar la generación de corriente en las células solares de perovskita. Para evitar la pérdida de fotones, se debe tener en cuenta el ancho de banda de la capa de transporte del hueco, su índice de refracción y coeficiente de extinción.[65] Hasta la fecha, se han probado un gran número de moléculas orgánicas, materiales inorgánicos y polímeros conductores en células solares de perovskita como capas de transporte de huecos. Los materiales de transporte de huecos más comunes en las células de tipo p-i-n incluyen PEDOT: PSS, PTAA, óxido de grafeno, NiO y CuSCN.[63,68–71]

El rendimiento de una célula solar está influenciado además por la interfaz entre las capas de transporte de carga y los electrodos. En general, para garantizar una extracción de carga óhmica, se debe minimizar la diferencia de energía entre la función de trabajo del electrodo y los orbitales fronterizos del material de transporte. Por lo tanto, generalmente se coloca una capa intermedia adicional entre el electrodo y la capa de transporte.[72] En las células solares tipo p-i-n, materiales interfaciales comunes son moléculas con baja energía de ionización,[73] semiconductores orgánicos dopados[72,74] y óxidos metálicos (MoO_3, V_2O_5 y WO_3)[75]. Asimismo, se ha probado una amplia variedad de materiales interfaciales, tales como óxidos metálicos, materiales orgánicos y polímeros, metales y sales metálicas, para su uso entre las capas de transporte de electrones y el electrodo metálico.

Objetivo de la tesis

El objetivo de esta tesis es el desarrollo de métodos de deposición en vacío para la fabricación de películas finas de perovskita, y su incorporación en células solares utilizando diferentes capas de transporte de carga. Más allá del desarrollo de la deposición en vacío de las propias perovskitas, la ingeniería de las interfaces es muy importante para aumentar el rendimiento de las células solares de perovskita. Por lo tanto, en esta tesis se estudia la influencia de diferentes capas de transporte de carga y materiales interfaciales en el rendimiento de las células solares de perovskita. El trabajo se ha estructurado en los siguientes capítulos:

- Preparación y caracterización de películas finas de perovskitas de haluro mixto $MAPbI_{3-x}Cl_x$ mediante deposición en vacío de tres fuentes:
  Este capítulo versa sobre la fabricación de células solares de perovskita de haluro mixta. Se han realizado optimizaciones en la co-evaporación de las tres fuentes para lograr capas delgadas de semiconductor del tipo $MAPbI_{3-x}Cl_x$.

- Células solares de perovskita de alto voltaje procesadas mediante vacío con capas interfaciales orgánicas:
  En este capítulo se ha estudiado el efecto de diferentes capas de transporte de electrones y cátodos metálicos sobre el rendimiento de las células solares.

- Células solares de perovskita p-i-n eficientes depositadas en vacío mediante optimización del contacto frontal:
  En este capítulo se ha llevado a cabo la optimización de la interfaz entre la capa de transporte de huecos y la perovskita

Metodología

2.1. Materiales y precursores

En esta tesis se han preparado varias arquitecturas de células solares. Todos los dispositivos se fabricaron sobre sustratos de vidrio recubiertos con óxido de indio y estaño (ITO) comprados a Julius. El óxido de molibdeno (MoO_3), $PbCl_2$, PbI_2, MAI, BCP y Liq se compraron a Lumtec. El TaTm fue proporcionado por Novaled. C_{60} fue comprado en Sigma-Aldrich.

2.2. Fabricación de células solares de perovskita

Las películas de perovskita y las capas de transporte de carga se pueden depositar mediante procesado desde disolución o mediante métodos de alto vacío. Sin embargo, la facilidad de control sobre los parámetros de deposición, como el tiempo de deposición, la uniformidad de la superficie y el espesor preciso de la capa, hacen que la evaporación por alto vacío sea una técnica particularmente prometedora para fabricar dispositivos de perovskita. En la técnica de deposición en vacío, el catión orgánico y el haluro metálico se subliman térmicamente de forma simultánea en una cámara de alto vacío, donde condensan y reaccionan sobre un sustrato colocado por encima de las fuentes térmicas. En comparación con las técnicas de procesado desde disolución, la técnica de deposición desde vacío tiene una serie de beneficios.

- Alta pureza de los materiales.
- Posibilidad de usar diferentes tipos de material.
- Control fino sobre el espesor de la capa.
- Compatibilidad con diferentes tipos de sustrato.
- Posibilidad de deposición multicapa.

Todas las células solares estudiadas en la tesis tienen una estructura p-i-n con la siguiente arquitectura: Vidrio/ITO/MoO_3/TaTm/perovskita /C60/ETL/metal.

2.3. Técnicas de caracterización de películas

Para caracterizar películas delgadas y células solares se han utilizado diferentes técnicas de caracterización. Estas se resumen a continuación

- Perfilometría de superficie
- Absorción UV-Vis
- Difracción de rayos X
- Microscopía electrónica de barrido
- Espectroscopía de fotoemisión de rayos X
- Medición con sonda Kelvin
- Medición de corriente-voltaje
- Rastreador de punto de máxima potencia
- Medición de fotoluminiscencia resuelta en el tiempo

3. Preparación y caracterización de películas finas de perovskita de haluro mixto $MAPbI_{3-x}Cl_x$ mediante deposición en vacío de tres fuentes

3.1. Introducción

La última generación de dispositivos fotovoltaicos que emplean perovskitas de haluros híbridas exhibe una alta eficiencia de conversión de potencia (PCE), superior al 25%.[1] El ioduro de plomo y metilamonio $MAPbI_3$ es la perovskita híbrida más estudiada en fotovoltaica debido a su simplicidad y buenas propiedades semiconductoras. Las propiedades optoelectrónicas del $MAPbI_3$ pueden mejorarse mediante la introducción de iones de cloro. Cabe destacar como las películas finas de $MAPbI_3$ y $MAPbI_{3-x}Cl_x$ exhiben las mismas propiedades estructurales y ópticas mientras que, cuando se emplean en células solares, muestran un comportamiento significativamente diferente. A pesar de una gran cantidad de estudios tanto teóricos como experimentales, los mecanismos responsables del efecto del cloro en las células solares de perovskita de haluro mixto $MAPbI_{3-x}Cl_x$ siguen sin estar claros.[91–94] Algunos estudios han estimado la longitud de difusión de cargas para películas finas de $MAPbI_3$ y $MAPbI_{3-x}Cl_x$. Se demostró que la longitud de difusión de las películas finas de $MAPbI_3$ preparadas a partir de los precursores MAI y PbI_2 es de aproximadamente 100 nm, mientras que se observó que puede alcanzar 1 µm cuando la perovskita se prepara a partir de $PbCl_2$ y MAI.[16,95] La diferencia en las longitudes de difusión de carga entre $MAPbI_3$ y $MAPbI_{3-x}Cl_x$ se atribuyeron a una morfología diferente de la perovskita tras la incorporación de átomos de Cl.[49] Sin embargo, algunos estudios muestran que el cloro no se incorpora efectivamente a la estructura de $MAPbI_3$ (por debajo del 3 al 4%) y actúa más bien como un dopante. De hecho, no se pueden formar cristales mixtos estables de yoduro/cloruro debido a la gran diferencia entre los radios iónicos de yodo y cloro.[92]

La mayoría de las células solares de perovskita $MAPbI_{3-x}Cl_x$ se han fabricado mediante un proceso de disolución.[13,24,48,98] El control de la concentración de precursores MAX y PbX_2 (X = I o Cl) es muy importante al preparar la perovskita de haluro mixto $MAPbI_{3-x}Cl_x$. Se ha demostrado que la relación final Cl/I en la película de $MAPbI_{3-x}Cl_x$ es menor en comparación con la de la disolución precursora, lo que probablemente se deba a la baja afinidad del cloro en la perovskita de yoduro.[92] En contraste con las técnicas de procesado en disolución, en la deposición térmica en vacío se pueden usar múltiples fuentes para preparar películas finas mixtas de perovskita de haluro con un control superior sobre la estequiometría del material.[99,100]

En este capítulo se presenta la co-deposición en vacío de tres fuentes, usando MAI, $PbCl_2$ y PbI_2 para formar películas de perovskita mixta $MAPbI_{3-x}Cl_x$. Las imágenes de microscopía electrónica de barrido (SEM) de la muestra de haluro mixto mostraron películas altamente uniformes y sin defectos. Estas capas homogéneas se han utilizado para fabricar células solares con la siguiente estructura: $ITO/MoO_3/TaTm/MAPbI_{3-x}Cl_x/C_{60}/BCP/Ag$. Mediante la adición de cloro, se obtuvieron dispositivos con alto V_{OC} (> 1.1 eV). Para investigar el efecto del cloruro en la dinámica de recombinación de carga, llevamos a cabo mediciones de fotoluminiscencia (PL) resuelta en el tiempo, y encontramos un tiempo de vida mucho más largo para las películas de $MAPbI_{3-x}Cl_x$ en comparación con las de $MAPbI_3$. Esto sugiere una reducción de la recombinación no radiativa en las películas de perovskita de haluro mixto depositadas por deposición en vacío.

3.2. Resultados y discusión

En este capítulo presentamos el primer ejemplo de deposición en vacío de tres fuentes de capas delgadas de $MAPbI_{3-x}Cl_x$ utilizando MAI, PbI_2 y $PbCl_2$ como precursores. Teniendo en cuenta la baja solubilidad del cloruro en $MAPbI_3$,[15] se decidió usar la velocidad de deposición controlable más baja para $PbCl_2$ durante el proceso. Por lo tanto, fijamos la velocidad de deposición de $PbCl_2$ en 0.05 Å/s, mientras que el PbI_2 se depositó a una velocidad de 0.6 Å/s. La fuente de MAI se mantuvo a una temperatura fija (85 ^{o}C). Después de la deposición, las películas se calentaron a 100 ^{o}C por diferentes tiempos en una caja seca en nitrógeno. Mediante el análisis XPS, identificamos cloruro en la superficie de las muestras en una concentración aproximadamente 10 veces menor que el yoduro ($MAPbI_{3-x}Cl_x$ con $x \approx 0.3$), un valor que se correlaciona bien con las relaciones entre las velocidades de deposición utilizadas para $PbCl_2$ y PbI_2. El espectro de absorción óptica muestra el perfil esperado para $MAPbI_3$, con la absorción correspondiente a la banda prohibida aproximadamente a 780 nm (1.6 eV). El patrón de difracción de rayos X revela la presencia de una pequeña cantidad de PbI_2 sin reaccionar (12.7°), como se observa a menudo para materiales de perovskita similares. Sin embargo, el patrón de difracción para la estructura de perovskita tetragonal es claramente visible (picos principales a 14.0°, 28.2°), lo que indica que es posible obtener películas $MAPbI_{3-x}Cl_x$ altamente cristalinas con nuestra técnica. Las imágenes de microscopía electrónica de barrido (SEM, figura 1d) muestran películas altamente uniformes y sin defectos, con un tamaño de grano del orden de cientos de nanómetros. Estas características son muy similares a las capas $MAPbI_3$ depositadas en vacío previamente estudiadas.[74]

Las películas de haluros mixtos se probaron entonces en una célula solar en capa fina y se caracterizaron con iluminación equivalente a AM1.5G. Las muestras sin tratamiento térmico posterior muestran una densidad de corriente inusualmente baja (16.4 mA cm^{-2}), acompañada de un FF relativamente bajo (68%). Conviene señalar que el V_{OC} alcanza los 1.13 V, lo que es aproximadamente de 30 a 50 mV más alto en comparación con las células solares de $MAPbI_3$ depositadas en vacío.[74,101] El tratamiento térmico de 2 minutos posterior a la deposición de la película de perovskita resulta en una mejora de la fotocorriente (J_{SC} = 19.0 mA cm^{-2}), con solo pérdidas menores en V_{OC} y FF. Un tratamiento térmico más prolongado (5 minutos) recupera parcialmente la eficiencia de recolección de carga (FF = 73%), lo que lleva a una PCE general de 16.1%. Los tratamientos más largos reducen principalmente el fotovoltaje, que sin embargo sigue siendo notable (1.12 V) para este tipo de materiales.

El diodo de mejor rendimiento se caracterizó además en una esfera integradora para cuantificar su eficiencia de electroluminiscencia (EL). El perfil de densidad de corriente en función del voltaje muestra una corriente de fuga muy baja, con una inyección pronunciada entre 0.6 y 1.1 V, lo que indica una alta calidad de diodo. La EL se detecta aproximadamente a 1.0 V, aumentando rápidamente para alcanzar alrededor de 500 µW cm^{-2} con un voltaje aplicado de 2.0 V. Esto corresponde a una eficiencia cuántica externa (EQE) para EL de 0.3%, que está a la par con las células solares de $MAPbI_3$ depositadas en vacío de mayor rendimiento hasta la fecha.[74] La observación de un EQE alto para la electroluminiscencia sugiere que los mecanismos de recombinación no radiativa disminuyen mediante la incorporación de cloruro, de acuerdo con la literatura sobre materiales similares procesados desde disolución.[16] La disminución de la recombinación no radiativa podría ser causada por una reducción en la concentración de las trampas electrónicas, como resultado de la incorporación de cloruro en los bordes de grano.[102]

La medida del tiempo de vida de PL se ajustó con una función triexponencial, obteniendo un tiempo de vida medio de PL de 300 ns. Este valor es un orden de magnitud mayor en comparación con las películas de $MAPbI_3$ puro depositadas al vacío,[139,140] que se caracterizan típicamente por tiempos de vida de PL muy cortos (<10 ns). Si bien se debe tener cuidado al deducir las propiedades optoelectrónicas mediante técnicas ópticas, el aumento del tiempo de vida de PL sugiere también una reducción de la densidad de trampas o de su profundidad en comparación con el $MAPbI_3$ puro.[141] Estas observaciones son consistentes con la mejora del rendimiento del dispositivo, específicamente con el aumento del V_{OC}, obtenida utilizando las capas de perovskita mixta de haluro.

3.3. Conclusión

Mostramos la formación de la perovskita de haluro mixto $MAPbI_{3-x}Cl_x$ por medio de la evaporación simultánea de los tres compuestos precursores. Bajo iluminación, el fotovoltaje aumenta en comparación con el del $MAPbI_3$ procesado en vacío, alcanzando 1.13 V y una eficiencia de conversión de potencia superior al 16%. Además, detectamos una intensa electroluminiscencia con un rendimiento cuántico del 0.3%, similar al de las mejores células solares de perovskita evaporadas de $MAPbI_3$. Estas observaciones, junto con el alto tiempo de vida de fotoluminiscencia, hacen que la perovskita de haluro mixto sea un buen candidato para células solares eficientes y LED NIR.

Los estudios futuros se centrarán en la optimización de los materiales para lograr una mayor eficiencia de conversión de energía en ambas aplicaciones.

4. Células solares de perovskita de alto voltaje procesadas en vacío con capas interfaciales semiconductoras orgánicas.

4.1. Introducción

En las células solares de perovskita las capas transportadoras de electrones (ETLs) y de huecos (HTLs) juegan un papel importante para el funcionamiento del dispositivo. Para lograr células solares de perovskita de alto rendimiento, el material de transporte de electrones (ETM) debe cumplir varios criterios. Para que el transporte de electrones sea eficiente y selectivo, se necesita que el LUMO del ETM coincida con la banda de conducción de la perovskita mientras que el HOMO tenga una energía más alta comparada con la banda de valencia. Además, el LUMO del ETL tiene que estar cerca en energía de la función de trabajo del electrodo metálico para facilitar la recolección de electrones. Para conseguir este propósito, una estrategia común es el uso de electrodos de baja función de trabajo como el bario o el calcio.[79,111] Otra opción es usar una capa intermedia entre el ETL y el electrodo de metal. La batocuproina (BCP), un semiconductor orgánico con un intervalo ancho de banda de aproximadamente 3.5 eV, es una molécula ampliamente utilizada como capa intermedia en combinación con fullerenos y Ag o Al, y puede depositarse fácilmente en películas capa finas por evaporación térmica.[76,78,112,113] El mecanismo de trabajo de transferencia de electrones a través de BCP todavía es un tema de debate, pero se ha observado que BCP y Ag/Al pueden formar complejos organometálicos que conducen electricidad formando una nueva densidad de estados electrónicos por debajo del LUMO de BCP puro, que mediaría el transporte de carga. Otra capa intermedia que se usó en este capítulo es el quinolato de litio (Liq), que tiene energías HOMO y LUMO de -5.6 eV y -3.2 eV, respectivamente.[114] El Liq se puede evaporar térmicamente y se usa comúnmente en

OLEDs como capa intermedia. Se ha demostrado que el Liq puede formar aniones radicales al reaccionar en contacto con el metal, favoreciendo la inyección de electrones en los OLED.[115]

En este capítulo, el estudio principal se dirige al efecto de estas capas interfaciales, específicamente BCP, y Liq, o la combinación de ellas, sobre el rendimiento de las células solares de perovskita. El electrodo superior utilizado en este capítulo es Ba o Ag y se investiga el efecto general de cada contacto l sobre el V_{OC} y la estabilidad de las células solares de perovskita. En este capítulo se ha estudiado la siguiente arquitectura de dispositivos: ITO/MoO_3/TaTm/$MAPbI_3$/C_{60}/EIL/metal (figura 19). Todas las capas se prepararon por evaporación térmica en cámaras de alto vacío.

4.2. Resultado y discusión

La Tabla 1 resume los parámetros fotovoltaicos que se extrajeron de las curvas JV promedio de todos los dispositivos con diferentes contactos superiores. Existen diferentes hipótesis posibles para explicar la diferencia entre los valores de V_{OC} en diferentes dispositivos.

Top contact	FF (%)	V_{OC} (V ± mV)	J_{SC} (mA cm^{-2})	PCE (%)
BCP	77.8 ± 2.8	1.13 ± 3	20.5 ± 0.1	18.1 ± 0.2
Liq	77.6 ± 1.9	1.13 ± 4	20.4 ± 0.3	18.1 ± 0.3
BCP/Ba	67.1 ± 1.9	1.11 ± 2	20.7 ± 0.5	15.7 ± 0.1
BCP/Liq	78.3 ± 0.2	1.12 ± 6	20.6 ± 0.7	18.4 ± 0.2
Ba	71.8 ± 1.8	1.15 ± 7	20.7 ± 0.7	17.1 ±0.6

Tabla 1. Parámetros fotovoltaicos promedios con desviación estándar σ extraídos de curvas JV en células solares con diferentes contactos superiores.

En dispositivos optoelectrónicos, la recombinación no radiativa reduce la separación de los cuasi- niveles de Fermi- (QFLS) y, por lo tanto, limita el máximo V_{OC} alcanzable. Como en las perovskitas la recombinación se produce a partir de portadores de carga libre, el QFLS puede estar directamente relacionado con el rendimiento cuántico de fotoluminiscencia de la perovskita.[116] Teniendo esto en cuenta, realizamos mediciones de PL de células solares completas en una esfera integradora iluminando el dispositivo con un láser de 515 nm. Para asegurar que todos los dispositivos tienen la misma concentración de portadores de carga, ajustamos la potencia del láser para que el la J_{SC} de las células coincida con la obtenida bajo iluminación equivalente a AM 1.5G

Los espectros de PL de todos los dispositivos con diferente contacto superior exhiben un máximo centrado en 1.58 eV. La máxima intensidad de PL se observó para el dispositivo con un electrodo de Ba depositado directamente sobre C_{60}, lo que indica que la función de trabajo del Ba tiene una influencia positiva en la recombinación de carga en la célula solar. Los dispositivos con Liq y BCP mostraron la menor intensidad de PL, aunque se caracterizaron por un alto V_{OC}, mientras que los dispositivos que emplearon BCP/Liq y BCP/Ba dieron como resultado una PL más intensa. Estas observaciones sugieren que el fotovoltaje final está determinado por diferentes mecanismos competitivos. Curiosamente, tanto la función de trabajo del electrodo como el tipo de capa intermedia pueden influir en el PL del $MAPbI_3$. Una hipótesis para explicar este efecto es la alteración directa de la función de trabajo de la película $MAPbI_3$ por la superficie superior. Sin embargo, la medición directa de la función de trabajo de estos materiales es difícil ya que la interfaz está enterrada dentro del dispositivo. Ya se ha mostrado que el nivel de Fermi de la perovskita se puede modular cambiando el sustrato. Por ejemplo, los sustratos de tipo p inducen un carácter de tipo p en la perovskita misma.[57,117,118] Por lo tanto, podemos suponer que el nivel de Fermi del $MAPbI_3$ también está influenciado por el contacto superior.

Se ha estudiado la evolución de la PCE a lo largo del tiempo para la serie de dispositivos. Aquellos que emplean Ba como electrodo (ya sea solo o en combinación con BCP) muestran un rápido aumento inicial de la eficiencia (hasta aproximadamente el 19%) seguido de una disminución relativamente rápida. Esto no es sorprendente ya que el Ba es extremadamente reactivo y, por lo tanto, se necesita una encapsulación más rigurosa para evitar su reacción en presencia de oxígeno y/o humedad del aire. Se observaron perfiles de degradación similares, pero con una estabilidad mucho más larga para dispositivos que emplean BCP y BCP/Liq en combinación con el electrodo Ag. El dispositivo que empleaba la capa delgada intermedia de Liq entre C_{60} y Ag, mostró un aumento inicial de la eficiencia (hasta el 19.5% después de 1 día) nuevamente seguido de una disminución lenta, alcanzando aproximadamente el 16% después de 6 días de funcionamiento. Se han propuesto varios mecanismos responsables de la degradación de las células solares de perovskita, siendo el más relevante la migración de haluros e iones metálicos.[119–121] En particular, los principales procesos que conducen a la degradación de las células solares de perovskita es son la difusión de haluros al electrodo, así como la migración opuesta de átomos de metal desde el electrodo a la película de perovskita.[122,123] Considerando esto, la corta vida útil de las células solares con una capa delgada (2 nm) de Liq entre el C_{60} y el Ag podría estar relacionada con una interdifusión más rápida de especies entre el electrodo y la película de MAPbI3. La barrera adicional proporcionada por la BCP puede aliviar este efecto, resultando en los tiempos de vida más largos observados en estos casos.

4.3. Conclusión

Se ha estudiado el efecto de dos semiconductores orgánicos, BCP y Liq, como materiales de transporte de electrones, en el rendimiento de las células solares de $MAPbI_3$ procesadas al en vacío. Los semiconductores orgánicos utilizados tradicionalmente en células solares (BCP) y OLED (Liq) pueden conducir a dispositivos con alta rectificación, factor de forma y fotovoltaje. También observamos cómo se reduce la recombinación no radiativa cuando se intercambia el contacto superior de Ag con un metal de baja función de trabajo, como Ba. Sin embargo, en este caso, la estabilidad del dispositivo disminuye como consecuencia de la mayor reactividad del metal. La estabilidad del dispositivo a largo plazo se observó solo en presencia de BCP, con o sin la capa de Liq. Se deben realizar más estudios para comprender la interacción de los metales y las capas intermedias y su efecto sobre el rendimiento y la vida útil de las células solares de perovskita**.**

5. Células solares de perovskita p-i-n eficientes depositadas en vacío mediante optimización de contacto frontal

5.1. Introducción

En las células solares de tipo p-i-n, el HTL juega un papel significativo en el funcionamiento general del dispositivo, debido a que la concentración de carga en el contacto frontal HTL/perovskita es mayor. Como se mencionó anteriormente, un HTL adecuado debería confinar electrones y extraer huecos de manera eficiente, evitando pérdidas de recombinación no radiativa en la interfaz HTL/perovskita. Para garantizar una extracción selectiva de los huecos, el HOMO del material de transporte de huecos (HTM) debe estar alineado con la banda de valencia de la perovskita (-5.4 eV para $MAPbI_3$). Por otro lado, su afinidad electrónica debería ser lo suficientemente baja como para bloquear los electrones dentro de la perovskita. Por esta razón, los semiconductores con ancho de banda grande se utilizan a menudo como HTL. Un electrodo transparente ampliamente adoptado en las células solares p-i-n es el óxido de indio y estaño (ITO), con una función de trabajo de aproximadamente 4.7 eV. Como el requisito para un HTL es tener un HOMO cercano en energía al máximo de la banda de valencia de la perovskita, el uso de ITO conlleva una barrera para la inyección/extracción de huecos de hasta 0.7 eV. Un método común para reducir esta barrera es utilizar una capa intermedia entre el electrodo y el HTL, formada por un material con alta función de trabajo: comúnmente se utilizan óxidos metálicos como NiO_x, V_2O_5 o MoO_3.[101,108,125,126] EL MoO_3 es un material prometedor y versátil debido a la facilidad de procesado, baja toxicidad, estabilidad ambiental y sobre todo por su función de trabajo muy alta.[127] En este capítulo estudiamos el efecto de los tratamientos posteriores a la deposición de películas de MoO_3 en la interfaz con el HTL en células solares de perovskita. El HTL que se usó es TaTm y la configuración del dispositivo consiste en ITO/MoO_3/TaTm/$MAPbI_3$/C60/BCP/Ag. Investigamos y comparamos el efecto del tratamiento térmico del MoO_3 antes de la deposición de TaTm y el efecto del mismo sobre doble capas de MoO_3/TaTm. Examinamos un amplio rango de temperaturas de 60 a 200 °C.

5.2. Resultado y discusión

Los parámetros de rendimiento fotovoltaicos extraídos de las curvas JV para una serie de células solares en función de la temperatura del tratamiento térmico, se muestran en la figura 23. Todos los dispositivos mostraron un J_{SC} similar de aproximadamente 19-20 mA cm^{-2}. La figura 23.B muestra un aumento en el V_{OC} al aumentar la temperatura de 60 °C a 100 °C para ambas series de dispositivos. Es importante destacar que para las células con tratamiento térmico efectuado sobre las bicapas de MoO_3/TaTm, se encontró que el V_{OC} era alto y estable (> 1.12 V) incluso para temperaturas superiores a 100 °C. Al contrario, el voltaje resultó ser más bajo (<1.11 V) y con una disminución progresiva para las células donde el tratamiento térmico se llevó a cabo solo con el MoO_3 . Para las células preparadas con tratamiento sobre bicapas de MoO_3/TaTm, el FF aumenta de manera prominente del 73% (a 60 °C) a aproximadamente el 80% (en el rango de 120 a 200 °C), mientras que si el tratamiento se lleva a cabo antes de la deposición de TaTm, el FF muestra un valor constante de aproximadamente el 73% hasta 140 °C, y luego una disminución continua hasta el 65% (figura 23.C). La evolución de la PCE (figura 23.D) sigue tendencias bastante similares a las de FF para ambas series de dispositivos.

También se investigó el funcionamiento de las mejores células solares de las dos series de dispositivos (con tratamiento térmico del contacto frontal a la temperatura de 140 °C) en función de la intensidad de la luz incidente, como se resume en la figura 25. Se han calculado factores de idealidad de diodo (IF) de 1.9 y 1.4 para regímenes de baja (0.1 - 10 mW cm^{-2}) y de alta intensidad (10 - 100 mW cm^{-2}) respectivamente, sin diferencias significativas para los dos conjuntos de dispositivos (figura 25 A-B). Sin embargo, se vio que el V_{OC} era sistemáticamente más alto al llevar a cabo el tratamiento térmico de las dos capas TaTm/MoO_3 juntas, lo que indica una reducción de la recombinación no radiativa. El IF cercano a 2, calculado a baja concentración de portadores, sugiere que la recombinación dominante es asistida por trampa, mientras que a intensidades de luz más altas el IF se reduce (1.4) debido al aumento de la recombinación superficial.[136]

La figura 25. C-D muestra la tendencia del FF al aumentar la intensidad de la luz. Para los dispositivos con tratamiento térmico sobre MoO_3 antes de la deposición con TaTm, no se puede observar una tendencia clara (figura 25.C), probablemente debido a la presencia de una barrera de extracción en la interfaz MoO_3/TaTm, que no conlleva un aumento de la recombinación (la dependencia del V_{OC} con la intensidad de luz es similar para ambos dispositivos). La existencia de una barrera de potencial en la interfaz MoO_3/TaTm dificulta la recolección eficiente de carga en el contacto p, reduciendo el FF (<77%) de las células solares. Esta barrera también justificaría la resistencia en serie observada para estos diodos (figura 24.B). Para dispositivos de alta eficiencia con tratamiento térmico sobre la bicapa de

MoO_3/TaTm (figura 3.D), la disminución de FF a baja intensidad de luz (baja concentración de portadores) indica que las trampas dominan este régimen, de acuerdo con la tendencia del fotovoltaje (figura 23.B).

Las mediciones de sonda Kelvin se realizaron (en aire) en la superficie de MoO_3 en función de la temperatura de tratamiento térmico. Esta muestra una función de trabajo (WF) de 5.05 eV a 60 °C mientras que para temperaturas más altas se encontró que la WF del MoO_3 disminuía aproximadamente en 0.2 eV. La reducción de la WF es consistente con la tendencia del FF observada en la figura 23.C para células solares con tratamiento térmico únicamente en el MoO_3. Esto confirma que la WF del electrodo es responsable de la barrera de extracción y la recombinación en el contacto frontal. Estas variaciones se deben a un aumento de las vacantes de oxígeno que resulta en una disminución de la WF de MoO_3.[137,138] La medición mediante sonda Kelvin es una técnica sensible a la superficie, por lo tanto no pudimos extraer información significativa para las películas de MoO_3 recubiertas con TaTm. En este caso, la pérdida de oxígeno en el tratamiento térmico podría verse obstaculizada por la presencia de la barrera física de TaTm en la parte superior de MoO_3 que da como resultado un mejor contacto óhmico dentro de la interfaz MoO_3/TaTm.[101]

5.3. Conclusión

Observamos que la eficiencia de células solares de perovskita de tipo p-i-n puede mejorarse sustancialmente mediante un tratamiento térmico del contacto frontal MoO_3/TaTm. Se lograron grandes mejoras en el FF (> 80%) y en la PCE (18%) al depositar TaTm y llevar a cabo el tratamiento térmico junto con

MoO_3, con resultados óptimos para una temperatura de 140 °C. El mejor rendimiento de las células solares con tratamiento térmico de las bicapas ITO/MoO_3 probablemente esté relacionado con una interacción entre los dos materiales, lo que minimiza la barrera de energía para la transferencia de huecos en su interfaz.

Bibliography

1. "*Renewables Global Status Report*", Members, R. E. N. available at: https://www.ren21.net/reports/global-status-report/ (2019).

2. Green, M. A. *et al.* Solar cell efficiency tables (version 50). *Prog. Photovoltaics Res. Appl.* **25**, 668–676 (2017).

3. Manser, J. S., Christians, J. A. & Kamat, P. V. Intriguing Optoelectronic Properties of Metal Halide Perovskites. *Chem. Rev.* **116**, 12956–13008 (2016).

4. "Time to Switch on to Alternative Energy", available at: http://zafarson.com/services/solar-panels/.

5. "Sustainable Implementation of Electric Vehicles" available at: https://lightyear.one/.

6. Watthage, S. C., Song, Z., Phillips, A. B. & Heben, M. J. Evolution of Perovskite Solar Cells. *Perovskite Photovoltaics* 43–88 (Elsevier, 2018).

7. MØLLER, C. K. Crystal Structure and Photoconductivity of Cæsium Plumbohalides. *Nature* **182**, 1436–1436 (1958).

8. Jena, A. K., Kulkarni, A. & Miyasaka, T. Halide Perovskite Photovoltaics: Background, Status, and Future Prospects. *Chem. Rev.* **119**, 3036–3103 (2019).

9. Jain, A., Castelli, I. E., Hautier, G., Bailey, D. H. & Jacobsen, K. W. Performance of genetic algorithms in search for water splitting perovskites. *J. Mater. Sci.* **48**, 6519–6534 (2013).

10. Green, M. A., Ho-Baillie, A. & Snaith, H. J. The emergence of perovskite solar cells. *Nat. Photonics* **8**, 506–514 (2014).

11. D'Innocenzo, V. *et al.* Excitons versus free charges in organo-lead tri-halide perovskites. *Nat. Commun.* **5**, 1–6 (2014).

12. Lin, Q., Armin, A., Nagiri, R. C. R., Burn, P. L. & Meredith, P. Electro-optics of perovskite solar cells. *Nat. Photonics* **9**, 106–112 (2015).

13. Wehrenfennig, C., Eperon, G. E., Johnston, M. B., Snaith, H. J. & Herz, L. M. High Charge Carrier Mobilities and Lifetimes in Organolead Trihalide Perovskites. *Adv. Mater.* **26**, 1584–1589 (2014).

14. Ponseca, C. S. *et al.* Organometal Halide Perovskite Solar Cell Materials

Rationalized: Ultrafast Charge Generation, High and Microsecond-Long Balanced Mobilities, and Slow Recombination. *J. Am. Chem. Soc.* **136**, 5189–5192 (2014).

15. Wehrenfennig, C., Liu, M., Snaith, H. J., Johnston, M. B. & Herz, L. M. Charge-carrier dynamics in vapour-deposited films of the organolead halide perovskite $CH_3NH_3PbI_{3-x}Cl_x$. *Energy Environ. Sci.* **7**, 2269–2275 (2014).

16. Stranks, S. D. *et al.* Electron-Hole Diffusion Lengths Exceeding one Micrometer in an Organometal Trihalide Perovskite Absorber. *Science (80).* **342**, 341–344 (2013).

17. Gonzalez-Pedro, V. *et al.* General Working Principles of $CH_3NH_3PbX_3$ Perovskite Solar Cells. *Nano Lett.* **14**, 888–893 (2014).

18. Zheng, K. *et al.* Trap States and Their Dynamics in Organometal Halide Perovskite Nanoparticles and Bulk Crystals. *J. Phys. Chem. C* **120**, 3077–3084 (2016).

19. Zhao, Y., Nardes, A. M. & Zhu, K. Solid-State Mesostructured Perovskite $CH_3NH_3PbI_3$ Solar Cells: Charge Transport, Recombination, and Diffusion Length. *J. Phys. Chem. Lett.* **5**, 490–494 (2014).

20. Yin, W.-J., Yang, J.-H., Kang, J., Yan, Y. & Wei, S.-H. Halide perovskite materials for solar cells: a theoretical review. *J. Mater. Chem. A* **3**, 8926–8942 (2015).

21. Leguy, A. M. A. *et al.* Experimental and theoretical optical properties of methylammonium lead halide perovskites. *Nanoscale* **8**, 6317–6327 (2016).

22. Weller, M. T., Weber, O. J., Frost, J. M. & Walsh, A. Cubic Perovskite Structure of Black Formamidinium Lead Iodide, α-$[HC(NH_2)_2]PbI_3$, at 298 K. *J. Phys. Chem. Lett.* **6**, 3209–3212 (2015).

23. Noh, J. H., Im, S. H., Heo, J. H., Mandal, T. N. & Seok, S. Il. Chemical Management for Colorful, Efficient, and Stable Inorganic–Organic Hybrid Nanostructured Solar Cells. *Nano Lett.* **13**, 1764–1769 (2013).

24. Suarez, B. *et al.* Recombination Study of Combined Halides (Cl, Br, I) Perovskite Solar Cells. *J. Phys. Chem. Lett.* **5**, 1628–1635 (2014).

25. Comin, R. *et al.* Structural, optical, and electronic studies of wide-bandgap lead halide perovskites. *J. Mater. Chem. C* **3**, 8839–8843

(2015).

26. Chen, H., Sakai, N., Ikegami, M. & Miyasaka, T. Emergence of Hysteresis and Transient Ferroelectric Response in Organo-Lead Halide Perovskite Solar Cells. Nature photonics **8**, 506-514 (2015).

27. van Reenen, S., Kemerink, M. & Snaith, H. J. Modeling Anomalous Hysteresis in Perovskite Solar Cells. *J. Phys. Chem. Lett.* **6**, 3808–3814 (2015).

28. Azpiroz, J. M., Mosconi, E., Bisquert, J. & De Angelis, F. Defect migration in methylammonium lead iodide and its role in perovskite solar cell operation. *Energy Environ. Sci.* **8**, 2118–2127 (2015).

29. Snaith, H. J. *et al.* Anomalous Hysteresis in Perovskite Solar Cells. *J. Phys. Chem. Lett.* **5**, 1511–1515 (2014).

30. Fabini, D. Quantifying the Potential for Lead Pollution from Halide Perovskite Photovoltaics. *J. Phys. Chem. Lett.* **6**, 3546–3548 (2015).

31. Hao, F., Stoumpos, C. C., Chang, R. P. H. & Kanatzidis, M. G. Anomalous Band Gap Behavior in Mixed Sn and Pb Perovskites Enables Broadening of Absorption Spectrum in Solar Cells. *J. Am. Chem. Soc.* **136**, 8094–8099 (2014).

32. Zhu, H. L. *et al.* Controllable Crystallization of $CH_3NH_3Sn_{0.25}Pb_{0.75}I_3$ Perovskites for Hysteresis-Free Solar Cells with Efficiency Reaching 15.2%. *Adv. Funct. Mater.* **27**, 1605469 (2017).

33. Igual-Muñoz, A. M., Ávila, J., Boix, P. P. & Bolink, H. J. $FAPb_{0.5}Sn_{0.5}I_3$: A Narrow Bandgap Perovskite Synthesized through Evaporation Methods for Solar Cell Applications. *Sol. RRL* solr. **4**, 1900283 (2019).

34. Liao, W. *et al.* Fabrication of Efficient Low-Bandgap Perovskite Solar Cells by Combining Formamidinium Tin Iodide with Methylammonium Lead Iodide. *J. Am. Chem. Soc.* **138**, 12360–12363 (2016).

35. Gupta, S., Cahen, D. & Hodes, G. How SnF 2 Impacts the Material Properties of Lead-Free Tin Perovskites. *J. Phys. Chem. C* **122**, 13926–13936 (2018).

36. Goldschmidt, V. M. Die Gesetze der Krystallochemie. *Naturwissenschaften* **14**, 477–485 (1926).

37. Pang, S. *et al.* $NH_2CH{=}NH_2PbI_3$: An Alternative Organolead Iodide Perovskite Sensitizer for Mesoscopic Solar Cells. *Chem. Mater.* **26**,

1485–1491 (2014).

38. Amat, A. *et al.* Cation-Induced Band-Gap Tuning in Organohalide Perovskites: Interplay of Spin–Orbit Coupling and Octahedra Tilting. *Nano Lett.* **14**, 3608–3616 (2014).

39. Poglitsch, A. & Weber, D. Dynamic disorder in methylammoniumtrihalogenoplumbates (II) observed by millimeter-wave spectroscopy. *J. Chem. Phys.* **87**, 6373–6378 (1987).

40. Quarti, C. *et al.* Structural and optical properties of methylammonium lead iodide across the tetragonal to cubic phase transition: implications for perovskite solar cells. *Energy Environ. Sci.* **9**, 155–163 (2016).

41. Whitfield, P. S. *et al.* Structures, Phase Transitions and Tricritical Behavior of the Hybrid Perovskite Methyl Ammonium Lead Iodide. *Sci. Rep.* **6**, 1–15 (2016).

42. Baikie, T. *et al.* Synthesis and crystal chemistry of the hybrid perovskite $(CH_3NH_3)PbI_3$ for solid-state sensitised solar cell applications. *J. Mater. Chem. A* **1**, 5628 (2013).

43. Baikie, T. *et al.* A combined single crystal neutron/X-ray diffraction and solid-state nuclear magnetic resonance study of the hybrid perovskites $CH_3NH_3PbX_3$ (X = I, Br and Cl). *J. Mater. Chem. A* **3**, 9298–9307 (2015).

44. Szafrański, M. & Katrusiak, A. Mechanism of Pressure-Induced Phase Transitions, Amorphization, and Absorption-Edge Shift in Photovoltaic Methylammonium Lead Iodide. *J. Phys. Chem. Lett.* **7**, 3458–3466 (2016).

45. Palazon, F. *et al.* Room-Temperature Cubic Phase Crystallization and High Stability of Vacuum-Deposited Methylammonium Lead Triiodide Thin Films for High-Efficiency Solar Cells. *Adv. Mater.* **31**, 1902692 (2019).

46. Kojima, A., Teshima, K., Shirai, Y. & Miyasaka, T. Organometal Halide Perovskites as Visible-Light Sensitizers for Photovoltaic Cells. *J. Am. Chem. Soc.* **131**, 6050–6051 (2009).

47. Im, J. H., Lee, C. R., Lee, J. W., Park, S. W. & Park, N. G. 6.5% Efficient Perovskite Quantum-Dot-Sensitized Solar Cell. *Nanoscale* **3**, 4088–4093 (2011).

48. Lee, M. M., Teuscher, J., Miyasaka, T., Murakami, T. N. & Snaith, H. J. Efficient Hybrid Solar Cells Based on Meso-Superstructured Organometal Halide Perovskites. *Science (80-.).* **338**, 643–647 (2012).

49. Eperon, G. E., Burlakov, V. M., Docampo, P., Goriely, A. & Snaith, H. J. Morphological control for high performance, solution-processed planar heterojunction perovskite solar cells. *Adv. Funct. Mater.* **24**, 151–157 (2014).

50. Di Giacomo, F., Fakharuddin, A., Jose, R. & Brown, T. M. Progress, challenges and perspectives in flexible perovskite solar cells. *Energy Environ. Sci.* **9**, 3007–3035 (2016).

51. You, J., Meng, L., Hong, Z., Li, G. & Yang, Y. Inverted Planar Structure of Perovskite Solar Cells. *Organic-Inorganic Halide Perovskite Photovoltaics* 307–324 (Springer International Publishing, 2016).

52. Heo, J. H., Han, H. J., Kim, D., Ahn, T. K. & Im, S. H. Hysteresis-less inverted $CH_3NH_3PbX_3$ planar perovskite hybrid solar cells with 18.1% power conversion efficiency. *Energy Environ. Sci.* **8**, 1602–1608 (2015).

53. Wu, C.-G. *et al.* High efficiency stable inverted perovskite solar cells without current hysteresis. *Energy Environ. Sci.* **8**, 2725–2733 (2015).

54. Marinova, N., Valero, S. & Delgado, J. L. Organic and perovskite solar cells: Working principles, materials and interfaces. *J. Colloid Interface Sci.* **488**, 373–389 (2017).

55. Ameri, T., Li, N. & Brabec, C. J. Highly efficient organic tandem solar cells: a follow up review. *Energy Environ. Sci.* **6**, 2390 (2013).

56. Herz, L. M. Charge-Carrier Dynamics in Organic-Inorganic Metal Halide Perovskites. *Annu. Rev. Phys. Chem.* **67**, 65–89 (2016).

57. Schulz, P., Cahen, D. & Kahn, A. Halide Perovskites: Is It All about the Interfaces? *Chem. Rev.* **119**, 3349–3417 (2019).

58. Kirchartz, T., Ding, K. & Rau, U. Fundamental Electrical Characterization of Thin-Film Solar Cells. *Advanced Characterization Techniques for Thin Film Solar Cells* 33–60 (Wiley-VCH Verlag GmbH & Co. KGaA, 2011).

59. Sarritzu, V. *et al.* Optical determination of Shockley-Read-Hall and interface recombination currents in hybrid perovskites. *Sci. Rep.* **7**, 1–10 (2017).

60. Krogmeier, B., Staub, F., Grabowski, D., Rau, U. & Kirchartz, T. Quantitative analysis of the transient photoluminescence of $CH_3NH_3PbX_3/PC_{61}BM$ heterojunctions by numerical simulations. *Sustain. Energy Fuels* **2**, 1027–1034 (2018).

61. Tao, C. *et al. 17.6%* stabilized efficiency in low-temperature processed planar perovskite solar cell*s. Energy & Environmental Science* **8**, 2365-2370 (2015).

62. Chiang, C.-H., Tseng, Z.-L. & Wu, C.-G. Planar heterojunction perovskite/$PC_{71}BM$ solar cells with enhanced open-circuit voltage via a (2/1)-step spin-coating process. *J. Mater. Chem. A* **2**, 15897–15903 (2014).

63. Docampo, P., Ball, J. M., Darwich, M., Eperon, G. E. & Snaith, H. J. Efficient organometal trihalide perovskite planar-heterojunction solar cells on flexible polymer substrates. *Nat. Commun.* **4**, 2761 (2013).

64. Jeng, J.-Y. *et al.* CH 3 NH 3 PbI 3 Perovskite/Fullerene Planar-Heterojunction Hybrid Solar Cells. *Adv. Mater.* **25**, 3727–3732 (2013).

65. Wang, K.-C. *et al.* p-type Mesoscopic Nickel Oxide/Organometallic Perovskite Heterojunction Solar Cells. *Sci. Rep.* **4**, 4756 (2015).

66. Li, G., Chu, C.-W., Shrotriya, V., Huang, J. & Yang, Y. Efficient inverted polymer solar cells. *Appl. Phys. Lett.* **88**, 253503 (2006).

67. Christians, J. A., Fung, R. C. M. & Kamat, P. V. An Inorganic Hole Conductor for Organo-Lead Halide Perovskite Solar Cells. Improved Hole Conductivity with Copper Iodide. *J. Am. Chem. Soc.* **136**, 758–764 (2014).

68. Sun, S. *et al.* The origin of high efficiency in low-temperature solution-processable bilayer organometal halide hybrid solar cells. *Energy Environ. Sci.* **7**, 399–407 (2014).

69. Polander, L. E. *et al.* Hole-transport material variation in fully vacuum deposited perovskite solar cells. *APL Mater.* **2**, 081503 (2014).

70. Wu, Z. *et al.* Efficient planar heterojunction perovskite solar cells employing graphene oxide as hole conductor. *Nanoscale* **6**, 10505–10510 (2014).

71. Subbiah, A. S. *et al.* Inorganic Hole Conducting Layers for Perovskite-Based Solar Cells. *J. Phys. Chem. Lett.* **5**, 1748–1753 (2014).

72. Schloemer, T. H., Christians, J. A., Luther, J. M. & Sellinger, A. Doping strategies for small molecule organic hole-transport materials: impacts on perovskite solar cell performance and stability. *Chem. Sci.* **10**, 1904–1935 (2019).

73. Avila, J. *et al.* Influence of doped charge transport layers on efficient perovskite solar cells. *Sustain. Energy Fuels* **2**, 2429–2434 (2018).

74. Momblona, C. *et al.* Efficient vacuum deposited p-i-n and n-i-p perovskite solar cells employing doped charge transport layers. *Energy Environ. Sci.* **9**, 3456–3463 (2016).

75. Shin, S. S., Lee, S. J. & Seok, S. Il. Metal Oxide Charge Transport Layers for Efficient and Stable Perovskite Solar Cells. *Adv. Funct. Mater.* **29**, 1900455 (2019).

76. O'Brien, D. F., Baldo, M. A., Thompson, M. E. & Forrest, S. R. Improved energy transfer in electrophosphorescent devices. *Appl. Phys. Lett.* **74**, 442–444 (1999).

77. Peumans, P. & Forrest, S. R. Very-high-efficiency double-heterostructure copper phthalocyanine/C_{60} photovoltaic cells. *Appl. Phys. Lett.* **79**, 126–128 (2001).

78. Yoshida, H. Electron Transport in Bathocuproine Interlayer in Organic Semiconductor Devices. *J. Phys. Chem. C* **119**, 24459–24464 (2015).

79. Gil-Escrig, L., Momblona, C., Sessolo, M. & Bolink, H. J. Fullerene imposed high open-circuit voltage in efficient perovskite based solar cells. *J. Mater. Chem. A* **4**, 3667–3672 (2016).

80. Sun, K., Chang, J., Isikgor, F. H., Li, P. & Ouyang, J. Efficiency enhancement of planar perovskite solar cells by adding zwitterion/LiF double interlayers for electron collection. *Nanoscale* **7**, 896–900 (2015).

81. Seo, J. *et al.* Benefits of very thin PCBM and LiF layers for solution-processed p–i–n perovskite solar cells. *Energy Environ. Sci.* **7**, 2642–2646 (2014).

82. Xue, Q. *et al.* Highly efficient fullerene/perovskite planar heterojunction solar cells via cathode modification with an amino-functionalized polymer interlayer. *J. Mater. Chem. A* **2**, 19598–19603 (2014).

83. Chen, C.-C. *et al.* Perovskite/polymer monolithic hybrid tandem solar cells utilizing a low-temperature, full solution process. *Mater. Horizons* **2**, 203–211 (2015).

84. You, J. *et al.* Low-Temperature Solution-Processed Perovskite Solar Cells with High Efficiency and Flexibility. *ACS Nano* **8**, 1674–1680 (2014).

85. Min, J. *et al.* Interface Engineering of Perovskite Hybrid Solar Cells with Solution-Processed Perylene–Diimide Heterojunctions toward High Performance. *Chem. Mater.* **27**, 227–234 (2015).

86. Salehi, A. *et al.* Realization of high-efficiency fluorescent organic light-emitting diodes with low driving voltage. *Nat. Commun.* **10**, 2305 (2019).

87. Mitzi, D. B., Prikas, M. T. & Chondroudis, K. Thin Film Deposition of Organic−Inorganic Hybrid Materials Using a Single Source Thermal Ablation Technique. *Chem. Mater.* **11**, 542–544 (1999).

88. Liu, M., Johnston, M. B. & Snaith, H. J. Efficient planar heterojunction perovskite solar cells by vapour deposition. *Nature* **501**, 395–398 (2013).

89. Sessolo, M., Momblona, C., Gil-Escrig, L. & Bolink, H. J. Photovoltaic devices employing vacuum-deposited perovskite layers. *MRS Bull.* **40**, 660–666 (2015).

90. Green, M. A. *et al.* Solar cell efficiency tables (Version 53). *Prog. Photovoltaics Res. Appl.* **27**, 3–12 (2019).

91. Jang, J., Choe, G. & Yim, S. E ff ective Control of Chlorine Contents in $MAPbI_{3-x}Cl_x$ Perovskite Solar Cells Using a Single-Source Vapor Deposition and Anion- Exchange Technique. *ACS Appl. Mater. Interfaces* **11**, 20073–20081 (2019).

92. Colella, S. *et al.* $MAPbI_{3-x}Cl_x$ mixed halide perovskite for hybrid solar cells: The role of chloride as dopant on the transport and structural properties. *Chem. Mater.* **25**, 4613–4618 (2013).

93. Nh, C. H. *et al.* The optoelectronic role of chlorine in. *Nat. Commun.* **6**, 1–9 (2015).

94. Colella, S. *et al.* Elusive presence of chloride in mixed halide perovskite solar cells. *J. Phys. Chem. Lett.* **5**, 3532–3538 (2014).

95. Xie, F. X., Su, H., Mao, J., Wong, K. S. & Choy, W. C. H. Evolution of diffusion length and trap state induced by chloride in perovskite solar cell. *J. Phys. Chem. C* **120**, 21248–21253 (2016).

96. Edri, E. *et al.* Why lead methylammonium tri-iodide perovskite-based solar cells require a mesoporous electron transporting scaffold (but not necessarily a hole conductor). *Nano Lett.* **14**, 1000–1004 (2014).

97. Herz, L. M. Charge-Carrier Mobilities in Metal Halide Perovskites: Fundamental Mechanisms and Limits. *ACS Energy Lett.* **2**, 1539–1548 (2017).

98. Yu, H. *et al.* The role of chlorine in the formation process of $CH_3NH_3PbI_{3-x}Cl_x$ perovskite. *Adv. Funct. Mater.* **24**, 7102–7108 (2014).

99. Longo, G. *et al.* Fully Vacuum-Processed Wide Band Gap Mixed-Halide Perovskite Solar Cells. *ACS Energy Lett.* **3**, 214–219 (2018).

100. Gil-Escrig, L. *et al.* Vacuum Deposited Triple-Cation Mixed-Halide Perovskite Solar Cells. *Adv. Energy Mater.* **8**, 1703506 (2018).

101. Pérez-del-Rey, D. *et al.* Molecular Passivation of MoO_3: Band Alignment and Protection of Charge Transport Layers in Vacuum-Deposited Perovskite Solar Cells. *Chem. Mater.* **31**, 6945–6949 (2019).

102. Abdi-Jalebi, M. *et al.* Maximizing and stabilizing luminescence from halide perovskites with potassium passivation. *Nature* **555**, 497–501 (2018).

103. Brenner, T. M., Egger, D. A., Kronik, L., Hodes, G. & Cahen, D. Hybrid organic—inorganic perovskites: low-cost semiconductors with intriguing charge-transport properties. *Nat. Rev. Mater.* **1**, 15007 (2016).

104. Dunlap-Shohl, W. A., Zhou, Y., Padture, N. P. & Mitzi, D. B. Synthetic Approaches for Halide Perovskite Thin Films. *Chem. Rev.* **119**, 3193–3295 (2019).

105. Shamsi, J., Urban, A. S., Imran, M., De Trizio, L. & Manna, L. Metal Halide Perovskite Nanocrystals: Synthesis, Post-Synthesis Modifications, and Their Optical Properties. *Chem. Rev.* **119**, 3296–3348 (2019).

106. Dunlap-Shohl, W. A., Zhou, Y., Padture, N. P. & Mitzi, D. B. Synthetic Approaches for Halide Perovskite Thin Films. *Chem. Rev.* **119**, 3193–

3295 (2019).

107. Fan, P. *et al.* High-performance perovskite $CH_3NH_3PbI_3$ thin films for solar cells prepared by single-source physical vapour deposition. *Sci. Rep.* **6**, 29910 (2016).

108. Malinkiewicz, O. *et al.* Metal-Oxide-Free Methylammonium Lead Iodide Perovskite-Based Solar Cells: the Influence of Organic Charge Transport Layers. *Adv. Energy Mater.* **4**, 1400345 (2014).

109. Castro, E., Murillo, J., Fernandez-Delgado, O. & Echegoyen, L. Progress in fullerene-based hybrid perovskite solar cells. *J. Mater. Chem. C* **6**, 2635–2651 (2018).

110. Shao, Y., Xiao, Z., Bi, C., Yuan, Y. & Huang, J. Origin and elimination of photocurrent hysteresis by fullerene passivation in $CH_3NH_3PbI_3$ planar heterojunction solar cells. *Nat. Commun.* **5**, 5784 (2014).

111. Hsiao, S.-Y. *et al.* Efficient All-Vacuum Deposited Perovskite Solar Cells by Controlling Reagent Partial Pressure in High Vacuum. *Adv. Mater.* **28**, 7013–7019 (2016).

112. Gommans, H. *et al.* On the Role of Bathocuproine in Organic Photovoltaic Cells. *Adv. Funct. Mater.* **18**, 3686–3691 (2008).

113. Chen, C. *et al.* Effect of BCP buffer layer on eliminating charge accumulation for high performance of inverted perovskite solar cells. *RSC Adv.* **7**, 35819–35826 (2017).

114. Schmitz, C., Schmidt, H.-W. & Thelakkat, M. Lithium−Quinolate Complexes as Emitter and Interface Materials in Organic Light-Emitting Diodes. *Chem. Mater.* **12**, 3012–3019 (2000).

115. Kido, J. & Matsumoto, T. Bright organic electroluminescent devices having a metal-doped electron-injecting layer. *Appl. Phys. Lett.* **73**, 2866–2868 (1998).

116. Ross, R. T. Some thermodynamics of photochemical systems. *J. Chem. Phys.* **46**, 4590–4593 (1967).

117. Schulz, P. *et al.* Electronic Level Alignment in Inverted Organometal Perovskite Solar Cells. *Adv. Mater. Interfaces* **2**, 1400532 (2015).

118. Olthof, S. & Meerholz, K. Substrate-dependent electronic structure and film formation of $MAPbI_3$ perovskites. *Sci. Rep.* **7**, 40267 (2017).

119. Hoke, E. T. *et al.* Reversible photo-induced trap formation in mixed-halide hybrid perovskites for photovoltaics. *Chem. Sci.* **6**, 613–617 (2015).

120. Tsai, H. *et al.* Light-induced lattice expansion leads to high-efficiency perovskite solar cells. *Science (80-.).* **360**, 67–70 (2018).

121. deQuilettes, D. W. *et al.* Photo-induced halide redistribution in organic–inorganic perovskite films. *Nat. Commun.* **7**, 11683 (2016).

122. Leguy, A. M. A. *et al.* Reversible Hydration of $CH_3NH_3PbI_3$ in Films, Single Crystals, and Solar Cells. *Chem. Mater.* **27**, 3397–3407 (2015).

123. Boyd, C. C., Cheacharoen, R., Leijtens, T. & McGehee, M. D. Understanding Degradation Mechanisms and Improving Stability of Perovskite Photovoltaics. *Chem. Rev.* **119**, 3418–3451 (2019).

124. Kung, P. K. *et al.* A Review of Inorganic Hole Transport Materials for Perovskite Solar Cells. *Adv. Mater. Interfaces* **5**, 1–35 (2018).

125. Zanoni, K. P. S. *et al.* Use of Hydrogen Molybdenum Bronze in Vacuum-Deposited Perovskite Solar Cells. *Energy Technol.* 1900734 (2019).

126. Liu, Z. *et al.* Improving the stability of the perovskite solar cells by V 2 O 5 modified transport layer film. *RSC Adv.* **7**, 18456–18465 (2017).

127. Gong, Y. *et al.* Diverse Application of MoO3 for High Performance Organic Photovoltaics: Fundamentals, Processes and Optimization Strategies. *J. Mater. Chem. A* (2019). doi:10.1039/C9TA12005J

128. Bhaumik, S. & Pal, A. J. Light-Emitting Diodes Based on Solution-Processed Nontoxic Quantum Dots: Oxides as Carrier-Transport Layers and Introducing Molybdenum Oxide Nanoparticles as a Hole-Inject Layer. *ACS Appl. Mater. Interfaces* **6**, 11348–11356 (2014).

129. Zhang, H., Chen, S. & Sun, X. W. Efficient Red/Green/Blue Tandem Quantum-Dot Light-Emitting Diodes with External Quantum Efficiency Exceeding 21%. *ACS Nano* **12**, 697–704 (2018).

130. Kim, B.-S., Kim, T.-M., Choi, M.-S., Shim, H.-S. & Kim, J.-J. Fully vacuum–processed perovskite solar cells with high open circuit voltage using MoO_3/NPB as hole extraction layers. *Org. Electron.* **17**, 102–106 (2015).

131. Jiang, Y., Li, C., Liu, H., Qin, R. & Ma, H. Poly(3,4-ethylenedioxythiophene):poly(styrenesulfonate)(PEDOT:PSS)–

molybdenum oxide composite films as hole conductors for efficient planar perovskite solar cells. *J. Mater. Chem. A* **4**, 9958–9966 (2016).

132. Zanoni, K. P. S. *et al.* Molecular Passivation of MoO_3 : Band Alignment and Protection of Charge Transport Layers in Vacuum-Deposited Perovskite Solar. *Chem. Mater.* **31**, 6945-6949 (2019).

133. Gong, Y. *et al.* Diverse applications of MoO_3 for high performance organic photovoltaics: fundamentals, processes and optimization strategies. *J. Mater. Chem. A* **8**, 978–1009 (2020).

134. Dänekamp, B. *et al.* Efficient Photo- and Electroluminescence by Trap States Passivation in Vacuum-Deposited Hybrid Perovskite Thin Films. *ACS Appl. Mater. Interfaces* **10**, 36187–36193 (2018).

135. Parrott, E. S. *et al.* Growth modes and quantum confinement in ultrathin vapour-deposited $MAPbI_3$ films. *Nanoscale* **11**, 14276–14284 (2019).

136. Tress, W. *et al.* Interpretation and evolution of open-circuit voltage, recombination, ideality factor and subgap defect states during reversible light-soaking and irreversible degradation of perovskite solar cells. *Energy Environ. Sci.* **11**, 151–165 (2018).

137. Greiner, M. T., Chai, L., Helander, M. G., Tang, W. & Lu, Z. Transition Metal Oxide Work Functions : The Influence of Cation Oxidation State and Oxygen Vacancies. *Adv. Funct. Mater.* **22**, 4557–4568 (2012).

138. Dasgupta, B. *et al.* Enhanced Extraction Rates through Gap States of Molybdenum Oxide Anode Bu ff er. (2013).

139. Patel, J. B., Milot, R. L., Wright, A. D., Herz, L. M. & Johnston, M. B. Formation Dynamis of $CH_3NH_3PbI_3$ Perovskite Following Two-Step Layer Deposition. *J. Phys. Chem. Lett.* **7**, 96–102 (2016).

140. Levine, I. *et al.* Can we use time-resolved measurements to get steady-state transport data for halide perovskites? *J. Appl. Phys.* **124**, 103103 (2018).

141. Chirvony, V. S. *et al.* Delayed Luminescence in Lead Halide Perovskite Nanocrystals. *J. Phys. Chem. C* **121**, 13381–13390 (2017).

List of abbreviations

CdTe	Cadmium telluride
CIGS	Copper Indium Gallium selenide/sulphide
c-Si	Crystalline Silicon
DFT	Density functional theory
DSSC	Dye-sensitized solar cells
E_g	Bandgap energy
EQE	External quantum efficiency
ETL	Electron transport layer
ETM	Electron transport material
FA	Formamidinium
FF	Fill factor
GaAs	Gallium arsenide
HOMO	Highest occupied molecular orbital
HTL	Hole transport layer
HTM	Hole transport material
I	Current
I_{ph}	Photocurrent
ITO	Indium tin oxide
J	Current density
LED	Light-emitting diode
LUMO	Lowest unoccupied molecular orbital

MA	Methylammonium
MPPT	Maximum power point tracking
OLED	Organic light-emitting diode
PCE	Power conversion efficiency
PL	Photoluminescence
PSC	Perovskite solar cell
PV	Photovoltaics
QCM	Quartz crystal microbalance
QFLS	Quasi-Fermi-level splitting
SEM	Scanning electron microscopy
SRH	Shockley-Read-Hall
TCSPC	Time-correlated single photon counting
TRPL	Time-resolved photoluminescence
UV	Ultraviolet
V	Voltage
V_{bi}	Built-in voltage
V_{OC}	Open-circuit voltage
XPS	X-ray photoemission spectroscopy
XRD	X-ray diffraction

Publications

Included in this thesis:

- **A. Babaei,** W. Soltanpoor, M.A.Tesa-Serrate, S. Yerci, M Sessolo, H.J. Bolink**,** Preparation and Characterization of Mixed Halide MAPbI3−xClx Perovskite Thin Films by Three-Source Vacuum Deposition, Energy Technol., **2019**, 1900784.
- **A. Babaei,** K. P. S. Zanoni, L. Gil-Escrig , D. Pérez-del-Rey, P. P. Boix, M. Sessolo, H. J. Bolink, *Efficient vacuum deposited pin perovskite solar cells by front contact optimization,* Frontiers in Chemistry, 2019, 10.3389.
- **A. Babaei,** Ch. Dreessen, M. Sessolo, H. J. Bolink, High voltage vacuum-processed perovskite solar cells with organic semiconducting interlayers**,** RSC Advances, 2020, Just accepted

Other publications:

- V. Sicilia, L. Arnal, A. J Chueca, S. Fuertes, **A. Babaei**, A. M. Igual Muñoz, M. Sessolo, H. J. Bolink, *Highly Photoluminescent Blue Ionic Platinum-Based Emitters,* Inorg. Chem. **2020**, 59, 1145−1152.
- F. Brunner, **A. Babaei**, A. Pertegás, J. M. Junquera-Hernández, A. Prescimone, E. C. Constable, H. J. Bolink, M. Sessolo, E. Ortí; C. E. Housecroft, *Phosphane tuning in heteroleptic [Cu(N^N)(P^P)]+ complexes for light-emitting electrochemical cells,* Dalton Trans., **2019,** 48, 446–460.
- R. Hallan, V. Fallah Hamidabadi, A. Huckaba, G. Galliani, **A. Babaei,** M.-G. La-Placa, A. Bahari, M. Sessolo, M.K. Nazeeruddin, I. McCulloch, H. J. Bolink. *New cross-linkable 9,10-diphenylanthracene derivative as wide bandgap host for solution-processed organic light-emitting diodes***,** J. Mater. Chem, **2018**, 30, 12948-12954
- **A. Babaei**, K. Rakstys, S. Guelen, V. Fallah Hamidabadi, M.-G. La-Placa, L. Martínez-Sarti, M. Sessolo, H. Aron Joel, O. P. M. Gaudin, V. Schanen, M. K. Nazeeruddin, H. J. Bolink, *Solution processed*

organic light-emitting diodes using a triazatruxene crosslinkable hole transporting material, RSC Adv., **2018**, 8, 35719-35723

- A. J. Huckaba, A. Senes, S. Aghazada, **A. Babaei**, S. C. J. Meskers, I. Zimmermann, P. Schouwink, N. Gasilova, R. A. J. Janssen, H. J. Bolink, M. K. Nazeeruddin, *Bis(arylimidazole) Iridium Picolinate Emitters and Preferential Dipole Orientation in Films,* ACS Omega., **2018**, 3, 2673-2682.
- **A. Babaei**, L. Albero-Blanquer, A. M. Igual-Muñoz, D. Perez-Del-Rey, M. Sessolo, H. J. Bolink, R. Tadmouri, *Hansen theory applied to the identification of nonhazardous solvents for hybrid perovskite thin-films processing,* Polyhedron., **2018**,147, 9-14.
- M.-G. La-Placa, G. Longo**, A. Babaei,** L. Martínez-Sarti, M. Sessolo, H. J. Bolink, *Photoluminescence quantum yield exceeding 80% in low dimensional perovskite thin-films via passivation control,* Chem. Commun., **2017**, 53, 62, 8707 -8710.
- F. Henwood, A. K. Pal; D. B. Cordes, A. M. Z. Slawin, T. W. Rees, C. Momblona, **A. Babaei**, A. Pertegás, E. Ortí, H. J. Bolink, E. Baranoff, E. Zysman-Colman, *Blue-emitting cationic iridium(III) complexes featuring pyridylpyrimidine ligands and their use in sky-blue electroluminescent devices*, J. Mater. Chem., **2017**, C., 5, 37, 9638-9650.
- S. Aghazada, A. J. Huckaba, A. Pertegas, **A. Babaei**, G. Grancini, I. Zimmermann, H. Bolink, M. K. Nazeeruddin, *Molecular Engineering of Iridium Blue Emitters Using Aryl N-Heterocyclic Carbene Ligands,* Eur. J. Inorg. Chem., **2016**, 32, 5089-5097.
- D. A. W. Ross, P. A. Scattergood, **A. Babaei**, A. Pertegás, H. J. Bolink, P. I. P. Elliott**,** *Luminescent osmium(II) bi-1,2,3-triazol-4-yl complexes: photophysical characterisation and application in light-emitting electrochemical cells*, Dalton Trans. **2016**, 45, 7748-7757.

Prior to Ph.d.:

- M.Marandi, N.Taghavinia, **A. Babaei**, *Super-hydrophilic characteristic of thermochemically preparedCdS nanocrystals,* Physica E, **2014**, 58, 146-152

Acknowledgments

Firstly, I would like to express my special gratitude to my supervisors, Henk Bolink and Michele Sessolo to give me the opportunity to join their fantastic group. Honestly, the journey of my doctorate would have never happened if Henk hadn't smoothened the difficulties ahead. Not only has he led me towards the field of optoelectronic devices and let me experience the beauty of it, but also inspired me with his endless spirit of pursuing goals, which would influence me throughout the rest of my life no matter which field I work in. I would like to express my appreciation to Michele. I feel so fortunate to have him as the PhD supervisor and really appreciate his support and mentorship in those years. Thanks for being always present to help, for you hard work to meet the deadlines, for your patience, for being so knowledgeable and funny at the same time, for all the scientific discussions and for all I have learned from you.

During my Ph.D. life in ICMOL, I have met so many great and helpful people who have influenced me in my professional and personal life. I would like to thank my best friend Maria, for all she has done during my Ph.D., regarding the tedious bureaucracy, correction the Spanish section of this thesis, and for all she has done for our friendship. Since the very beginning I arrived to Valencia she was always kind and helpful to me. Maria, you are the strongest girl I have ever met in my life and I am super happy to share all those good moments with you, and with Balma kuchulu. Thanks for being such an inspiration, such a good listener and such a great friend for me. Special thanks to Benni, for being always kind, for listening to me whenever I needed to talk, to be always present to help me, for all the laughter and joy we experienced together. Thanks for all the "chilling outs" in your apartment, for always reminding me "don't worry", for our interesting trips for conferences, and so many unforgettable memories. Maria Grazia, probably me and you shared the most time together. I am so happy for all the good memories we made together. Thanks for always being an initiator to talk and share your feelings with me. Thanks for your trust in me and for being kind and helpful. We made a lot of good memories together although we are sometimes like Mat and Pat, but even those moments we are funny, no? To Cristina, my Spanish sister, I will never forget all those good moments we had here in Valencia, windsurfing, dance classes which we never learned, our Chinese dinners and cakes at happiness seller, travel to cold Freiburg, your warm house in Lausanne and so many other things. I acknowledge Toni for training on the setups I used during my Ph.D. with such a patience, and for all the good moments we shared, for being always ready to assist me in the lab work. For keeping the flag of the OLEDs always flying in the group and for teaching me the funny parts of Spanish language. Thanks to David, who was the most active person I have ever met in my life with such an incredible energy to work and party at the same day. Thanks for all the good memories we shared while you were here in Valencia and for being such a good listener when I needed. Lidon, I always appreciate your hard working personality and humble character. I learned a lot from you and I am always grateful for that. I would like to thank Chris, who has been always positive and helpful. I always liked your enthusiasm to learn new topics. Dani, thanks for all the funny moments during lunch time. I really like your sense of humour and your creativity in making memes. Thanks to Jorge, for discussions we had about all the irrelevant topics, but I cannot thank you for the KitKats you never shared with me. Thanks to Ana who has a positive attitude and funny character as well. I will never forget our trip to Lausanne and the new word you added to my Spanish vocabulary. To Laura for being always ready to help everyone. Isidora, you are a positive person always with a smile ready to help people. I am really happy to have you among my friends and happier to share a lot of good moments with you. Kassio, I have to admit that I do regret why I got to know you only in the last year of my doctorate, although I have the hope that our friendship will not end by the end of this Ph.D, I will never forgot all the good memories, laughers, partying, and scientific collaborations we had together. I would also like to thank Paco for the final correction of the Spanish part of this thesis. I acknowledge the technical support from Jorge F. and Alejandra for all the help with laboratory equipment, and I also thank Alex for delivering all my packages. I would like to appreciate the help of Angel and Estrella, for always being nice and kind to me, for helping me with my mudanza. Angle, I think your name totally suits your character and I am thankful for all the things you taught me in the lab. I would like to thank all the past members of the group with whom I shared a lot of good moments and we learned a lot from each other: Giulia, Enrico, Vaheed, Wiria, Lina, Vittal, Pablo, Vladimir, and my gratitude as well to all the new comers of the group: Paz, Sang, Lorenzo, Xavi, Abhi, Cihan, Yous, Bas, Georgina, Beom, Arghanoon, Miguel, Vicente and Paula. Thanks to Ali for providing the fuel (Tea) while I was writing the thesis and for taking care of my plant.

I would like to express my appreciation to Dr. Anna Hayer and Dr. George Bernatz for welcoming me at Merck KGaA during my internship and thanks to all the colleague-friends I met there who made my stay more interesting: Hema, Stefan, Hsin-Rong (Mike), Beth, Ekaterina, Julian, Gabriel, Ha.

Sahar, my friend of life, I never can explain how inspiring you are for me. One of the blessings I have in my life is your friendship. Thanks for listening to me while I was nagging, crying, complaining and more thanks for your advices and all the good moments of life we shared together. Parvaneh, you are my geographically furthest but emotionally among closest friends I have ever had in my life. I learned from you how to look at life in a better way. Shiva and Marteen, you guys proved me one more time that the distance does not matter in friendship as long as our hearts are close to each other. Thanks for hosting me like a part of your family whenever I travelled to Belgium, for all the nice and hilarious moments while traveling, for all the nice Belgian beers and (spontaneous) Iranian teas we drunk together. Thanks to Kevin, for taking care of me, for being next to me. For his nice character and patience, for his endless kindness and positivity. For all the delicious food and for all the good memories we made together, some of which accompanied by cul cul.

I appreciate the friendship of all the nice people I met in Valencia during my doctorate, Giulia, Francesco, Raquel, Stephanie, and so many other nice people which I might forget to mention their name here. I would also like to take this opportunity to thank all my virtual friends in Googleplus, MeWe and Kolbeh who were supported and inspired me throughout all these years.

در آخر و از همه مهمتر از خانواده عزیزم تشکر می کنم. از مادرم که در تمامی این سالها پشتیبان من بوده و واژه از خودگذشتگی شاید با اسم او معنا شود. کسی که در تمام این مدت روحیه و انرژی مضاعف به من داده و در تمامی لحظه ها با وجود تمام فاصله جغرافیایی دست از حمایت من نکیشده. از پدرم که سخت کوشی و پشتکار را به من آموخته و همیشه پشتیبان و حامی من بوده. ممنون از هر دو شما برای همه زحمت ها و پشیبانی ها, برای راهنمایی ها و مراقبت ها, برای هموار کردن راه برای من تا به این مرحله. از برادران عزیزم آرش و امین. از آرش عزیز که قلبی بزرگ داری و همیشه به من انرژی مثبت دادی. از امین عزیزم که بدون وجود تو شاید اینهمه شادی و دلگرمی در زندگی من وجود نداشت. ممنون برای تمام لحظات خوب و شیرینی که با هم ساختیم برای حمایت ها و کمک ها و برای انرژی مثبتی که همیشه از شما گرفتم.